Title

Low-Field MR-guided Stereotactic Body Radiation Therapy for Prostate and Prostate Bed Cancer Response Management

Author

Pham, Jonathan

Publication Date

2023

Peer reviewed|Thesis/dissertation

UNIVERSITY OF CALIFORNIA

Los Angeles

Low-Field MR-guided Stereotactic Body Radiation Therapy for Prostate and Prostate Bed Cancer Response Management

A dissertation submitted in partial satisfaction of the

requirements for the degree Doctor of Philosophy

in Physics and Biology in Medicine

by

Jonathan Pham

2023

ABSTRACT OF THE DISSERTATION

Low-Field MR-guided Stereotactic Body Radiation Therapy for

Prostate and Prostate Bed Response Management

by

Jonathan Pham

Doctor of Philosophy in Physics and Biology in Medicine

University of California, Los Angeles, 2023

Professor Dan Ruan, Chair

Stereotactic body radiation therapy (SBRT) has become a standard-of-care option for localized prostate cancer, utilizing large fractionated dose in five or fewer fractions. Furthermore, SBRT may also be recommended for prostate patients who undergo radical prostatectomy as there is a high risk of biochemical recurrence. Despite improvement in treatment efficiency, SBRT toxicity remains a significant challenge for prostate and prostate bed patients. The development of MR-guided radiation therapy systems (MRgRT) has allowed the acquisition of high soft tissue contrast MRI for treatment planning, adaptation, and monitoring, which may be used to treatment toxicity. This dissertation sought to utilize a 0.35T MRgRT

system to develop new tools and features to help manage prostate and prostate bed SBRT treatment and toxicity management.

First, an air cavity electron density correction method was proposed for MR-guided online adaptive radiation therapy (MRgART) for more accurate dose calculation and better daily dose constraint management. MRgART air cavity electron density correction was shown to be unnecessary and clinically insignificant on low-field systems as SBRT plans were dosimetrically robust to air cavity variation. Next, a half-Fourier acquisition single-shot turbo spin echo (HASTE) MRI sequence was proposed to visualize the urethra with the aim to enable urethra dose constraining radiation therapy to mitigate genitourinary (GU) toxicity. HASTE demonstrated high urethra visibility with the potential to be used for treatment planning. Furthermore, HASTE was utilized to analyze urethral inter-fractional geometric and dosimetric variations. Urethra inter-fractional motion and anatomical changes were shown to result in daily urethral constraint failures. Therefore, on-board urethra imaging and treatment adaption may be warranted to protect the urethra. Lastly, a method to identify dosimetric predictors of GU toxicity, utilizing fraction-wise dose volume histogram metrics, based on a planning dose registration surrogate method, of urinary structures/substructures, was proposed. Planning dose registration was shown to be an accurate surrogate to the daily delivered dose for toxicity regression. Moreover, a logistic regression model using the identified dosimetric predictors was able to predict GU toxicity with an accuracy/sensitivity/specificity of 0.79/ 0.67/0.82. Fraction-wise urinary structure and substructure dosimetric predictors can be used to provide stable dosimetric metrics to guide treatment planning.

This dissertation of Jonathan Pham is approved.

Minsong Cao

Kyung Hyun Sung

Daniel Abraham Low

Amar Upadhyaya Kishan

Dan Ruan, Committee Chair

University of California, Los Angeles

2023

Table of Contents

List of Figures

List of Tables

Acknowledgements

I would like to thank the entire Physics and Biology in Medicine (PBM) program. Thank you Mike for giving the opportunity to pursue my passion in medical physics and further my interest in MR-guided radiation therapy. I really enjoyed my time here at UCLA, which I get to call home. Thank you Yingli and Dan for advising me through my four years here, your patience, guidance, and support have been extraordinary, and my success is owed to you two. Thank you, Dr. Amar Kishan for pushing forth prostate MR-guided radiation therapy, and allowing me to be a part of the clinical trial. Thank you Dr. Kyung Sung and Dr. Peng Hu for your guidance in better understanding MRI. Thank you, Dr. Minsong Cao for you guidance, mentorship, and always providing a perspective on the clinical impact of my work. Thank you, Dr. Dan Low for your enthusiasm and passion for medical physics research, it was very inspiring.

I would also like to thank my family, my mom and dad, Loan Cao and Jimmy Pham. Your never-ending love and support fuels me to be a better person every day. I get the honor of making you proud. Thank you to my sister, Jennifer Pham, for her support and admiration for what I do. I'm glad I get to share this part of my life with you all. It has been interesting journey and I have cherished every moment. I would lastly like to thank my cousin, Andy Do, who has been a rock for me, for many years. I can always count on you to be there for me, in the toughest times and also in the simple times. I appreciate your presence and insight, and I would not have been able to make it this far without you brother.

Vita

Education:

- M.Sc., Medical Physics, Duke University, Durham, NC, 2017-2019
- B.S., Physics, Bucknell University, Lewisburg, PA, 2013-2017

Certifications

- Therapeutic Medical Physics Part 1, The American Board of Radiology

Publications:

- Kishan, A. U., Ma, T. M., Lamb, J. M., Casado, M., Wilhalme, H., Low, D. A., Sheng, K., Sharma, S., Nickols, N. G., **Pham, J**., Yang, Y., Gao, Y., Neylon, J., Basehart, V., Cao, M., & Steinberg, M. L. (2023). Magnetic Resonance Imaging-Guided vs Computed Tomography-Guided Stereotactic Body Radiotherapy for Prostate Cancer: The MIRAGE Randomized Clinical Trial. *JAMA oncology*, *9*(3), 365–373. https://doi.org/10.1001/jamaoncol.2022.6558
- Xu, D., Ma, T. M., Savjani, R., **Pham, J.**, Cao, M., Yang, Y., Kishan, A. U., Scalzo, F., & Sheng, K. (2023). Fully automated segmentation of prostatic urethra for MR-guided radiation therapy. *Medical physics*, *50*(1), 354–364. https://doi.org/10.1002/mp.15983
- **Pham, J.**, Savjani, R. R., Yoon, S. M., Yang, T., Gao, Y., Cao, M., Hu, P., Sheng, K., Low, D. A., Steinberg, M., Kishan, A. U., & Yang, Y. (2022). Urethral Interfractional Geometric and Dosimetric Variations of Prostate Cancer Patients: A Study Using an Onboard MRI. *Frontiers in oncology*, *12*, 916254. https://doi.org/10.3389/fonc.2022.916254
- **Pham, J.**, Cao, M., Yoon, S. M., Gao, Y., Kishan, A. U., & Yang, Y. (2022). Dosimetric Effects of Air Cavities for MRI-Guided Online Adaptive Radiation Therapy (MRgART) of Prostate Bed after Radical Prostatectomy. *Journal of clinical medicine*, *11*(2), 364. https://doi.org/10.3390/jcm11020364
- Gao, Y., **Pham, J.**, Yoon, S., Cao M., Hu P., & Yang Y. (2021). Recent Advances in Functional MRI to Predict Treatment Response for Locally Advanced Rectal Cancer. *Curr Colorectal Cancer Rep* **17**, 77–87. https://doi.org/10.1007/s11888-021-00470-x
- Gao, Y., Yoon, S., Savjani, R., **Pham, J.**, Kalbasi, A., Raldow, A., Low, D. A., Hu, P., & Yang, Y. (2021). Comparison and evaluation of distortion correction techniques on an MR-guided radiotherapy system. *Medical physics*, *48*(2), 691–702. https://doi.org/10.1002/mp.14634
- **Pham, J.**, Savjani, R. R., Gao, Y., Cao, M., Hu, P., Sheng, K., Low, D. A., Steinberg, M., Kishan, A. U., & Yang, Y. (2021). Evaluation of T2-Weighted MRI for Visualization and Sparing of Urethra with MR-Guided Radiation Therapy (MRgRT) On-Board MRI. *Cancers*, *13*(14), 3564. https://doi.org/10.3390/cancers13143564
- **Pham, J.**, Harris, W., Sun, W., Yang, Z., Yin, F. F., & Ren, L. (2019). Predicting real-time 3D deformation field maps (DFM) based on volumetric cine MRI (VC-MRI) and

artificial neural networks for on-board 4D target tracking: a feasibility study. *Physics in medicine and biology*, *64*(16), 165016. https://doi.org/10.1088/1361-6560/ab359a

Presentations:

- ***Pham J***, Colbert C, Cao M, Nguyen K, Yang Y, "Ferumoxytol Relaxivity and Signal Enhancement for MR-guided radiation therapy (MRgRT) at 0.35T: A Feasibility Study", American Association of Physicists in Medicine (AAPM) Annual Meeting, poster, 2022
- ***Pham J***, Savjani R, Yoon SM, Yang T, Gao Y, Cao M, Hu P, Sheng K, Low D, Steinberg M, Kishan A, Yang Y, "Urethral Interfractional Geometric and Dosimetric Variations of Prostate Cancer Patients: A Study Using an Onboard MRI", American Association of Physicists in Medicine (AAPM) Annual Meeting, poster, 2022
- ***Pham J***, Gao Y, Low D, Hu P Yang Y, "Reduced Field-Of-View Diffusion Weighted MRI On An MR-Guided Radiotherapy System", American Association of Physicists in Medicine (AAPM) Annual Meeting, poster, 2021
- ***Pham J***, Savjani R, Yoon S, Gao Y, Cao M, Hu P, Sheng K, Low D, Steinberg M, Kishan A, Yang Y, "Urethra Inter-Fractional Geometric Variations of Prostate Cancer Patients: A Study Using an On-Board MRI", American Association of Physicists in Medicine (AAPM) Annual Meeting, poster, 2021
- ***Pham J***, Cao M, Kishan A, Yang Y, "Dosimetric Effects of Air Cavities for MRI-Guided Online Adaptive Radiation Therapy (MRgART) of Prostate Bed After Radical Prostatectomy", American Association of Physicists in Medicine (AAPM) Annual Meeting, poster, 2021
- Gao Y, ***Pham J***, Kalbasi A, Radlow A, Hu P, Yang Y, "Comparison and Validation of Distortion Correction on a Low-Field MR-Guided Radiotherapy System", American Association of Physicists in Medicine (AAPM) Annual Meeting, oral presentation, 2020
- ***Pham J***, Savjani R, Gao Y, Cao M, Hu P, Sheng K, Low D, Steinberg M, Kishan A, Yang Y, "Evaluation of T2-Weighted MRI Pulse Sequences for Visualization and Sparing of Urethra with MR-Guided Radiation Therapy (MRgRT) On-Board MRI", American Association of Physicists in Medicine (AAPM) Annual Meeting, poster, 2020
- ***Pham J***, Harris W, Wenzheng S, Yin F-F, Lei R, "Adaptive Boosting and Multilayer Perceptron Neural Network (ADMLP-NN) for Predicting Real-Time 3D Deformation Field Maps (DFM) for 4D Target Tracking", American Association of Physicists in Medicine (AAPM) Annual Meeting, oral presentation, 2019
- Harris W, Wenzheng S, ***Pham J***, Yin F-F, Lei R, "Predicting Real Time 3D Deformation Field Maps (DFM) based on Volumetric Cine MRI (VC-MRI) and Artificial Neural Networks for On-board 4D Target Tracking", American Association of Physicists in Medicine (AAPM) Annual Meeting, oral presentation, 2018

Chapter 1. Introduction

1.1 Stereotactic Body Radiation Therapy for Prostate Cancer

Prostate cancer is the most common cancer among men and is third to lung and colon cancer in absolute annual mortality (1). Treatment options for prostate cancer include active surveillance (for low-risk patients and favorable intermediate-risk disease), radical prostatectomy, brachytherapy, and external beam radiotherapy. In conventional radiotherapy, patients are treated in 39 to 45 fractions with 1.8 to 2.0 Gy each fraction. Prostate cancer has been shown to have low α/β ratios (~1.5 Gy), suggesting it may be more radiosensitive to higher doses per fractions than surrounding bladder and rectum normal tissues (3-5 Gy) (2). As a result, larger fractionated dose schedules have been investigated with the aim to achieve higher therapeutic ratios than conventional fractionation.

Initial randomized clinical trials using 2.4-3.4 Gy for 20-30 fractions, also known as moderate hypofractionation, showed the efficacy, safety, and superiority of larger fractionated dose (3–6). Furthermore, with advancement in image-guidance and radiation therapy delivery techniques, larger fractionated dose escalations were proposed, ultimately bringing the introduction of stereotactic body radiation therapy (SBRT). SBRT utilizes implanted fiducial x-ray and computed tomography (CT)-based patient positioning and tracking, and intensity modulated radiation therapy (IMRT) to deliver large ($\geq$ 5 Gy) and highly conformal fractionated dose for five or fewer fractions. The PACE-B clinical trial and a pooled SBRT consortium report demonstrated SBRT had comparable biochemical control rates as conventional fractionation and moderate hypofractionation while significantly reducing treatment time and cost (7,8) . As a result, SBRT has been recognized as an accepted curative standard-of-care option for very low

through very high-risk prostate cancer patients by the National Comprehensive Cancer Network (NCNN).

Although SBRT improves treatment efficiency, larger fractionated dose increases the risk of acute and late genitourinary (GU) and gastrointestinal (GI) toxicity. It is estimated the acute ($\leq$ 90 days from start of treatment) grade $\geq$ 2 GU and toxicity rates are 29.1% and 16.0% and late (> 90 day from start of treatment) grade $\geq$ are 12.0% and 2.0% (7–9). GU and GI toxicity stem from radiosensitivity of critical structures such as the bladder and rectum (10,11). Clinically, SBRT treatment plans are optimized to minimize dose to these critical structures, however, they may still receive unwarranted high dose due to their proximity to the target. Additionally, SBRT utilizes 2-5 mm treatment margins to ensure adequate target prescription dose coverage. Target margins are designed to account for target volume delineation uncertainty, patient setup errors, inter-fraction variation, and intra-fraction motion, however, larger margins increase the risk of treatment toxicity.

1.2 Stereotactic Body Radiation Therapy for Prostate Bed after Radical Prostatectomy

As mentioned, radical prostatectomy is an alternative treatment option for prostate cancer patients. However, some patients with adverse pathologic features and or unfavorable genomic risk score are of high risk to biochemical recurrence (12–15). Furthermore, it has been shown that 25 to 40% of patients will experience biochemical recurrence after radical prostatectomy (16–19). Therefore, patients with high risk of biochemical occurrence or with biochemical recurrence after radical prostatectomy are recommended for post-operation radiation therapy in the form adjunct radiotherapy or salvage radiotherapy. Currently, conventionally fractionated radiotherapy (1.8 Gy over 30-33 daily fractions) directed to the prostate bed is the only curative standard of care for post-operative patients. Despite its efficacy, post-operative radiation therapy

is underutilized due its prolonged treatment times and financial burden (20–22). Promising biochemical control rates and reduced treatment times from intact prostate SBRT has motivated the exploration of SBRT for prostate bed after radical prostatectomy.

A challenge in treating prostate bed, not seen in intact prostate cases, is the clinical target volume (CTV) is nontrivially defined and highly deformable (23). Moreover, the CTV position and dose coverage are significantly influenced by inter-fraction and intra-fraction deformation of the bladder and rectum (24,25). Pre-treatment bladder filling and rectum emptying instructions can be used to minimize inter-fraction bladder and rectum variation. However, daily patient setup using cone beam CT (CBCT) has poor soft-tissue contrast and imaging artifacts, resulting in limited daily CTV and organ visualization. Additionally, implanted fiducial markers can be utilized to monitor intra-fraction CTV motion. However, implanting fiducials is an invasive procedure, requires frequency x-ray imaging, and ultimately is tracking a proxy of the target rather than the target directly. Due to limited imaging and high anatomic uncertainty, large planning margins (5-7 mm) must still be used to account for daily variations, increasing the risk of treatment toxicity (26).

1.3 MR-guided Radiation Therapy

The development of MR-guided radiation therapy (MRgRT) systems, particularly the ViewRay 0.35T MRIdian system (Cleaveland, OH, USA) has enabled the potential of reducing prostate and prostate bed (after prostatectomy) SBRT treatment planning margins, and subsequently reducing treatment toxicity. Magnetic resonance imaging (MRI) provides good soft tissue contrast, which has shown to improve prostate and organ visualization and allow for smaller prostate target volumes and reduced target volume delineation uncertainty (27). Treatment on MRgRT systems avoid MR-CT registration uncertainty (1-2 mm) as on-board

planning MRIs can be acquired with the patient in treatment position (28). Prior to treatment, daily on-board MRIs allow for radiation-free and fiducial-free patient setups. Additionally, treatment plans can be adapted based on the inter-fraction anatomic variation, which is critical for highly deformable structures like the bladder and rectum (29,30). During treatment, real-time MR cine images can be acquired to directly monitor target and organ intra-fraction motion, enabling treatment gating with automatic beam hold (31,32).

In a prospective phase II MR-guided SBRT study by Bruynzeel et al, MRgRT was delivered in 5 fractions of 7.25 Gy to the target volume using daily plan adaptation (33). Acute grade ≥ 2 GU and GI toxicity were reported at a rate of 19.8% and 3.0%, which is favorable to the estimated 29.1 and 13.3%. MRgRT has demonstrated improved critical structure sparing capabilities and superior treatment toxicity reduction than CT-based treatment. However, SBRT treatment toxicity remains prevalent and the mechanisms behind the radiation-induced damage is not understood well enough to accurately constrain the treatment, as most treatment guidelines are based on empirical data from conventional fractionation.

1.4 Specific Aims

The goal of this dissertation is to evaluate and develop new tools and features provided by MRgRT to help manage prostate cancer and prostate bed SBRT treatment. We hypothesize that the 0.35T MRgRT workflow with electron density corrected adaptive planning will improve dose accuracy and allow for better daily dose constraint management. Furthermore, we hypothesize that 0.35T on-board MRI will provide sufficient urethra contrast for urethra delineation and enable urethra dose-constraining treatment planning and adaptation to mitigate SBRT GU toxicity. Lastly, we hypothesize utilizing longitudinal and granular dose-volume histograms (DVHs) provided by daily on-board MRI will provide comprehensive information on

urinary substructures to establish prognostic biomarkers for predicting prostate SBRT treatment toxicity. The following specific aims focus on developing key analysis and methodologies to accomplish the goal:

- Specific Aim #1 (SA1): Evaluate dosimetric impact of air cavities for 0.35T MR-guided online adaptive radiation therapy (MRgART) for prostate bed patients after prostatectomy
- Specific Aim #2 (SA2): Develop and evaluate urethral imaging using 0.35T MRgRT on-board MRI for urethra constraining prostate cancer treatment planning and adaptation
- Specific Aim #3 (SA3): Develop and evaluate toxicity model for prostate MRgRT SBRT patients based on longitudinal and granular dose-volume histogram (DVH) information

1.5 Overview

Chapters 2, 3 and 4 contain versions of pulished manuscripts written based core on projects of this dissertation. Two additional manuscripts (Chapter 5 and 6) are being journal reviewed. Each chapter consists of an introduction section that thoroughly addresses the study motivation and background.

SA1 is addressed in Chapter 2. Initial phantom studies with dosimeters comparing dose calculation and experimental verification demonstrated dose distortion from air cavity under a 0.35T magnetic field. This motivated us to explore the dosimetric impact of daily air cavities for prostate bed patients with highly deformable organs. Chapter 2 describes the MR-guided online adaptive radiation therapy (MRgART) workflow proposed for prostate bed with daily air cavity

variations. Chapter 3 addresses SA2 and describes the development of a urethral imaging sequence that we have proposed for urethral dose constraining treatment planning. Furthermore, in Chapter 3, the proposed urethra sequence was used to monitor urethra inter-fractional geometric and dosimetric variation to determine the clinical significance of on-board urethra visualization for urethra-focused MRgART. Chapter 5 addresses SA3, where a method to identify dosimetric predictors of GU toxicity, utilizing fraction-wise dose volume histogram metrics, based on a planning dose registration surrogate method, of urinary structures/substructures, is described. Chapter 6 is provided as a technical note and complimentary to Chapter 5 as it validates the use of the planning dose registration method as a surrogate for the daily dose distribution for treatment response analysis.

Chapter 2. Dosimetric Effects of Air Cavities for MRI-Guided Online Adaptive Radiation Therapy (MRgRT) of Prostate Bed after Radical Prostatectomy

A version of this chapter has been published in Journal of Clinical Medicine: Pham J, Cao M, Yoon SM, Gao Y, Kishan AU, Yang Y. Dosimetric Effects of Air Cavities for MRI-Guided Online Adaptive Radiation Therapy (MRgART) of Prostate Bed after Radical Prostatectomy. *J Clin Med*. 2022;11(2):364. Published 2022 Jan 12. doi:10.3390/jcm11020364

2.1 Introduction

MRgRT systems combine a MRI scanner with a linear accelerator (LINAC) radiation therapy system. The integrated MRI scanner allows for radiation-free on-board imaging with superior soft tissue contrast as opposed to conventionally used x-ray-based on-board imaging. Furthermore, MRI serves as a great tool for accurate tumor and critical structure contouring, enabling tighter treatment margins for dose escalation and treatment toxicity reduction (33). Additionally, on-board MRI allows for accurate daily patient setup, which can be further utilized for MRgART (34). Lastly, real-time cine MRIs can be acquired during treatment for soft-tissue-based gating (31).

MRgRT has allowed for more personalized treatment, but it has also introduced new treatment variables, not previously considered in conventional external beam radiation therapy (EBRT). In particular, the effects of the magnetic field on the radiation beam have been a primary concern for patients being treated on MRgRT systems. The presence of the magnetic field decreases surface dose due to the elimination of electron contamination (35). However, secondary electrons affected by the magnetic field can also contribute to out-of-field doses,

delivering unwarranted dose to nearby structures (36). Most notably, traveling electrons, generated within the body by the irradiating beam, are redirected by the Lorentz's force from the perpendicular magnetic field. In homogeneous tissue, the Lorentz force alters the point spread kernel to be asymmetrical, resulting in an asymmetrical penumbra. At tissue-to-air-interfaces, some electrons are subjected to the electron return effect (ERE), in which the Lorentz force redirects the electrons back upstream to the tissue, resulting in increased tissue dose deposition and potentially treatment hotspots. Therefore, the ERE also creates treatment cold spots at distal air-tissue interfaces (35,37,38)

Monte Carlo modeling has been verified, using EBT3 film and thermoluminescent dosimeter measurements in water-based phantoms, to accurately simulate the dosimetric impact of 0.35 T and 1.5 T magnetic fields on air-tissue interfaces and is used clinically in MRgRT treatment planning systems (TPS) for accurate dose calculation (36,39–41). Okamoto et al. and Cusumano et al. showed 0.35 T ^{60}Co Monte Carlo simulations on a phantom with water and air gaps was able to achieve a gamma index (dose difference threshold of 3%/ distance to agreement threshold of 3 mm) passing rate greater than 95% (42,43). Similarly, Shortall et al. showed 1.5 T 7 MV photon Monte Carlo simulation on a polymethyl methacrylate-air phantom was able to achieve a gamma index (3%/3 mm) passing rate greater than 95% (44). For Monte Carlo simulation to accurately calculate the dosimetric perturbation caused by the air cavities, an accurate electron density needs to be obtained, which can be directly converted from Hounsfield Units (HU) on computed tomography (CT) images. However, most clinical MRgRT treatment planning is based on MR images where the electron density is usually determined using either image registration to CT or bulk density assignment.

A widely adopted MRgRT treatment planning workflow, using the 0.35 T ViewRay MRIdian 6 MV LINAC (ViewRay Inc., Oakwood Village, OH, USA), starts with acquiring both simulation CT and MR images, where the MR image is used as the planning image. Electron density, used in ViewRay TPS Monte Carlo dose calculation, is obtained by deformably registering the simulation CT to the planning MR. Furthermore, prior to each treatment fraction, a daily MR image is acquired for patient setup and for use with online adaptive therapy if that is determined to be necessary, in which case planning contours will be updated and the simulation CT will be re-registered to the daily MRI to provide electron density for adaptive plan recalculation or re-optimization.

In addition to patient daily anatomic changes, air cavities in the gastrointestinal tract can vary greatly between initial simulation and subsequent treatment delivery days. Due to the ERE, daily air cavity variations can potentially lead to deviations of the delivered dose from the planning distribution for abdominal and pelvic treatments (45–47). Uilkema et al. generated 1.5 T 6-MV intensity-modulated radiation therapy (IMRT) plans on 10 rectal cancer patients planning CTs with real air cavities and showed a maximum dosimetric endpoint difference between 1.5 T and no magnetic field of 3% (48). Scripes et al. generated 1.5 T 7-MV IMRT plans on four rectal cancer patient planning CTs with artificial air cavities and showed that the planning target volume (PTV) hot spot dose and size increased with increasing air cavity size (49). PTV hot spot doses increased as much as 10% for 5 cm cylindrical diameter air cavity relative to no air cavity.

Although MRI-CT deformable registration is fast and generally considered acceptable in obtaining electron densities for soft tissues and bones, the uncertainty associated with air cavities and their impact on dose calculations is unknown. Furthermore, some adaptive workflows use

bulk average electron density assignments on the daily MRI structure from the corresponding simulation CT structure, ignoring structure inhomogeneities and air cavities (50). As a result, depending on disappearing or appearing daily air cavities, the electron density of the daily structure will be systematically increased or decreased, resulting in inaccurate dose calculations (51,52).

Currently, due to time constraints, daily air cavity contouring and electron density correction is not routinely considered in pelvic MRgART to specifically address its variation and dosimetric uncertainty. Therefore, in this study, the dosimetric impact of air cavities were retrospectively evaluated in a cohort of post-radical prostatectomy patients treated with SBRT on our 0.35 T MRgRT LINAC system. Similar to prior air cavity studies, artificial air cavities were generated in a prostate bed patient planning CT (48,49). However, patient dose will be influenced by a 0.35 T magnetic field rather than at 1.5 T. Although the magnitude of the ERE is expected to be less with 0.35 T than 1.5 T (weaker Lorentz force), the dosimetric difference has not been quantified. Additionally, the dosimetric impact of artificial and real air cavities in prostate bed daily MRI is evaluated, where the electron density is obtained from deformable registration with a simulation CT. Furthermore, the dosimetry between MRgART air cavity electron density corrected and non-corrected (only deformable registration) plans is compared.

2.2 Material and Methods

2.2.1 Dosimetric Impact of Artificial Air Cavities in Prostate Bed Patient Planning CT on a 0.35T MRgRT system

A prostate bed patient (Patient A) with negligible planning CT air cavities was selected. Artificial tubular air cavities (diameters 0–3 cm, 0.5 cm increments) were generated along the patient's planning CT rectum in MIM Software (Cleveland, OH, USA) and bulk air density

assigned in the ViewRay TPS. Figure 2-1 shows Patient A's electron density maps with planning CT contours and different size artificial tubular air cavities.

Three 0.35 T treatment plans were generated for each air cavity size using the ViewRay TPS: (1) single anterior–posterior (AP) beam, (2) opposing AP–PA beams, and (3) clinical IMRT with 15 beams. For the single AP plan, a 5 cm × 5 cm AP beam was used to deliver 5 Gy to the isocenter (center of PTV). Similarly, for the opposing AP–PA plan, two equally weighted 5 cm × 5 cm AP and PA beams were used to deliver 5 Gy to the isocenter (2.5 Gy each). For both plans, the dose distribution was calculated on the CT without an air cavity (0 cm) using a grid resolution of 0.3 cm and the magnetic field effect on. Afterwards, both plans were forward calculated on the CTs with various air cavity sizes (0.5–3 cm) using dose uncertainty of 1%.

Electron Density Map

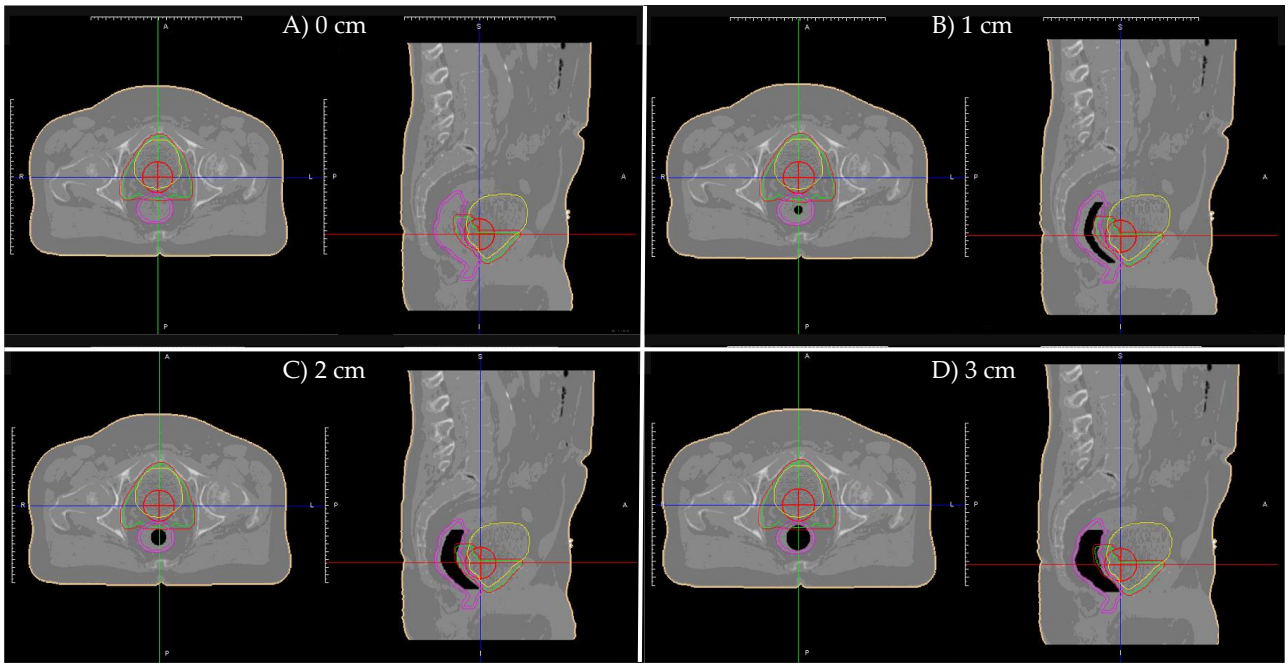

Figure 2-1. Patient A's planning CT electron density maps with artificial tubular air cavities of diameters: (**A**) 0 cm; (**B**) 1 cm; (**C**) 2 cm; and (**D**) 3 cm. Planning CT contours displayed: Red—planning target volume (PTV); Green—clinical target volume (CTV); Yellow—bladder; Pink—rectum/rectal wall; Red cross—isocenter

For the clinical IMRT plan, 15 equally arced beams were placed around the isocenter (PTV) and 32 Gy was prescribed to 95% of the PTV (5 fraction (Fx); 6.4 Gy/Fx). Dose was optimized on the CT without the air cavity using our clinical constraints (Table 2-1), a grid resolution of 0.2 cm, and the magnetic field effect turned on. The optimized plan was forward calculated on the CTs with the selected air cavity sizes using dose uncertainty of 1%.

Table 2-1. Clinical IMRT constraints for prostate bed patients.

Constraint	
PTV V32	≥ 95%
Bladder Max	≤ 35.7 Gy
Bladder V35.7	≤ 0.03 cc
Bladder V32.5	≤ 35%
Rectum Wall V24	≤ 50%
Rectum Max	≤ 35.7 Gy
Rectum V35.7	≤ 0.03 cc
Rectum V33.75	≤ 25%
Rectum V32.5	≤ 30%
Rectum V27.5	≤ 45%

2.2.2 Dosimetric Impact of Artificial Cavities Air Cavities in Prostate Bed Patient Daily MRI, with Electron Density Obtained from Deformable Registration to Simulation CT, on a 0.35 T MRgRT System

A different prostate bed patient (Patient B), with negligible simulation CT and daily MRI air cavities, was selected. Artificial tubular air cavities (diameter 0–3 cm, 0.5 cm increments) were generated along the patient's daily MRI rectum and masked with a signal intensity of 0 in MIM Software, simulating daily appearing air cavities that are not present during the initial CT simulation. In ViewRay TPS, the daily MRIs with various air cavity sizes were each deformably registered to the simulation CT for electron density mapping and treatment planning. Figure 2-2 shows Patient B's daily MRI with different size artificial tubular air cavities and corresponding electron density map from deformable registration with simulation CT. Notably, deformed electron density maps were unable to recreate daily MRI air cavities, resulting in inaccurate daily MRI electron density maps for dose calculation.

Two 0.35 T MRgART treatment plans were generated for each daily MRI air cavity size using ViewRay TPS: Plan 1—'Deformed' and Plan 2—'Override'. In the 'Deformed' plan, a clinical IMRT plan with 15 equally arced beams around the daily PTV was generated on the

daily MRI, with electron density map obtained from the registered simulation CT, to deliver 32 Gy to 95% of the PTV. Dose was optimized using the same constraints as in Table 2-1, grid resolution of 0.3 cm, and magnetic field effect on. In the 'Override' plan, daily MRI air cavities were corrected and bulk assigned air density on the registered simulation CT's electron density map. Afterwards, the 'Deformed' plan was forward calculated on the daily MRI with a dose uncertainty of 1%.

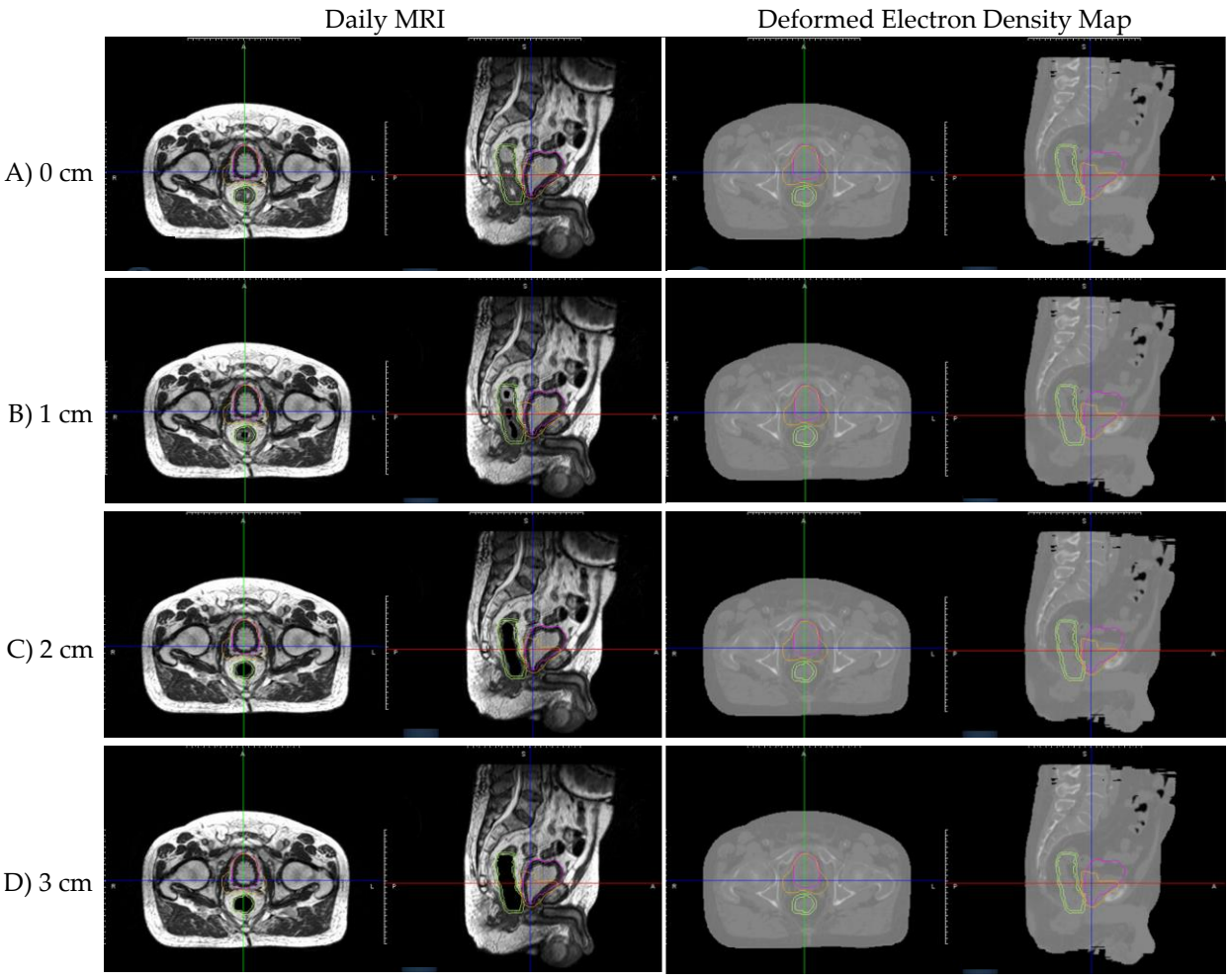

Figure 2-2. Patient B's daily MRI with artificial tubular air cavities of diameter (**A**) 0 cm, (**B**) 1 cm, (**C**) 2 cm, and (**D**) 3 cm, and corresponding electron density map from deformable registration with simulation CT. Notably, deformed electron density maps were unable to recreate daily MRI air cavities, resulting in inaccurate daily MRI electron density maps. Daily MRI contours displayed: Pink—bladder; Orange—PTV; Green—rectum/rectal wall.

2.2.3 Dosimetric Impact of Real Air Cavities in Prostate Bed Patient Daily MRI, with Electron Density Obtained from Deformable Registration to Simulation CT, on a 0.35 T MRgRT System

Five prostate bed patients (Patient 1–Patient 5) with non-negligible daily MRI air cavities were selected. Prior to simulation and each daily MRI fraction, patients were instructed to follow institutional bladder and rectum filling protocol. After simulation, an initial clinical 0.35 T MRgRT IMRT plan was generated on the planning MRI with electron density obtained from deformable registration to simulation CT. Initial clinical IMRT plans for the five prostate bed patients used 13–17 beams arced around the PTV to deliver 32 Gy to 95% of the PTV. Dose was optimized using the same constraints as in Table 2-1, grid resolution of 0.3 cm, and magnetic field effect on.

For each patient, the two fractions (Fraction A and Fraction B), with the largest volume daily MRI air cavities, were selected to simulate the adaptive planning process. Planning MRI contours were updated to the daily MRI anatomy by a resident radiation oncologist and reviewed by the attending physician in MIM Software. Afterwards, in ViewRay TPS, each daily fraction MRI was deformably registered to its simulation CT.

Two 0.35 T MRgART treatment plans were prepared for each fraction using the ViewRay TPS: Plan 1—'Deformed' and Plan 2—'Override'. In the 'Deformed' plan, the initial clinical plan was forward calculated on the daily MRI with an electron density map obtained from the registered simulation CT. In the 'Override' plan, simulation CT and daily MRI air cavities were manually corrected and bulk assigned water and air density on the registered simulation CT's electron density map, respectively. Afterwards, the initial clinical plan was forward calculated. For 'Deformed' and 'Override' plans, the initial clinical plan was forward calculated with dose uncertainty of 1%. Figure 2-3 shows Patient 3 Fraction A's daily MRI,

corresponding deformed simulation CT, deformed electron density map ('Deformed'), and corrected daily air cavity electron density map ('Override'). Daily MRI and deformed simulation CT display significantly different air cavities. White arrows indicate workflow for obtaining daily air cavity corrected electron density map. After daily air cavity correction, the 'Override' electron density map more accurately represents the daily MRI's electron density.

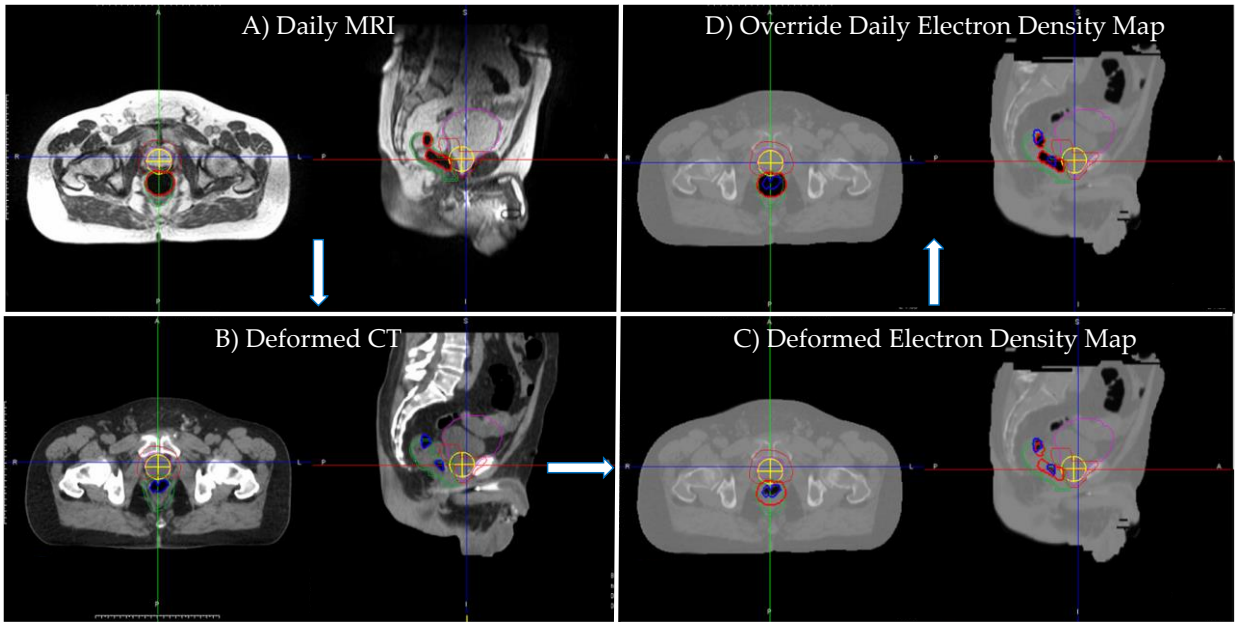

Figure 2-3. Patient 3 Fraction A's (**A**) daily MRI, (**B**) corresponding deformed simulation CT, (**C**) deformed planning electron density map ('Deformed') and (**D**) corrected daily air cavity electron density map ('Override'). Daily MRI and deformed simulation CT display significantly different air cavities. White arrows indicate workflow for obtaining daily air cavity corrected electron density map. After daily air cavity correction, the 'Override' electron density map more accurately represents the daily MRI's electron density. Daily MRI contours displayed: Pink—bladder; Orange—PTV; Green—rectum/rectal Wall; Red—daily MRI air cavity; Yellow cross—isocenter. Simulation CT contour displayed: Blue—simulation CT air cavity.

2.2.4 Dosimetric Evaluation

For the artificial planning CT air cavities (Section 2.2.1), prostate bed (Patient A) AP, AP–PA and clinical IMRT plan dose difference maps, for each air cavity size (0.5–3 cm), relative to no air cavity (0 cm), were calculated and normalized to each respective plan's

prescribed PTV dose. Planning CT target/organ mean and max dose difference were evaluated. Additionally, AP dose-depth curves along the isocenter were plotted for all air cavity sizes and plans.

For the artificial daily MRI air cavities (Section 2.2.2), prostate bed (Patient B) dose difference maps between 'Deformed' and 'Override' plans for each air cavity size (0.5–3 cm), were calculated. Similarly, daily MRI target/organ mean and max dose difference were evaluated.

For the real daily MRI air cavities (Section 2.2.3), prostate bed (Patients 1–5) air cavity volume changes, between simulation CT and daily MRIs (Fractions A and B), were calculated. Furthermore, the clinical significance of MRgART air cavity electron density corrections were evaluated based on the clinical constraint changes. The MRgART air cavity electron density correction was considered significant if the 'Deformed' plan passed the clinical constraint, but the 'Override' plan did not, or vice-versa.

2.3 Results

2.3.1 Dosimetric Impact of Artificial Air Cavities in Prostate Bed Patient Planning CT on a 0.35 T MRgRT System

Figure 2-4 shows prostate bed Patient A's AP plan dose and dose difference maps for 0, 1, 2, and 3 cm diameter artificial planning CT air cavities. Similarly, Figures 2-5 and 2-6 shows the AP–PA and clinical IMRT plan dose and dose difference maps. Figure 2-7 shows the AP dose-depth curve, along the isocenter, for varying air cavity sizes with AP, AP–PA, and clinical IMRT plans. For the AP and AP–PA plan, hot and cold spots within the rectum significantly increased in magnitude and size (relative to no air cavity) with increasing air cavity size due to the ERE, where the 3 cm air cavity resulted in a 20%/17% and 13%/13% increase to the

rectum/rectal wall max dose, respectively. ERE, for the AP–PA and clinical plan, were dominated by the posterior beams due to smaller attenuation on the posterior end of the target. As a result, the hot and cold spots appear rotated relative to the AP plan. Overall, the magnitude and size of the hot spot decreased when multiple beams were used as the dose was more uniformly spread across the body and the ERE was averaged-out by opposing beams. The clinical IMRT dose, with multiple optimized equally arced beams, was robust to air cavity size and deviations remained within dose calculation uncertainty (1%). The complete target/organ max and mean dosimetric change for each air cavity size and plan can be found in Section 2.6 Appendix (Table 2-3).

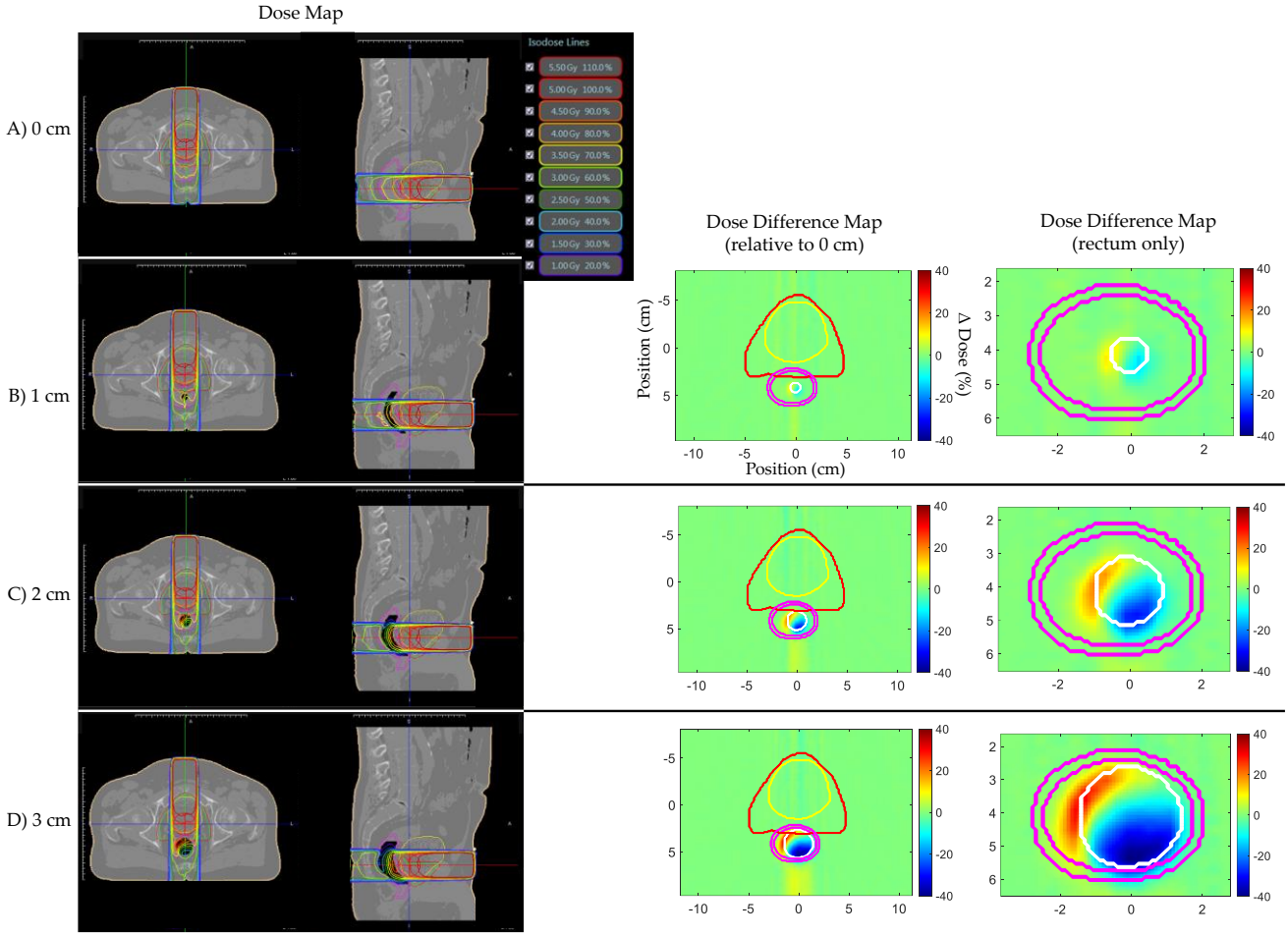

Figure 2-4. Prostate bed Patient A's AP plan dose distributions (overlaid on planning CT electron density map) and dose difference (ΔDose (%)) maps for (**A**) 0, (**B**) 1, (**C**) 2, and (**D**) 3 cm artificial planning CT air cavity. Rectum dose difference maps show hot and cold spots within the rectum increased in magnitude and size with increasing air cavity size due to the electron return effect (ERE). Dose difference map planning CT contours displayed: Red—PTV; Yellow—bladder; Pink—rectum; White—artificial air cavity.

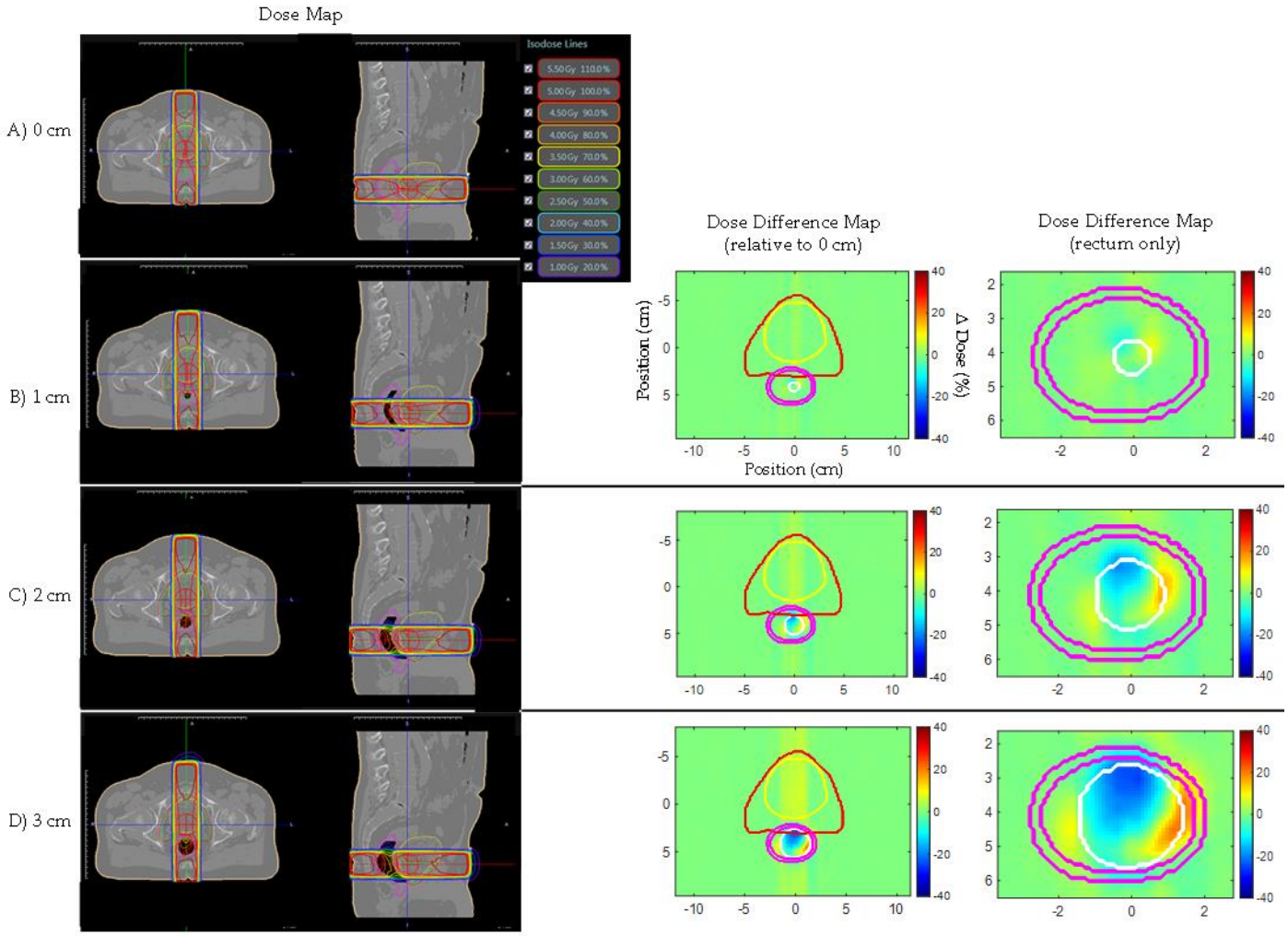

Figure 2-5. Prostate bed Patient A's AP–PA plan dose maps (overlaid on planning CT electron density map) and dose difference (ΔDose (%)) maps for (**A**) 0, (**B**) 1, (**C**) 2, and (**D**) 3 cm artificial planning CT air cavity. Rectum dose difference maps show hot and cold spots within the rectum increased in magnitude and size with increasing air cavity size due to the electron return effect (ERE). Dose difference map planning CT contours displayed: Red—PTV; Yellow—bladder; Pink—rectum; White—artificial air cavity.

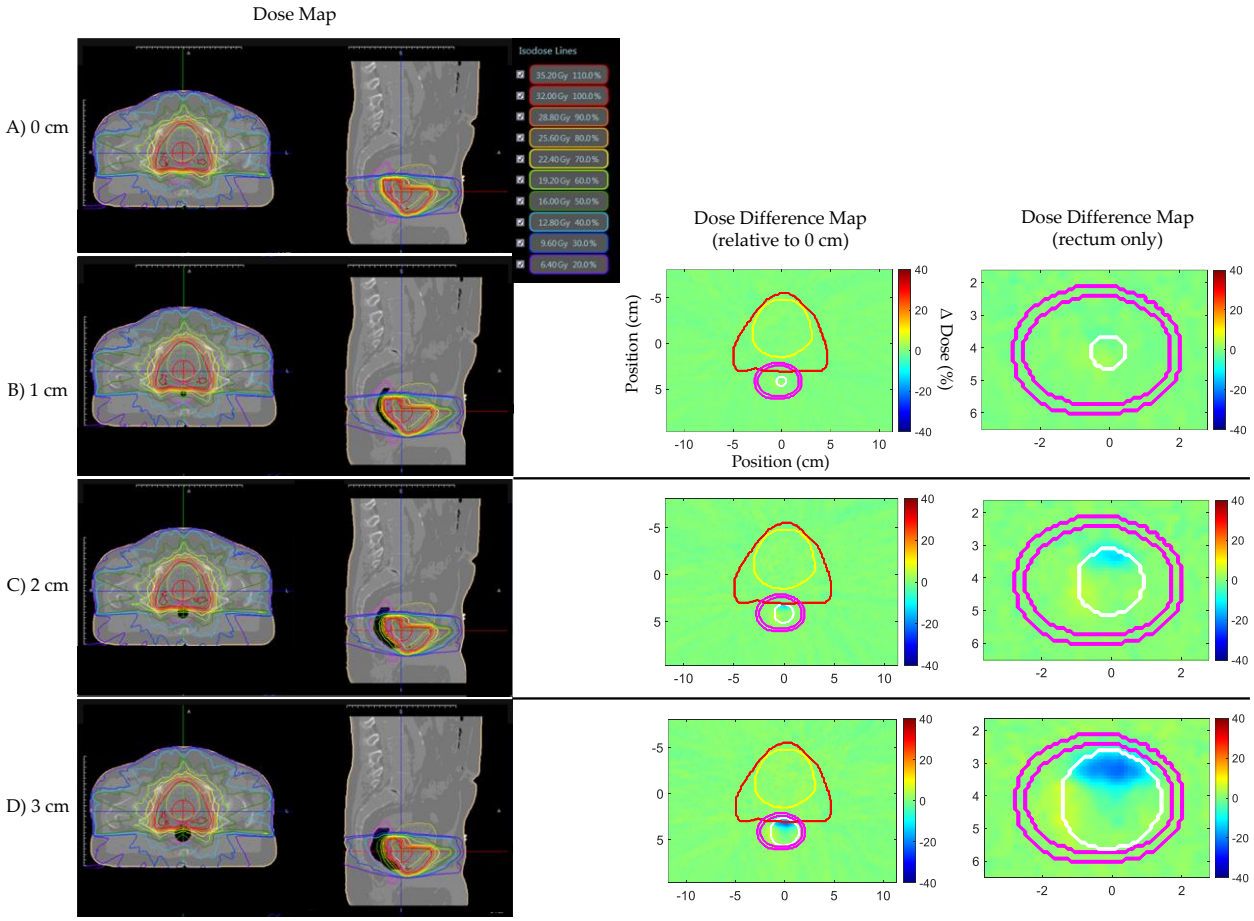

Figure 2-6. Prostate bed Patient A's clinical IMRT plan dose maps (overlaid on planning CT electron density map) and dose difference (ΔDose(%)) maps for (**A**) 0, (**B**) 1, (**C**) 2, and (**D**) 3 cm artificial planning CT air cavity. Rectum dose difference maps show little to no dose change within the rectum for different air cavity sizes due to dose being uniformly spread and the electron return effect (ERE) being averaged-out by multiple opposing beams. Dose difference map planning CT contours displayed: Red—PTV; Yellow—bladder; Pink—rectum; White—artificial air cavity.

A) AP

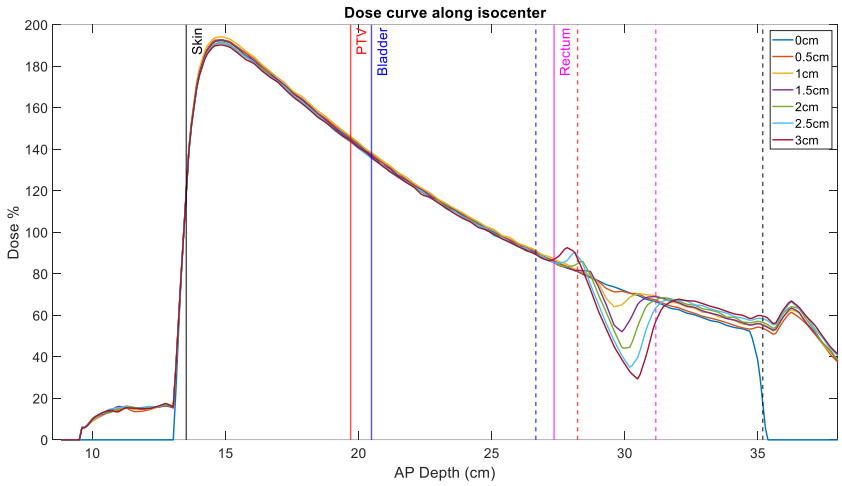

B) AP-PA

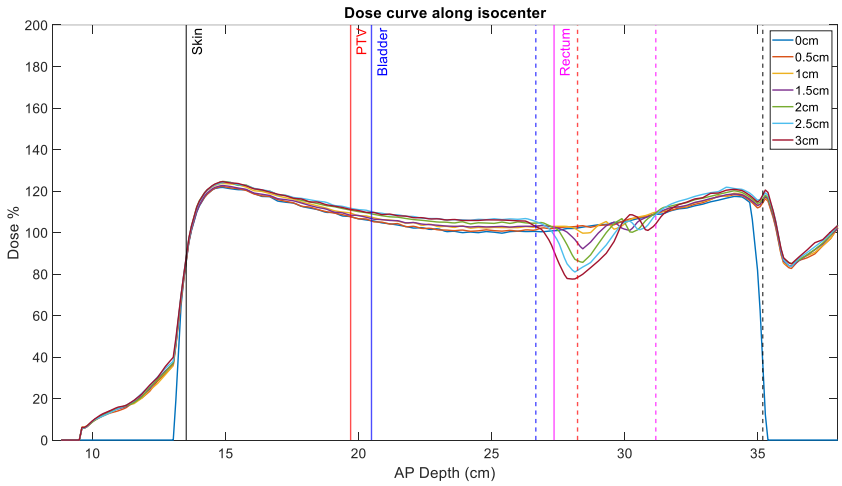

C) Clinical IMRT

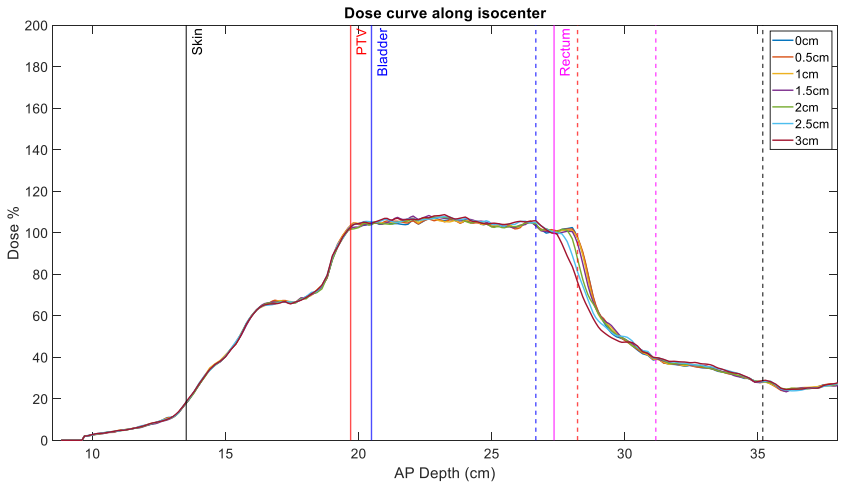

Figure 2-7. Prostate bed Patient A's AP dose-depth curve, along the isocenter, for varying air cavity sizes with (**A**) AP, (**B**) AP–PA, and (**C**) clinical IMRT plans (normalized by respective plan's prescribed PTV dose). Clinical IMRT dose is more robust to air cavity sizes than AP and

AP–PA plans and shows little deviation. Solid lines—planning CT target/organ start, dashed lines—planning CT target/organ end.

2.3.2 Dosimetric Impact of Artificial Cavities Air Cavities in Prostate Bed Patient Daily MRI, with Electron Density Obtained from Deformable Registration to Simulation CT, on a 0.35 T MRgRT System

As shown in Figure 2-2, daily MRI deformable registration with simulation CT is unable to create daily MRI appearing air cavities on the resulting electron density map. Figure 2-8 shows prostate bed Patient B's 'Deformed' and 'Override' plans' dose and dose difference maps for 1, 2, and 3 cm artificial daily MRI air cavities. Target/organ mean and max dose difference was relatively small (<4%) even though deformable registration was not able to attain electron density for the air cavities. Furthermore, no noticeable dose trend as a function of air cavity size was observed.

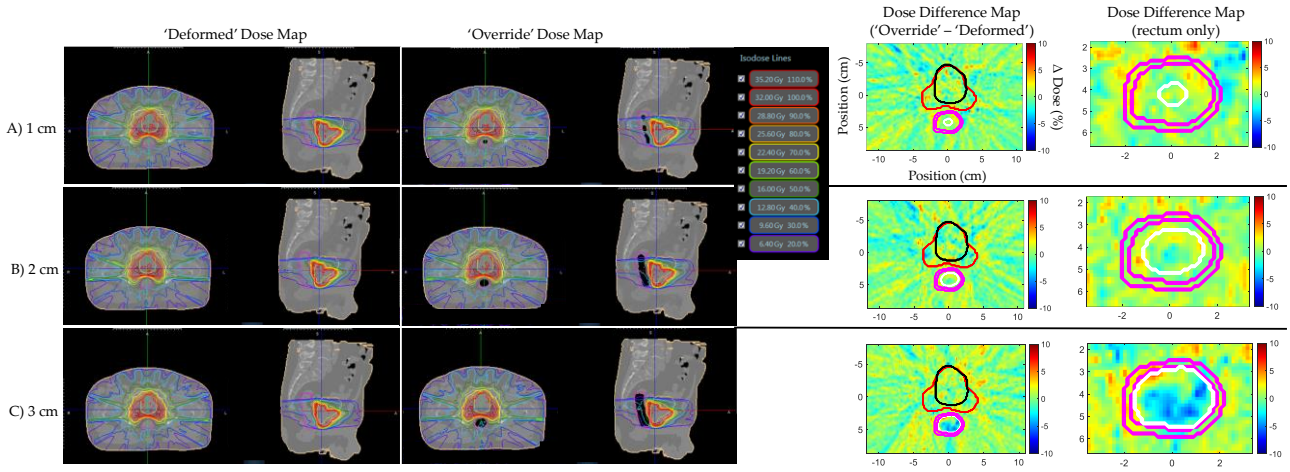

Figure 2-8. Prostate bed Patient B's 'Deformed' and 'Override' plan dose and dose difference maps for (**A**) 1, (**B**) 2, and (**C**) 3 cm artificial daily MRI air cavities. Target/organ mean and max dose difference was relatively small (<4%) despite air cavity correction in the 'Override' plan. Dose difference map daily MRI contours displayed: Red—PTV, Black—bladder, Pink—rectum, White—artificial air cavity.

2.3.3 Dosimetric Impact of Real Air Cavities in Prostate Bed Patient daily MRI on a 0.35 T MRgRT System, with Electron Density Obtained from Deformable Registration to Simulation CT,

For prostate bed Patients 1–5 Fraction A and B, the mean (range) air cavity size change between daily MRI and simulation CT was 5.69 ± 10.07 cc (−7.8 to + 22.9 cc), where positive and negative air cavity change represented increasing and decreasing air volumes, respectively.

Table 2-2 shows the mean dose constraint change between 'Deformed' and 'Override' plans for all patient fractions based on respective daily MRI with real air cavities. The complete daily constraint and change for each plan, patient and fraction can be found in Section 2.6 Appendix (Table 2-4). The dosimetric difference between 'Deformed' and 'Override' plans did not lead to change in clinical adaptive decision except for two fractions (Patient 3 Fraction A and Patient 4 Fraction B). In these fractions, the 'Override' plan, with air cavity electron density correction, indicated that the bladder D_{max} dose and rectum V35.7 exceeded the respective constraint, while the 'Deformed' plan, without correction, showed acceptable dose, although the absolute differences were only 0.3 Gy and 0.03 cc, respectively. Overall, clinical constraint changes between 'Deformed' and 'Override' plans were minimal.

Table 2-2. Mean constraint change between 'Deformed' and 'Override' plans for all patient (Patient 1–5) fractions (Fraction A and B) based on respective daily MRI with real air cavities.

Constraint	Change
PTV V32	−0.27 ± 0.27%
Bladder Max	−0.01 ± 0.24 Gy
Bladder V35.7	0.04 ± 0.12 cc
Bladder V32.5	0.09 ± 0.87%
Rectum Wall V24	−0.25 ± 0.37%
Rectum Max	−0.07 ± 0.50 Gy
Rectum V35.7	0.00 ± 0.01 cc
Rectum V33.75	−0.17 ± 0.37%
Rectum V32.5	−0.46 ± 0.66%
Rectum V27.5	−0.72 ± 1.01%

2.4 Discussion

This study evaluated the dosimetric impact of air cavities in prostate bed patients' rectums on a 0.35 T MRgRT system. Artificial tubular air cavities of a range of sizes (0–3 cm) were generated on a prostate bed patient's planning CT and three different plans (AP, AP–PA, clinical IMRT), were retrospectively evaluated. In the AP and AP–PA plans, the rectum and rectal wall hotspot magnitude and size increased with increasing air cavity size. The AP–PA plan hot spot dose was lower than the AP plan and was further reduced using clinical IMRT. The use of opposing beams counter-balance and average-out the effect of the ERE from each beam, reducing the magnitude and size of the resulting hot spots (45,47). Comparing our clinical IMRT results with a previous artificial air cavity clinical IMRT study (49) using a 3 cm air cavity, the maximum rectum hot spot change (relative to 0 cm) was expectedly smaller for 0.35 T (1%) (Table 2-3) than 1.5 T (6%).

In our second experiment, artificial tubular air cavities were generated on a prostate bed patient's daily MRI, and electron density information was obtained using deformable registration with simulation CT. Deformed electron density maps were unable to reproduce daily MRI air

cavities due to deformation transformation not able to create air cavity density in the electron density map ; however, the dose differences between air cavity electron density corrected ('Override') and uncorrected ('Deformed') clinical IMRT plans were minimal (< 4%) due to beam averaging and low magnetic field strength. Therefore, prostate bed dose calculation, based on electron density directly derived from MR-CT deformable registration, is acceptable for various rectal air cavity sizes under a low strength magnetic field.

Lastly, MRgART air cavity electron density correction was evaluated on prostate bed patients' daily MRI with real air cavities. Daily clinical constraint changes between 'Deformed' and 'Override' plan were minimal, although large variations of air cavity sizes were observed. MRgART air cavity electron density corrections were considered clinically significant if: (1) The 'Deformed' plan failed clinical constraints while the 'Override' plan passed; or (2) the 'Deformed' plan passed clinical constraints while the 'Override' plan failed. In Scenario 1, the 'Deformed' plan constraints failing would suggest the need for further plan adaptation; however, if the correct daily air electron density was used, plan adjustment would not be necessary, reducing treatment time. In Scenario 2, the 'Deformed' plan constraints passing would suggest plan adjustment was not needed based on deformably registered CT only; however, further plan adaptation is actually necessary when the correct air cavity electron density is used. Of the 10 real patients' air cavity fractions, two fractions followed Scenario 2, indicating air cavity electron density correction was necessary to improve prostate bed IMRT constraints. Despite this, the absolute difference between the 'Deformed' and the 'Override' plans were small in these cases. Furthermore, air cavity electron density correction is a time-intensive procedure that requires daily air cavity segmentation and plan re-calculation or re-optimization. As a result, MRgART, based on daily anatomical change was sufficient (53), and the need for additional air cavity

electron density correction to detect small dosimetric changes was not warranted at the cost of longer treatment times.

This study has several limitations. First, our real air cavity patient cohort size was small (5 patients, 2 fractions each). A larger patient cohort would include patients with different size and shape air cavities. However the current patient cohort had a large range of air cavity sizes and the dosimetric change from air cavity electron density correction was negligible. Second, this study used ViewRay, vendor-specific, deformable registration to obtain electron density maps for daily MRIs. Deformable registration algorithms, using machine learning or a more accurate deformation transformation method, can be used between daily MRI and simulation CT for potentially more accurate electron density mapping (54). Despite potential improvements in electron density accuracy, manual air cavity electron density correction used in this study resulted in small dosimetric differences with little to no clinical significance. Lastly, this study used Viewray, vendor-specific, Monte Carlo dose calculation, which may use underlying model assumptions to accelerate dose calculation and thus is not generalizable to other systems. However, Khan et al. developed a general vendor-independent Monte Carlo 0.35 T/6 MV MR-LINAC model using GEANT4 code and was able to show good agreement with ViewRay TPS results (55). Therefore, our results, using ViewRay TPS Monte Carlo dose calculation, is a reasonable estimation of the dosimetric impact of air cavities in prostate bed patients on a 0.35 T MRgRT system.

2.5 Conclusion

Clinical 0.35 T IMRT prostate bed plans are dosimetrically robust to rectum air cavity size when multiple beam angles are used, resulting in only small dosimetric deviations stemming from the ERE. Moreover, 0.35 T ERE dosimetric deviations are smaller than 1.5 T. Despite strict

bladder and rectum filling protocols, air cavity size change between simulation and daily treatment are still present. Daily MRI electron density maps obtained from deformable registration with simulation CT, are unable to produce accurate daily air cavity electron densities. However, 0.35 T MRgART plan recalculation or re-optimization, with air cavity electron density correction, shows small and clinically insignificant dosimetric change relative to uncorrected deformed electron density plans. Therefore, MRgART air cavity electron density correction is not necessary for prostate bed patients treated with clinical IMRT on low-field MRgRT systems.

2.6 Appendix

Table 2-3 shows prostate bed Patient A's AP, AP–PA, and clinical IMRT planning CT target/organ max and mean dose difference (relative to 0 cm) for each air cavity size,

Table 2-3. Prostate bed Patient A's AP, AP–PA, and clinical IMRT planning CT target/organ max and mean dose difference (relative to 0 cm) for each air cavity size.

AP Plan										
Air Cavity Radius (cm)	**CTV Max**	**CTV Mean**	**PTV Max**	**PTV Mean**	**Bladder Max**	**Bladder Mean**	**Rectum Max**	**Rectum Mean**	**Rectum Wall Max**	**Rectum Wall Mean**
0.5	2%	0%	2%	0%	0%	0%	0%	0%	0%	0%
1	2%	0%	2%	0%	0%	0%	0%	0%	0%	0%
1.5	0%	0%	0%	0%	0%	0%	5%	0%	0%	0%
2	−1%	0%	−1%	0%	−1%	0%	10%	0%	3%	0%
2.5	−1%	0%	−1%	0%	−1%	0%	17%	−1%	10%	0%
3	0%	0%	0%	0%	−1%	0%	20%	−1%	13%	0%
AP–PA Plan										
0.5	0%	0%	0%	0%	1%	0%	0%	0%	0%	0%
1	1%	0%	2%	0%	1%	0%	2%	0%	0%	0%
1.5	1%	0%	1%	0%	2%	1%	7%	0%	0%	0%
2	4%	0%	4%	0%	3%	1%	11%	0%	2%	0%
2.5	4%	1%	5%	0%	4%	1%	15%	−1%	8%	0%
3	4%	1%	6%	1%	4%	2%	17%	−1%	13%	0%
Clinical IMRT Plan										
0.5	0%	0%	0%	0%	0%	0%	0%	0%	0%	0%
1	−1%	0%	−1%	0%	0%	0%	1%	0%	1%	0%
1.5	0%	0%	0%	0%	1%	0%	1%	1%	1%	0%
2	0%	0%	0%	0%	1%	0%	1%	1%	1%	0%
2.5	1%	0%	1%	0%	1%	0%	1%	0%	1%	1%
3	1%	0%	1%	0%	1%	0%	1%	0%	0%	1%

Table 2-4 shows ‘Deformed’ and ‘Override’ plan daily constraint and change (Δ) for Patients 1–5 and Fractions A and B based on daily MRI with real air cavities.

Table 2-4. ‘Deformed’ (DE) and ‘Override’ (OV) plan daily constraint and change between plans (Δ) for each patient (Patient 1–5) and fraction (Fraction A and B) based on daily MRI with real air cavities. Red and black constraint values indicate failed and passing. Green constraint change values indicates scenarios where ‘Deformed’ plan passed the constraint, but ‘Override’ failed.

Patient	PTV V32 (%)			Bladder Max (Gy)			Bladder V35.7 (cc)			Bladder V32.5 (%)			Rectum Wall V24 (%)		
	DE	OV	Δ	DE	OV	Δ	DE	OV	Δ	DE	OV	Δ	DE	OV	Δ
Patient 1 Fraction A	79.95	79.97	0.02	36.36	36.16	−0.2	0.2	0.15	−0.05	40.55	40.61	0.06	15.38	15.37	−0.01
Patient 1 Fraction B	87.42	86.74	−0.68	35.48	35.23	−0.25	0	0	0	13.57	14.09	0.52	25.53	24.58	−0.95
Patient 2 Fraction A	93.2	92.45	−0.75	34.87	34.68	−0.19	0	0	0	73.71	71.92	−1.79	16.26	16.27	0.01
Patient 2 Fraction B	94.34	94.2	−0.14	35.92	36.04	0.12	0.01	0.02	0.01	48.99	48.79	−0.2	18.1	18.1	0
Patient 3 Fraction A	91.94	91.72	−0.22	35.48	35.8	0.32	0	0.02	0.02	21.34	21.22	−0.12	17.46	16.73	−0.73
Patient 3 Fraction B	92.15	91.68	−0.47	35.48	35.53	0.05	0	0	0	21.15	21.1	−0.05	17.52	17.14	−0.38
Patient 4 Fraction A	90.75	90.74	−0.01	37.52	37.35	−0.17	4.27	4.25	−0.02	39.63	39.63	0	10.63	10.56	−0.07
Patient 4 Fraction B	94.73	94.7	−0.03	36.34	36.84	0.5	0.5	0.9	0.4	24.44	24.41	−0.03	21.22	21.56	0.34
Patient 5 Fraction A	85.91	85.57	−0.34	36.5	36.41	−0.09	0.18	0.26	0.08	29.54	30.14	0.6	14.61	14.16	−0.45
Patient 5 Fraction B	87.06	87.01	−0.05	36.23	36.06	−0.17	0.03	0.02	−0.01	31.84	33.76	1.92	12.63	12.41	−0.22
Patient	**Rectum Max (Gy)**			**Rectum V35.7 (cc)**			**Rectum V33.75 (%)**			**Rectum V32.5 (%)**			**Rectum V27.5 (%)**		
	DE	OV	Δ	DE	OV	Δ	DE	OV	Δ	DE	OV	Δ	DE	OV	Δ
Patient 1 Fraction A	34.35	34.44	0.09	0	0	0	0.31	0.4	0.09	2.25	2.34	0.09	7.83	7.83	0
Patient 1 Fraction B	34.85	34.92	0.07	0	0	0	0.66	0.61	−0.05	5.85	3.64	−2.21	15.5	12.03	−3.47
Patient 2 Fraction A	32.84	32.9	0.06	0	0	0	0	0	0	0.04	0.07	0.03	7.96	7.98	0.02
Patient 2 Fraction B	33.13	33.12	−0.01	0	0	0	0	0	0	0.31	0.37	0.06	8.54	8.47	−0.07
Patient 3 Fraction A	34.76	34.57	−0.19	0	0	0	0.46	0.29	−0.17	2.36	1.76	−0.6	8.47	7.29	−1.18
Patient 3 Fraction B	34.76	34.65	−0.11	0	0	0	0.46	0.28	−0.18	2.36	1.75	−0.61	8.45	7.35	−1.1
Patient 4 Fraction A	34.97	35.26	0.29	0	0	0	0.27	0.33	0.06	0.86	0.9	0.04	3.94	3.89	−0.05
Patient 4 Fraction B	35.78	36.24	0.46	0.01	0.04	0.03	3.67	2.42	−1.25	5.91	5.19	−0.72	12.02	11.87	−0.15
Patient 5 Fraction A	34.85	34.94	0.09	0	0	0	0.09	0.1	0.01	0.67	0.5	−0.17	5.49	4.75	−0.74
Patient 5 Fraction B	35.09	33.62	−1.47	0	0	0	0.24	0	−0.24	0.68	0.13	−0.55	5	4.52	−0.48

Chapter 3. Evaluation of T2-Weighted MRI for Visualization and Sparing of Urethra with MR-Guided Radiation Therapy (MRgRT) On-Board MRI

A version of this chapter has been published Cancers Journal: Pham J, Savjani RR, Gao Y, et al. Evaluation of T2-Weighted MRI for Visualization and Sparing of Urethra with MR-Guided Radiation Therapy (MRgRT) On-Board MRI. *Cancers (Basel)*. 2021;13(14):3564. Published 2021 Jul 16. doi:10.3390/cancers13143564

3.1 Introduction

Stereotactic body radiation therapy (SBRT) has become a standard of care option for prostate cancer patients, utilizing a large-fractionated dose to shorten treatment times. Recent SBRT reports with large prostate cancer patient cohorts have shown SBRT to have comparable biochemical control and toxicity rates to conventional treatments (56–58). Despite improvements in treatment efficiency, patients are still reporting acute and late gastrointestinal (GI) and genitourinary (GU) toxicities. GU toxicities can arise due to complications along the GU tract (59). In the past, attention has primarily been focused on sparing the bladder despite the significant contributions of urethral injury to GU toxicities mainly due to difficulty in localizing the urethra.

Delineating the prostatic urethra on CT is challenging due to the urethral wall and prostate having the same physical density and average atomic number (60). Furthermore, on-board cone beam CT (CBCT) in linear accelerators (LINACs) has poor image quality, making it impossible to visualize the urethra during treatment. The prostatic urethra can vary in size, shape, and length from patient to patient, but on average is approximately 3.5 cm long and 0.8 cm wide

(61,62). Currently, there are no consensus guidelines for contouring the urethra. The use of a Foley catheter has been used to localize and visualize the urethra on CT. However, this method must be done prior to each treatment, is invasive and can lead to infection. Additionally, the catheter can also rotate and deform the urethra, resulting in potential organ misalignment during each treatment delivery (63–65). As a result, some physicians choose to contour the prostatic urethra on the planning CT based on prior experience and knowledge. However, this is unreliable and can be inconsistent between radiation oncologists and centers.

Alternatively, MRI provides superior soft-tissue contrast and proper MRI sequences may be used to improve prostatic urethra conspicuity. T2-weighted (T2w) MRIs can make the urethra appear more hyperintense (59), and are currently used in radiation therapy urethra contouring by registering diagnostic T2w MRI to the planning CT. However, the associated MR to CT registration can be challenging due to differences in tissue contrast between the two imaging modalities, as well as the potentially different shape and location of the urethra on MRI and CT, which is often acquired on different days with different patient position (66).

Delineating the urethra enables various urethra sparing techniques for reducing GU toxicities. Urethra sparing is most commonly implemented by limiting hotspots in the urethra as encouraged in PACE-B (56) and ongoing NRG-GU 005 trials. This method lowers GU toxicity and avoids loss of efficacy. Moreover, limiting hotspots can enable dose escalation elsewhere for aggressive disease and improve biochemical control while maintaining acceptably low rates of toxicity (67). Urethra dose de-escalation has also been attempted (33,68,69) but is not commonly used due to the high risk of recurrence at the periurethral areas (70).

In a study by VU Medical Center in Amsterdam (VUMC), prostate cancer patients, undergoing urethra-sparing SBRT using MR-guided radiation therapy (MRgRT), showed lower rates of GU toxicity (33,68,69). Besides tighter planning target volume margins and on-line adaptation enabled by on-board MRI, the urethra was also delineated and used for urethra sparing with dose de-escalation. In their study, the urethra was contoured on one sagittal MR slice from the balanced steady-state free precession (bSSFP) planning MRI and expanded isotopically by 2 mm. However, the T2/T1 weighted contrast of bSSFP is not ideal for urethra visibility and single-slice urethral contouring is limited and can miss the full extent of the urethra.

In this study, we sought to optimize two MRI sequences, 3D half-Fourier acquisition single-shot turbo spin echo (HASTE) and 3D turbo spin echo (TSE) on a commercial MRgRT system for visualization and multi-slice delineation of the prostatic urethra within an MRgRT prostate SBRT workflow. Imaging on an MRgRT system, as opposed to a diagnostic MRI scanner, allows the patient to be in treatment position and avoids additional systematic uncertainties. HASTE and TSE are T2-weighted MR sequences that can directly provide urethral contrast within the prostate. The tradeoff for our proposed sequence is the lower signal-to-noise ratio (SNR), which can degrade urethral visualization, thus urethral contrast and SNR must be optimized by sequence parameters adjustments for adequate urethral localization. We compared prostatic urethra contours in five different workflows: (1) CT-based planning based on CT only (CT-1), (2) CT-based planning based on CT and registered diagnostic T2w 3T MRI (CT-2), (3) MRgRT-based planning with the proposed optimized urethra 3D HASTE (MRgRT-1), (4) MRgRT-based planning with the proposed optimized urethra 3D TSE (MRgRT-2), and (5) MRgRT-based planning with clinical bSSFP MRI (MRgRT-3).

3.2 Materials and Methods

3.2.1 Imaging and Subject Cohort

Eleven prostate cancer patients undergoing radiation therapy between February 2020 and June 2020 were included. Each patient provided written consent prior to the study. Patient planning CT and diagnostic 3T T2w MRI were acquired prior to treatment. For each patient, the proposed 3D HASTE and 3D TSE sequences were used to image the urethra on a 0.35T MRgRT system (MRIdian, ViewRay). Of the 11 patients, eight patients (Patients 1–8) were imaged immediately after one of their treatment fractions and three patients (Patients 9–11) were imaged right after simulation. Additionally, a clinical bSSFP scan was acquired on the MRgRT system, which is currently used for MRgRT treatment planning and patient setup. Although images were acquired at different times, all but the diagnostic MRI were acquired with the patient in their treatment position.

Pelvic CTs were acquired on a 16-slice CT scanner (Sensation Open, Siemens Medical Solutions, Erlangen, Germany) using 120 kVp and 400 mA. CT slice thickness was 1.5–3 mm and in-plane resolutions ranged from 0.90×0.90 mm^2 to 1.27×1.27 mm^2. Diagnostic MRIs were acquired either in 2D or 3D. The scan parameters for the diagnostic T2w MRI, optimized MRgRT HASTE, optimized MRgRT TSE, and clinical MRgRT bSSFP are shown in Table 3-1.

Table 3-1. Sequence parameters used for diagnostic T2W (2D and 3D) MRI, MRgRT 3D HASTE, MRgRT 3D TSE, and clinical MRgRT 3D bSSFP.

Sequence	**Diagnostic T2w MRI**		**MRgRT HASTE**	**MRgRT TSE**	**Clinical MRgRT bSSFP**
Acquisition Type	2D	3D	3D	3D	3D
Acquisition Orientation	Axial	Axial	Sagittal	Sagittal	Axial

Repitition Time (ms)	3530–6000	2200	1800	2000	3.37
Echo Time (ms)	95–130	205	246	250	1.45
Flip Angle	90–160°	110°	90°	90°	60°
Pixel Bandwidth (Hz/Px)	199–273	315	196	351	535
In-plane Resolution (mm^2)	0.3 × 0.3–1.3 × 1.3	0.7 × 0.7	1.5 × 1.5	1.5 × 1.5	1.5 × 1.5
FOV (mm^2)	180 × 180–462 × 399	170 × 170	227 × 400	236 × 399	449 × 499
Phase Encoding Direction	RL	RL	AP	AP	AP
Slice Thickness (mm)	3	1.5	1.5	1.5	1.5
Number of Slices	24–84	60	40	60	192
Parallel Imaging	GRAPPA	GRAPPA	GRAPPA	GRAPPA	None
Acceleration Factor	2–3	2	2	2	N/A
Number of Averages	1–4	2	6	4	1
Acquisition Duration (minutes)	4:00–5:00	7:00	8:06	7:12	1:45

Both 3D HASTE and 3D TSE were qualitatively optimized for urethra visualization on low-field MRgRT using four healthy male volunteers. Echo time (TE), relaxation time (TR), and voxel size were tuned to provide urethra contrast while maintaining sufficient SNR. Additionally, the number of averages was tuned to increase image SNR and minimize motion/ghosting artifacts, while maintaining acceptable scan times. Figures 3-1 and 3-2 show the MRgRT 3D HASTE and MRgRT 3D TSE optimization. Optimization steps for MRgRT 3D HASTE and TSE were similar. Volunteer 1 HASTE 1 and Volunteer 2 TSE 1 (baseline) show a noisy urethra with some urethral contrast. By increasing the number of averages to 6 (HASTE) and 4 (TSE), the scan SNR improved and the final scan time was increased to 8:06 min and 7:14 min, respectively. Increasing TE to 407 ms (Volunteer 2 HASTE 1) resulted in lower SNR, but greater urethral contrast as T2-weighting increased. Conversely, decreasing TE to 135/133 ms (Volunteer 2 HASTE 2/Volunteer 2 TSE 2), resulted in higher SNR, but less urethral contrast as T2-weighting decreased. Increasing TR to 3000 ms (Volunteer 4 TSE 2) slightly improved SNR, but lowered urethral contrast, as prostate and urethral signal intensity were able to fully recover. Ultimately, TE of 246/250 ms and TR of 1800/2000 ms for MRgRT 3D HASTE/TSE was

selected to provide adequate SNR and urethral contrast. Lower resolution (Volunteer 2 HASTE 2 and 3) of 2.0 mm isotropic, compared to 1.5 mm isotropic, provided higher SNR; however, 1.5 mm isotropic was selected to capture the prostatic urethra's fine structure. Lastly, sagittal acquisition was preferred over axial acquisition for easier urethra visualization and delineation.

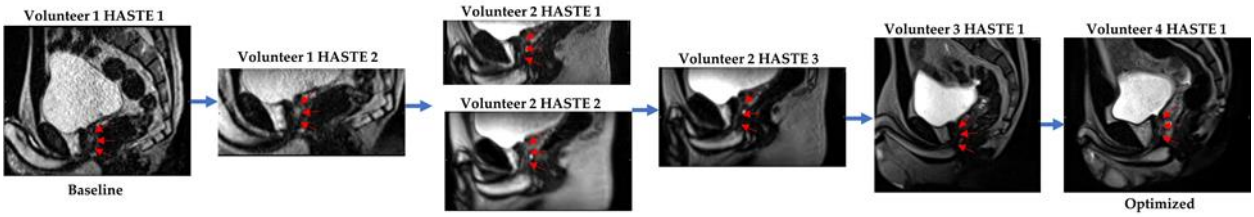

Sequence	Volunteer 1 HASTE 1 (baseline)	Volunteer 1 HASTE 2	Volunteer 2 HASTE 1	Volunteer 2 HASTE 2	Volunteer 2 HASTE 3	Volunteer 3 HASTE 1	Volunteer 4 HASTE 1 (optimized)
Acquisition Type	3D	3D	3D	3D	3D	3D	3D
Acquisition Orientation	Axial	Axial	Axial	Axial	Axial	Sagittal	Sagittal
Relaxation Time (ms)	1800	1800	1800	1800	1800	1800	1800
Echo Time (ms)	296	296	407	135	297	303	246
Flip Angle	90°	90°	90°	90°	90°	90°	90°
Pixel Bandwidth (Hz/Px)	196	196	196	196	196	196	196
In-plane Resolution (mm^2)	1.5 × 1.5	1.5 × 1.5	1.6 × 1.6	2.0 × 2.0	2.0 × 2.0	1.5 × 1.5	1.5 × 1.5
FOV (mm^2)	228 × 399	228 × 399	228 × 399	228 × 399	228 × 399	228 × 399	228 × 399
Slice Thickness (mm)	1.5	1.5	2.0	2.0	2.0	1.5	1.5
Number of Slices	120	60	40	60	60	40	40
Parallel Imaging	GRAPPA	GRAPPA	GRAPPA	GRAPPA	GRAPPA	GRAPPA	GRAPPA
Acceleration Factor	2	2	2	2	2	2	2
Number of Averages	1	2	4	4	4	6	6
Acquisition Duration (minutes)	3:57	3:57	5:24	7:55	7:55	8:06	8:06

Figure 3-1. MRgRT 3D HASTE optimization scheme using healthy male volunteers (red arrows pointing towards prostatic urethra).

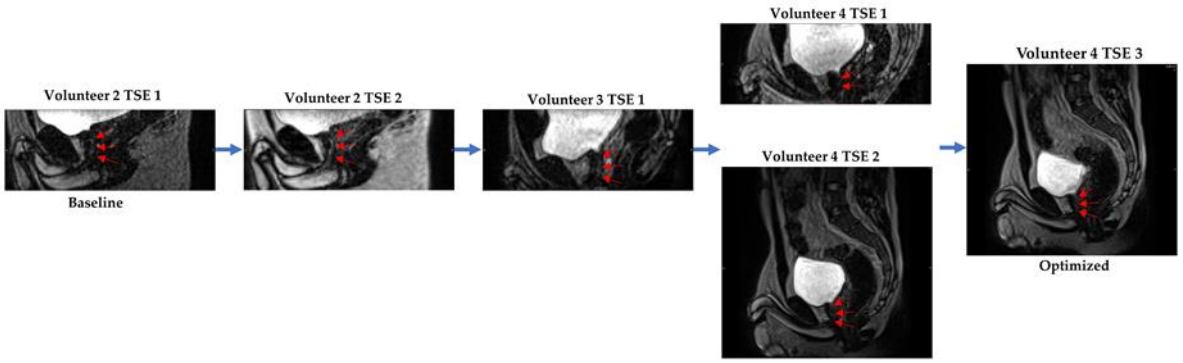

Sequence	Volunteer 2 TSE 1 (baseline)	Volunteer 2 TSE 2	Volunteer 3 TSE 1	Volunteer 4 TSE 1	Volunteer 4 TSE 2	Volunteer 4 TSE 3 (optimized)
Acquisition Type	3D	3D	3D	3D	3D	3D
Acquisition Orientation	Axial	Axial	Axial	Axial	Sagittal	Sagittal
Relaxation Time (ms)	2000	2000	2000	2000	3000	2000
Echo Time (ms)	297	133	250	297	250	250
Flip Angle	90°	90°	90°	90°	90°	90°
Pixel Bandwidth (Hz/Px)	351	351	351	351	351	351
In-plane Resolution (mm^2)	1.5 × 1.5	1.5 × 1.5	1.5 × 1.5	1.5 × 1.5	1.5 × 1.5	1.5 × 1.5
FOV (mm^2)	236 × 399	236 × 399	236 × 399	236 × 399	236 × 399	236 × 399
Slice Thickness (mm)	1.5	1.5	1.5	1.5	1.5	1.5
Number of Slices	60	60	60	60	40	60
Parallel Imaging	GRAPPA	GRAPPA	GRAPPA	GRAPPA	GRAPPA	GRAPPA
Acceleration Factor	2	2	2	2	2	2
Number of Averages	2	2	4	6	4	4
Acquisition Duration (minutes)	3:35	3:35	7:14	10:49	7:14	7:14

Figure 3-2. MRgRT 3D TSE optimization scheme using healthy male volunteers (red arrows pointing towards prostatic urethra).

3.2.2 Urethra Contours

A resident radiation oncologist with over two years of experience contoured the prostatic urethra on each patient's CT sim, registered pre-treatment T2w diagnostic MRI, MRgRT 3D HASTE, and MRgRT 3D TSE MRIs. First, in the CT-1 workflow, the resident radiation oncologist only had access to the patient's CT sim and the prostatic urethra contour was made using anatomical guidelines (71). Second, in the CT-2 workflow, the resident radiation oncologist contoured the prostatic urethra using the patient's CT sim and the diagnostic T2w MRI which had been rigidly registered to the CT. Third, in the MRgRT-1 workflow, the resident radiation oncologist contoured the prostatic urethra using the patient's MRgRT 3D HASTE. Fourth, in the MRgRT-2 workflow, the resident radiation oncologist contoured the prostatic urethra using the patient's MRgRT 3D TSE. Afterwards, an attending radiation oncologist with over eight years of experience reviewed and, if necessary, edited the contours. Lastly, in the

MRgRT-3 workflow, the attending radiation oncologist contoured the prostatic urethra using the patient's clinical MRgRT 3D bSSFP.

3.2.3 Evaluation Metrics

The resident radiation oncologist, attending radiation oncologist, and a senior medical physicist with over 15 years of experience qualitatively scored the urethra visibility for each image on a 4-point scale: 1 = no conspicuity; 2 = some conspicuity, urethra can be identified, but not very clear; 3 = good conspicuity, urethra can be identified clearly; 4 = excellent conspicuity.

Based on the urethra conspicuity scores, MRgRT 3D HASTE in MRgRT-1 workflow had the highest score (Table 3-2) from two out of the three observers and was subsequently used as the reference in quantitative contour evaluation. Specifically, CT, diagnostic MRI, MRgRT 3D TSE, and clinical MRgRT 3D bSSFP were rigidly registered to the MRgRT 3D HASTE based on the prostate gland using MIM Software (Cleveland, OH, USA). Afterwards, the contours in the CT-1, CT-2, MRgRT-2 and MRgRT-3 workflows were compared relative to the contours in the MRgRT-1 workflow (MRgRT 3D HASTE) using the 95th percentile Hausdorff distance (HD95), mean-distance-to-agreement (MDA), and DICE coefficient. The 95th percentile Hausdorff distance was calculated as the 95th percentile surface distance between the contours and was chosen as it was relatively stable to small outliers.

Table 3-2. Observer 1 (OBS1—senior radiation oncologist), observer 2 (OBS2—resident radiation oncologist), and observer 3 (OBS3—senior medical physicist) patient urethra visibility scores for each imaging technique. Qualitative visibility scores: 1 = no conspicuity; 2 = some conspicuity; 3 = good conspicuity; 4 = excellent conspicuity. Wilcoxon signed-rank test statistical significance difference test was used between MRgRT 3D HASTE and different imaging techniques for each respective observer.

Patient	**CT**			**Diagnostic T2w MRI**			**MRgRT 3D HASTE**			**MRgRT 3D TSE**			**Clinical MRgRT 3D bSSFP**		
	OBS1	**OBS2**	**OBS3**	**OBS1**	**OBS2**	**OBS3**	**OBS1**	**OBS2**	**OBS3**	**OBS1**	**OBS2**	**OBS3**	**OBS1**	**OBS2**	**OBS3**
1	1	1	1	(3D) 2	3	3	3	2	4	3	3	3	2	2	2
2	1	1	1	(3D) 2	2	2	3	2	4	2	3	3	1	3	1
3	1	1	1	(2D) 2	2	2	3	3	3	2	2	3	2	3	1
4	1	1	1	(2D) 2	3	2	3	3	3	3	4	4	2	2	2
5	1	1	1	(3D) 3	3	3	4	3	4	3	4	4	3	3	2
6	1	1	1	(2D) 4	3	4	3	3	4	3	3	3	2	3	2
7	1	1	1	(3D) 4	3	4	3	3	3	2	3	3	2	2	2
8	1	1	1	(3D) 3	3	3	3	3	4	2	3	3	1	2	1
9	1	1	1	(2D) 2	4	3	2	3	3	2	3	3	1	3	1
10	1	1	1	(3D) 4	4	4	3	2	3	2	3	3	1	2	1
11	1	1	1	(2D) 4	4	4	4	4	4	3	4	3	2	3	2
Mean	1.0	1.0	1.0	2.9	3.1	3.1	3.1	2.8	3.5	2.5	3.2	3.2	1.7	2.5	1.5
Standard Deviation	0.0	0.0	0.0	0.9	0.7	0.8	0.5	0.6	0.5	0.5	0.6	0.4	0.6	0.5	0.5
p-value	<0.001	<0.001	<0.001	0.732	0.5	0.234	-	-	-	0.02	0.219	0.219	<0.001	0.375	<0.001

Additionally, prostatic urethra contrast-to-noise ratios (CNR) were calculated for each image as follows:

$$\mathrm{CNR}_{\text{Prostatic Urethra}} = \frac{|\text{Prostatic urethra mean intensity - Surrounding prostate mean intensity}|}{\text{Background noise}}. \qquad (3\text{-}1)$$

The prostatic urethra mean intensity was evaluated based on the radiation oncologist's contour. The surrounding prostate mean intensity was evaluated based on a prostate ring contour encompassing the prostatic urethra. The prostate ring contour was made by expanding the prostatic urethra contour 1 cm isotropically then subtracting the original urethra. Both the prostatic urethra and prostate ring contour were cropped to remain within the clinical prostate contour, which was originally made on the planning image and registered/transferred to each image. The entire clinical prostate contour for the prostate mean intensity calculation was not used because the clinical prostate contour often extended into the bladder and would artificially

increase the mean value. The background noise was measured as the standard deviation of the image values inside the prostate ring contour.

The prostatic urethra qualitative and CNR results were compared using the Wilcoxon signed-rank test with a significance level of 0.05.

3.3 Results

Table 3-2 shows the attending radiation oncologist's (Observer 1–OBS1), resident radiation oncologist's (Observer 2—OBS2), and senior medical physicist's (Observer 3—OBS3) qualitative urethra visibility scores for all patient images. All observers scored CT urethra visibility a 1. For Observer 1 and 3, the qualitative scores for MRgRT 3D HASTE were scored significantly higher than CT and clinical MRgRT 3D bSSFP. Observer 1 scored MRgRT 3D HASTE significantly higher than MRgRT 3D TSE, but Observer 3 did not. Furthermore, Observer 2 scored MRgRT 3D HASTE significantly higher than for CT only and not for the other MRI techniques. Two-dimensional (2D) and 3D diagnostic T2w MRI's qualitative scores were not significantly different from MRgRT 3D HASTE for all observers. MRgRT 3D HASTE was scored highest for two out of three observers and was used as a reference for quantitative evaluation.

Figure 3-3 shows Patient 11's (Figure 3-3a) planning CT, (Figure 3-3b) 2D diagnostic T2w MRI, (Figure 3-3c) MRgRT 3D HASTE, (Figure 3-3d) MRgRT 3D TSE, and (Figure 3-3e) clinical MRgRT 3D bSSFP. There is no tissue contrast between the urethra and prostate in the planning CT. In the MRI scans, the contrast is improved in general, but urethra visibility varies with the different MRI sequences. Notably, the diagnostic MRI and MRgRT 3D HASTE and TSE showed fewer motion/ghosting artifacts compared to the MRgRT 3D bSSFP (blue arrow).

Figure 3-4 shows Patient 7's CT and MRgRT 3D HASTE fused images with urethra contours based on CT-1: CT only (yellow), CT-2: CT + diagnostic T2w MRI (green), MRgRT-1: MRgRT 3D HASTE (red), MRgRT-2: MRgRT 3D TSE (blue), and MRgRT-3: clinical MRgRT 3D bSSFP (purple).

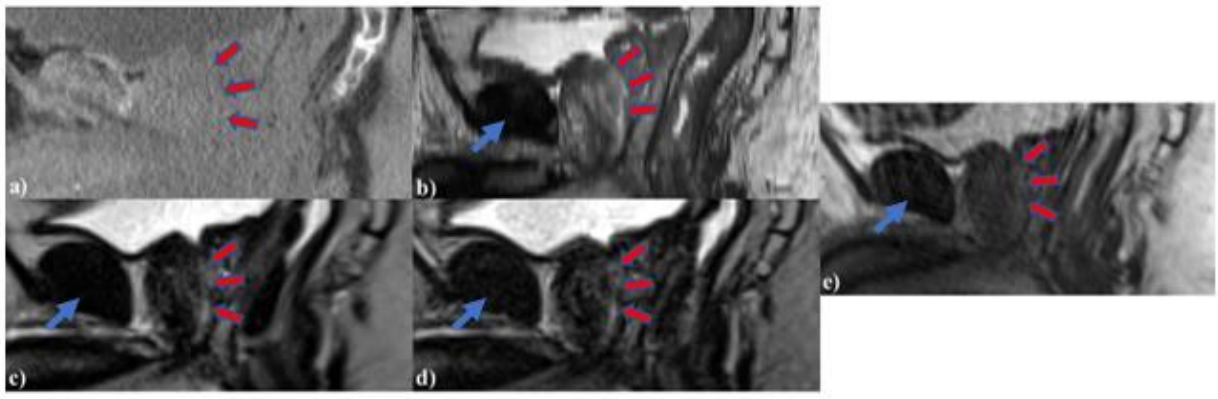

Figure 3-3. Patient 11's (**a**) planning CT, (**b**) 2D diagnostic T2w MRI at 3T, (**c**) MRgRT 3D HASTE, (**d**) MRgRT 3D TSE, and (**e**) clinical MRgRT 3D bSSFP (red arrows pointing to the prostatic urethra). Blue arrows showing different amounts of motion/ghosting artifacts in each MRI image. The clinical MRgRT 3D bSSFP showed significant motion/ghosting artifacts.

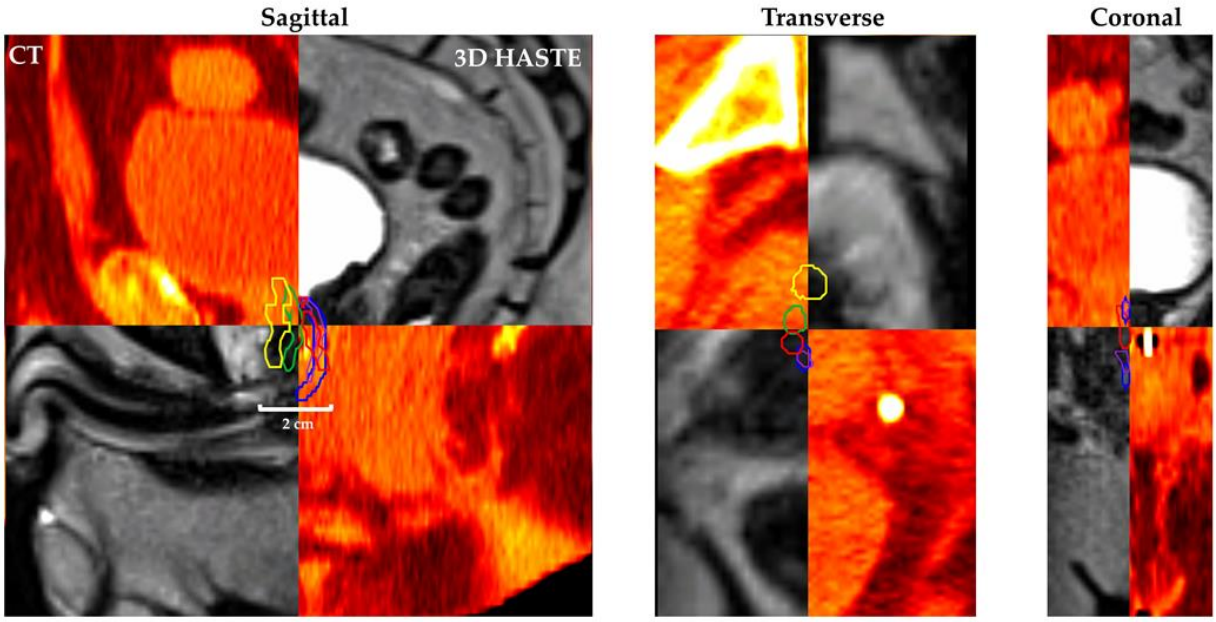

Figure 3-4. Patient 7's CT (red/yellow) and MRgRT 3D HASTE (B–W linear) fused images with urethra contours based on workflow (1) CT-1: CT only (yellow), (2) CT-2: CT + diagnostic T2w MRI (green), (3) MRgRT-1: MRgRT 3D HASTE (red), (4) MRgRT-2: MRgRT 3D TSE (blue), and (5) MRgRT-3: clinical MRgRT 3D bSSFP (purple) prostatic urethra contour.

Figure 3-5 shows the CT-1, CT-2, MRgRT-2 and MRgRT-3 workflows' prostatic urethra contours' HD95, MDA, and DICE coefficient relative to workflow MRgRT-1's prostatic urethra contour. The mean HD95s for workflow CT-1, CT-2, MRgRT-2, and MRgRT-3 were 11.35 ± 3.55 mm, 7.62 ± 2.75 mm, 5.49 ± 2.32 mm, and 6.34 ± 2.89 mm, respectively. Similarly, the mean MDAs were 5.77 ± 2.69 mm, 3.83 ± 1.47 mm, 2.18 ± 1.19 mm, and 2.65 ± 1.31 mm, and the mean DICE coefficients were 0.07 ± 0.08, 0.12 ± 0.10, 0.35 ± 0.19, and 0.21 ± 0.12. Overall, the prostatic urethra contours showed great variance between the different workflows. Urethra contours from the three MRgRT MRIs acquired in common imaging sessions (MRgRT-1, MRgRT-2, and MRgRT-3) showed the smallest variances.

Figure 3-6 shows prostatic urethra CNRs. The mean CNRs for CT, diagnostic T2w MRI, MRgRT 3D HASTE, MRgRT 3D TSE, and clinical MRgRT 3D bSSFP were 0.07 ± 0.05, 0.25 ± 0.14, 0.44 ± 0.25, 0.39 ± 0.29, and 0.24 ± 0.14, respectively. The CNR for MRgRT 3D HASTE was significantly greater than CT ($p < 0.001$), diagnostic T2w ($p < 0.042$), and clinical MRgRT 3D bSSFP ($p < 0.014$), but was not significantly different from MRgRT 3D TSE ($p = 0.465$).

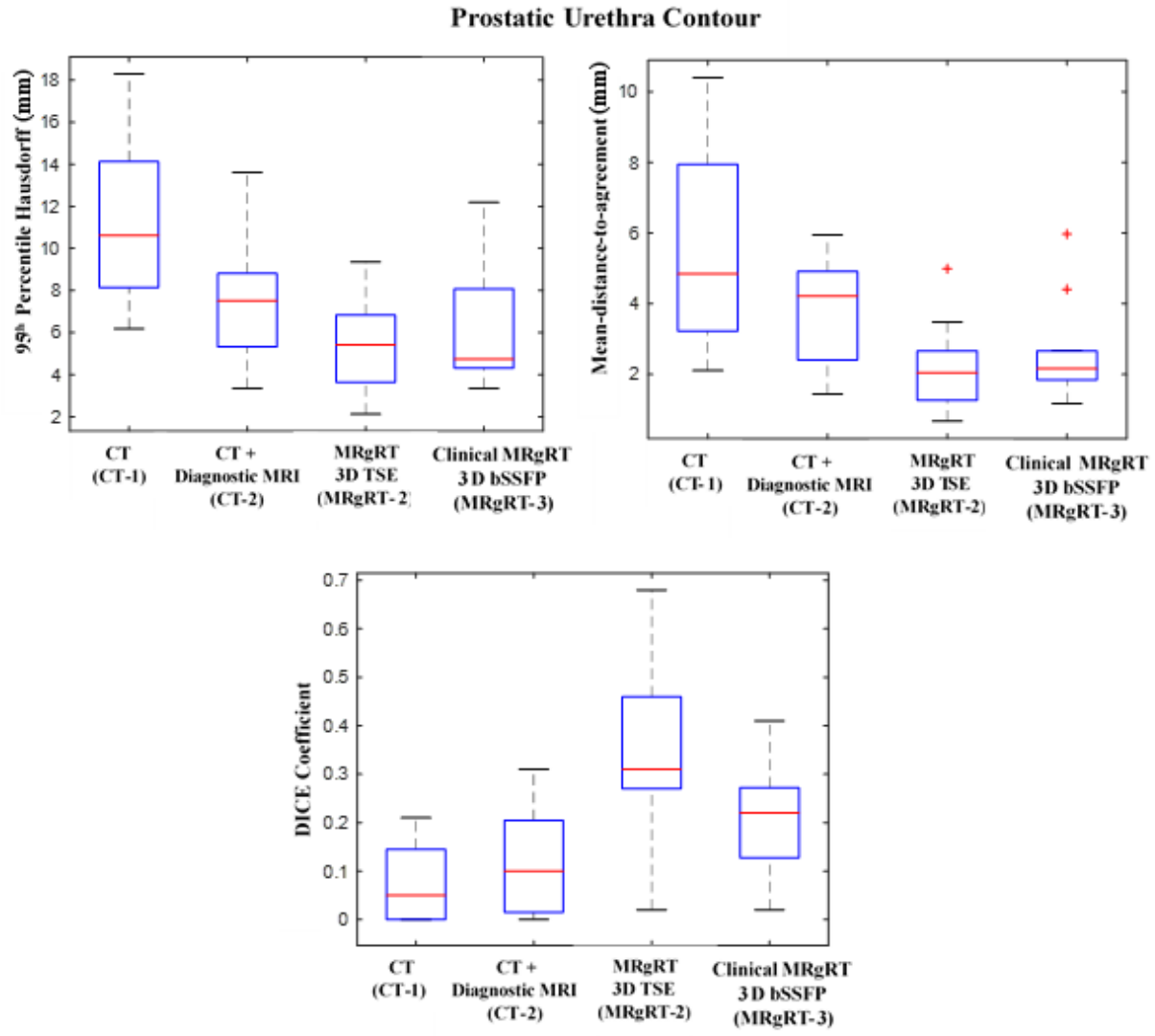

Figure 3-5. Boxplot of 95th percentile Hausdorff distance, mean-distance-to-agreement, and DICE coefficient for CT (CT-1), CT + diagnostic T2w MRI (CT-2), MRgRT 3D TSE (MRgRT-2), and clinical MRgRT 3D bSSFP (MRgRT-3) prostatic urethra contour relative to MRgRT 3D

HASTE's (MRgRT-1) prostatic urethra contour. CT-based planning showed great variability while MRgRT-based planning showed the most consistency. (Red line = median value, top edge of box = 75th percentile, bottom edge of box = 25th percentile, whiskers = extreme data points (not outliers), red cross = outliers).

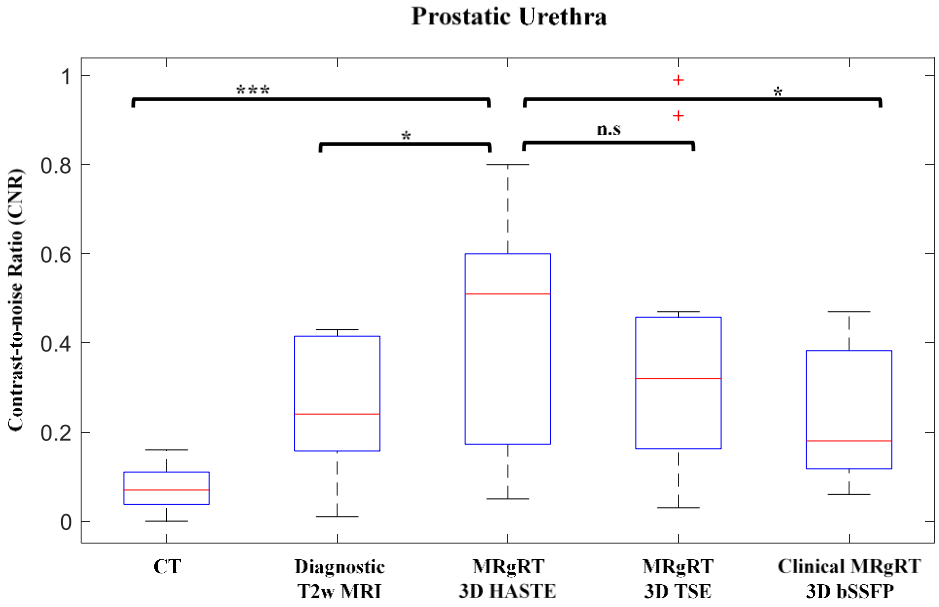

Figure 3-6. Boxplot of CT, diagnostic T2w MRI, MRgRT 3D HASTE, MRgRT 3D TSE, and clinical MRgRT 3D bSSFP prostatic urethra CNR. Urethral MRgRT scans showed significantly greater prostatic urethra contrast. (Red line = median value, top edge of box = 75th percentile, bottom edge of box = 25th percentile, whiskers = extreme data points (not outliers), red cross = outliers; n.s = not significantly different; ***** = significantly different—* = $p \leq 0.05$, *** = $p \leq 0.001$).

3.4 Discussion

This study evaluated five workflows with the intention of delineating the prostatic urethra utilizing three MRgRT workflows with different MR pulse sequences on a 0.35T MRgRT system and two conventional CT-based clinical workflows. The two new urethral T2w MR pulses sequences, MRgRT 3D HASTE and 3D TSE, acquired 1.5 mm isotropic resolution images in 7 to 8 min. Based on Observers 1 and 3, both urethral MRgRT sequences were markedly better than the current clinical MRgRT 3D bSSFP and CT for urethra visualization. Clinical 3D bSSFP has its intrinsic advantages of fast speed and high SNR, which can be used to

acquire 3D volumetric MRI within a very short time. Optimized MRgRT 3D HASTE and TSE showed less motion/ghosting artifacts, originating from subcutaneous fat and periprostatic fat, and better urethra/prostate contrast than clinical MRgRT 3D bSSFP. Thus, the urethral sequences' intended purpose should be to supplement current clinical MRgRT 3D bSSFP for urethral sparing. However, despite the potential improvement in GU toxicity reduction, the current urethral scan times are long, which can introduce unwarranted organ motion from bladder or rectum filling, potentially degrading the treatment efficacy. Future work will be focused on decreasing the urethral scan time by exploring acceleration strategies, further optimizing the protocol, and utilizing new vendor-improved receiver coils. Moreover, a limitation of the study was a lack of GU toxicity reports. Future work will look to incorporate MRgRT on-board urethral imaging into a urethra sparing study to evaluate its effectiveness in GU toxicity reduction.

No observer was able to visualize the urethra on CT as it provided no urethral contrast. Observer 1 and 3 reported little to no visibility on clinical MRgRT bSSFP, whereas, contrastingly, Observer 2 reported more visibility. Despite this, all observers reported similar high visibility scores for diagnostic MRI and MRgRT urethral scans. Overall, the MRgRT 3D HASTE performed best and was most comparable to diagnostic MRI. Although diagnostic MRI was acquired at higher field strength and is expected to have superior image quality, the low-field MRgRT urethral sequences. Specifically, our low-field MRgRT urethral sequences utilized heavier T2-weighting (larger TE), providing greater urethral contrast as seen in Figure 3-6.

Although MRgRT 3D HASTE and diagnostic MRI had similar prostatic urethra visibility, the prostatic urethra contours differed significantly. Contour differences may be due to the images being acquired on different days and the patient being in different positions.

Furthermore, no strict guidelines were followed to control patient bladder and rectum fullness for diagnostic MRI acquisition, and as a result, urethra location and shape may vary between a patient's diagnostic MRI and MRgRT 3D HASTE. MRgRT 3D TSE's prostatic urethra contour had the best agreement with MRgRT 3D HASTE's with the highest DICE score and smallest HD95 and MDA values. Both urethra MRgRT scans were acquired on the same day and in the same imaging session, however, there are still significant differences between these two contours, which may be due to different image contrast and potential motion during long acquisition. Furthermore, the prostatic urethra is a small structure, making the oncologist's contour extremely sensitive to any contour deviation. Compared to MRgRT 3D TSE, MRgRT 3D HASTE showed less grainy prostate glands, and subsequently easier visualization of urethras. This is also indicated by MRgRT 3D HASTE's higher CNR. Although MRgRT 3D HASTE's CNR was superior, its standard deviation was high, indicating inconsistent performance. CNR variance may be due to different prostate patients having varying residual amounts of urine in the prostatic urethra. Additionally, surrounding fat and ghosting artifacts decreases the CNR of the prostatic urethra. Furthermore, the prostatic urethra may be compressed due to nearby prostatic hyperplasia in the transitional zone (72). Regardless, the prostatic urethra's lining is histologically different from the surrounding prostate and should be distinguishable on MRI (73). Future work will focus on implementing fat suppression for more consistent contrast and improving scan technique for motion robustness.

The quantitative results in Figure 3-5 showed considerable disagreement of prostatic urethra position amongst CT and MR based workflows regardless of whether MRgRT imaging was done prior to or during treatment course. High urethra contouring accuracy and precision are critical for urethra sparing and radiation therapy efficacy as significant treatment degradation

could occur if reduced dose regions were not positioned correctly. One limitation of the study is a lack of a urethra ground-truth to reference. As a result, urethra accuracy could not be confidently reported. Currently, there is no gold-standard ground-truth for the urethra. However, our high MRgRT urethra visibility scores lead us to have higher confidence in the urethra contouring. Furthermore, MRgRT workflow avoids additional cross-modality image registration as the urethra can be reliably drawn on the planning MRI, at the time of simulation or before each treatment. With greater confidence, urethra sparing can be further improved with high visibility urethra on-board imaging for patient setup and pre-beam MRgRT on-line adaptive. Future work will be to design and construct anthropomorphic prostate phantom to study urethra contouring accuracy of our MRgRT urethra MRI sequences. Additionally, future work will be focused on detecting inter-observer and inter-fraction urethra localization variability for determining urethral margin.

One weakness of our study is the small patient cohort. Future work will add more patients to improve the power of the study. Another weakness was the qualitative scoring system, which was subjective. Future work should recruit additional radiation oncologists for more confident scoring and analysis.

3.5 Conclusion

Two 0.35T MRgRT T2w pulse sequences were proposed for urethra visualization and prostatic urethra contouring. MRgRT 3D HASTE provided high contrast and spatial resolution for prostatic urethra delineation. MRgRT workflow avoids cross-modality registration errors and holds the potential of accurate urethra delineation and effective urethra sparing during both initial MRgRT treatment planning and on-line adaptive radiation therapy.

Chapter 4.Urethral Inter-fractional Geometric and Dosimetric Variations of Prostate Cancer Patients: a study using an on-board MRI

A version of this chapter has been published Frontiers Oncology Journal: Pham J, Savjani RR, Yoon SM, et al. Urethral Interfractional Geometric and Dosimetric Variations of Prostate Cancer Patients: A Study Using an Onboard MRI. *Front Oncol*. 2022;12:916254. Published 2022 Jul 15. doi:10.3389/fonc.2022.916254

4.1 Introduction

Stereotactic body radiotherapy (SBRT) is now a widely accepted standard of care option for localized prostate cancer (74). Despite an overall highly favorable safety profile, SBRT late (13.3%) grade ≥ 2 genitourinary (GU) toxicity rates remain a significant challenge (7,57,75,76). Past efforts for reducing late GU toxicities have been focused on bladder sparing (77). However, urethral injury is also a significant contributor to GU toxicity (78,79). The urethra can be constrained below the prescription dose (urethra sparing) or above (hotspot limitation). Prospective SBRT trials have reported allowable urethra doses ranging between 34.7 Gy and 52.5 Gy in 5 fractions (80,81). Leeman et al. analyzed patients enrolled onto trials for SBRT and showed an increase to the maximum urethral dose metric (MUDM) correlated to an increase in acute (≤ 3 months) and late (> 3 months) grade ≥ 2 GU toxicity rates (79). While urethral sparing approaches are appealing from the standpoint of limiting toxicity, post-radiation patterns of failure studies have suggested that peri-urethral recurrences are common, and therefore hotspot limitation may be a better goal for minimizing toxicity while maintaining efficacy (82).

In addition to urethral dose constraints, urethra delineation uncertainty and intra-fraction/inter-fraction motion can also contribute to GU toxicity. Delineating the urethra on computed tomography (CT) images is non-trivial due to the lack of contrast between the urethra and prostate (83). Foley catheters have been used to delineate the urethra on planning CTs; however, the catheter can also displace and deform the urethra, resulting in urethra misposition (65,84). Alternatively, magnetic resonance images (MRI) can be acquired and registered to planning CTs for urethra delineation (85). Diagnostic 3T T2-weighted MRI has shown good urethra visualization and low inter-observer urethra contouring variation (86,87). However, contouring uncertainty from cross-modality registration adds uncertainties (88). Moreover, the shape and location of the urethra may change between diagnostic MRI and planning CT acquisitions, which are often acquired on different days with different patient positions. As for urethra intra-fraction/inter-fraction motion, little has been studied and its impact on urethral dose is unknown due to limited urethra visualization tools.

Recently, advancements in MR-guided radiation therapy (MRgRT) and the development of MR linear accelerators (MR-LINAC), equipped with on-board MRI, have allowed the application of MRI for prostate treatment planning, adaptation, and monitoring. MRI provides high soft-tissue contrast for accurate tumor and critical structure delineation (89). MR-LINAC's on-board MRIs allow for fiducial-free daily patient setup and inter-fraction MR-guided online adaptive radiation therapy (MRgART), where initial treatment plans can be re-calculated or re-optimized based on the patient's daily anatomy (90). Real-time cine MR can also be acquired during treatment delivery to monitor intra-fraction motion and gate treatment (32). Consistent and frequent radiation-free MR imaging, throughout patient treatment, enables use of smaller planning margins and improved critical structure sparing (76). Furthermore, the MRgRT

workflow minimizes cross-modality and cross-system registration errors as the MRIs are acquired on the same system with the patient in the treatment position.

Currently, it is standard practice to acquire a 3D balanced steady-state free precession (bSSFP) MRI for MRgRT treatment planning and daily patient setup using the ViewRay MRIdian MR-LINAC (ViewRay INC., Oakwood Village, OH, USA). Clinical bSSFP is intrinsically fast and has a high signal-to-noise ratio (SNR). However, it is T2/T1-weighted and provides lower urethral contrast than T2-weighted scans (91). As a result, at our institution, a T2-weighted MRI sequence is optimized and performed at the end of patient MR simulation for urethra delineation (91) and are acquired with a smaller FOV covering only the prostate gland. Due to time constraints, T2-weighted MRIs are not acquired for daily patient setup. Herein, we analyze interobserver variability as well as geometric and dosimetric changes in the urethra between the simulation scan and the final fraction of SBRT in a cohort of prospectively treated patients to determine the clinical significance of on-board urethra visualization for urethra-focused MRgART.

4.2 Method and Materials

This study was conducted according to the guidelines of the Declaration of Helsinki and approved by the Institutional Review Board of the University of California, Los Angeles, IRB #17-001064, on December 6, 2017. 26 prostate cancer patients undergoing MRgRT SBRT between June 2020 and June 2021 were prospectively included. Prior to patient simulation and each treatment fraction, patients were instructed to follow the institutional bladder filling and rectum emptying protocol. For CT simulation, patients were immobilized with a vacuum bag and a pelvic CT was acquired on a 16-slice CT scanner (Sensation Open, Siemens Medical Solutions, Erlangen, Germany). For MR simulation and before each treatment fraction, a clinical bSSFP

MRI was acquired on a 0.35T MR-LINAC system (ViewRay MRIdian, ViewRay Inc., Cleveland, OH, USA) using the same immobilization device. Additionally, a urethra-specific T2-weighted 3D half-Fourier acquisition single-shot turbo spin echo (3D HASTE) was acquired at simulation (HASTE 1) and at the end of the final treatment fraction (HASTE 2). Urethra imaging was only acquired at two timepoints due to clinical time constraints. 3D HASTE sequence parameters are as follow: repetition time (TR) = 1800 ms, echo time (TE) = 246 ms, voxel size 1.5 mm isotropic, FOV = 227 x 400 mm^2, number of slices = 40, number of averages = 6, acquisition time = 8:06 minutes. A more detailed explanation of 3D HASTE sequence optimization can be found in Pham et al (91).

The simulation clinical bSSFP MRI serves as the primary treatment planning image (planning MRI). An attending physician contoured the prostate gland as the clinical target volume (CTV) and all critical structures on the planning MRI in MIM Software (Cleveland, OH, USA). Due to high MRI prostate visualization and MRgRT daily/real-time image guidance, the planning target volume (PTV) was constructed by isotropically expanding the CTV by 2 mm. Two radiation oncologists (RO1 and RO2) independently contoured the prostatic urethras on both HASTE 1 and HASTE 2 for all patients. Prostatic urethra contours were cropped to be within the PTV. HASTE 1 and 2 were rigidly registered in MIM Software using box-based assisted alignment on the prostate. Afterwards, a medical physicist checked the registration and manual translational/rotational adjustments were made if necessary. Urethral inter-observer and inter-fractional geometric variation was evaluated using 95^{th} percentile Hausdorff distance (HD95), mean-distance-agreement (MDA), center-of-mass-shift (COMS), and DICE coefficient. A DICE coefficient score of > 0.70 reflected a good spatial and volumetric agreement between observers or no geometrical change between imaging fractions (87). Additionally, HASTE 1 and

2 bladder volumes were estimated and association between bladder volume change and urethral motion was assessed using regression analysis. Due to the HASTE images' limited FOV, complete bladder volume could not be measured, and as a result, a surrogate area index (Area = A × B) was used, in which the long axis (A) and perpendicular short axis (B) of the bladder in the central sagittal plane was measured.

Further, each RO qualitatively scored the urethra visibility of each image on a 4-point scale: 1 = no conspicuity; 2 = some conspicuity, the urethra can be identified, but not very clear; 3 = good conspicuity, the urethra can be identified clearly; 4 = excellent conspicuity. RO1 and RO2's urethra visibility scores were compared using Wilcoxon signed-rank test with a significance level of 0.05.

For dosimetric analysis, HASTE 1 and HASTE 2 were rigidly registered to their respective clinical bSSFP MRI. Both RO's urethra contours were transferred separately from HASTE images for treatment planning and dose estimation. For each RO, an MRgRT treatment plan was generated on the planning MRI using clinical contours and their respective HASTE 1 urethra contours. MRgRT plans were prescribed to deliver 40 Gy to 95% of PTV (5 fractions (Fx); 8 Gy/Fx). Each plan was optimized to meet clinical constraints (Table 4-1), including a urethral hotspot limiting constraint ($V42Gy \leq 0.03cc$).

Table 4-1. Clinical constraints for prostate patients

Constraint	
PTV V40Gy	≥ 95%
PTV V42Gy	< 30%
Rectum V20Gy	< 50%
Rectum V36Gy	< 10%
Rectum V40Gy	< 5%
Bowel V20Gy	< 30 cc
Urethra V42Gy	≤ 0.03 cc
Bladder V20Gy	< 40%
Bladder V39Gy	< 4 cc
Bladder V40Gy	< 10%

Urethral hotspot limitation constraint was prioritized over urethral sparing to maintain treatment efficacy and reduce risk of disease recurrence. The dose was calculated on the planning MRI with deformably registered electron density information from simulation CT using the MRgRT treatment planning system. The final fraction urethral dose was estimated by performing a forward calculation of the initial plan onto the final fraction patient setup bSSFP MRI. Urethral constraint, mean dose, D0.03cc, V42Gy, and PTV mean dose change between simulation and final fraction were evaluated. Simulation and final fraction dose parameters were compared using paired t-test with a significance level of 0.05.

4.3 Results

The average time between simulation and final fraction imaging was 21.4 ± 4.6 days. The RO1 and RO2's average qualitative urethra visibility scores were 1.8 ± 0.7 and 3.2 ± 0.7. RO2 scored urethra visibility significantly greater than RO1 ($p < 0.05$). The average HD95, MDA, COMS, and DICE between RO1 and RO2's urethra contours were 2.85 ± 1.34 mm, 1.02 ± 0.36 mm, 3.16 ± 1.61 mm and 0.58 ± 0.15.

Figures 4-(1-4) shows four prostate patients' (Patient A-D) HASTE 1 and 2 with RO1 and RO2 contours. Patient A-D showed ok-good inter-observer contour agreement (DICE >

0.60). Patients A and B showed minimal urethral inter-fraction change (DICE > 0.62), while Patients C and D showed significant urethral inter-fraction change (DICE < 0.54). The combined RO-average HD95, MDA, COMS, and DICE between simulation and final fraction urethra contours for all patients were 3.26 ± 1.54 mm, 1.29 ± 0.54 mm, 3.34 ± 2.01 mm. and 0.49 ± 0.18. No correlation between urethral motion and the bladder volume surrogate was observed (R2 < 0.1).

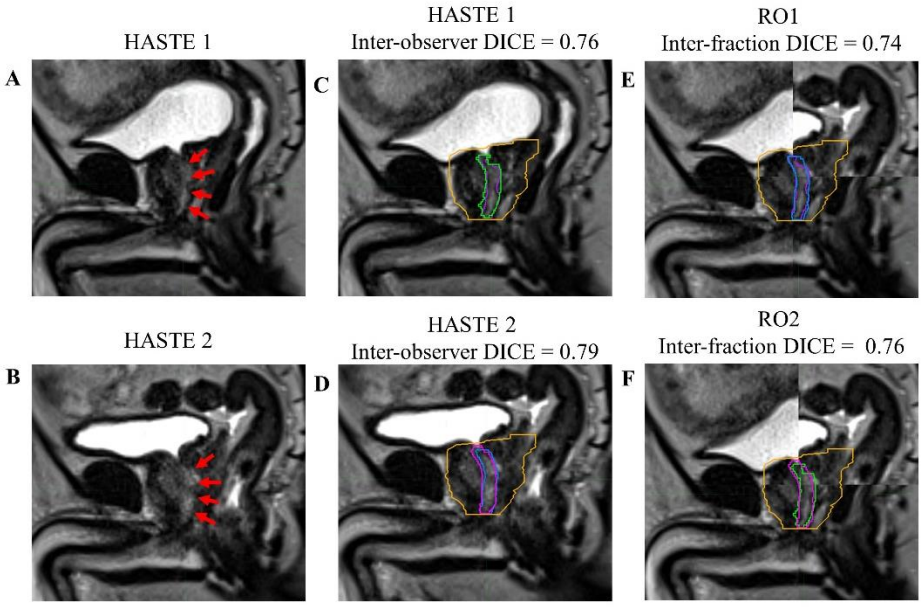

Figure 4-1. Patient A's (A) simulation (HASTE 1) and (B) final fraction (HASTE 2) urethra image (red arrows pointing to urethra). (C) Inter-observer urethra contour agreement between RO1 (purple) and RO2 (green) for HASTE 1. (D) Inter-observer urethra contour agreement between RO1 (blue) and RO2 (pink) for HASTE 2. Planning target volume (PTV) is contoured in orange. Inter-fraction urethra changes for (E) RO1 and (F) RO2 on fused (checkerboard layout) HASTE 1 and 2 images.

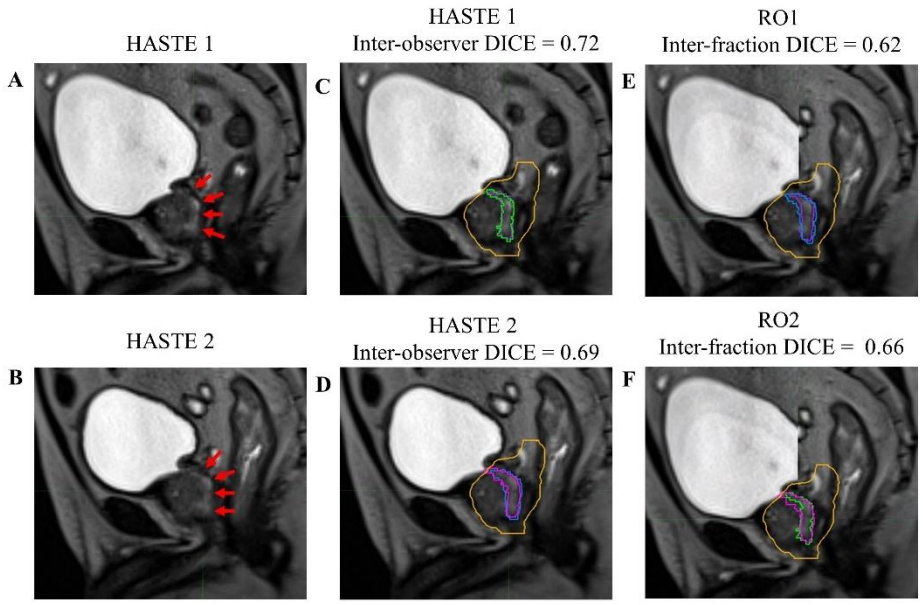

Figure 4-2. Patient B's (A) simulation (HASTE 1) and (B) final fraction (HASTE 2) urethra image (red arrows pointing to urethra). (C) Inter-observer urethra contour agreement between RO1 (purple) and RO2 (green) for HASTE 1. (D) Inter-observer urethra contour agreement between RO1 (blue) and RO2 (pink) for HASTE 2. Planning target volume (PTV) is contoured in orange. Inter-fraction urethra changes for (E) RO1 and (F) RO2 on fused (checkerboard layout) HASTE 1 and 2 images.

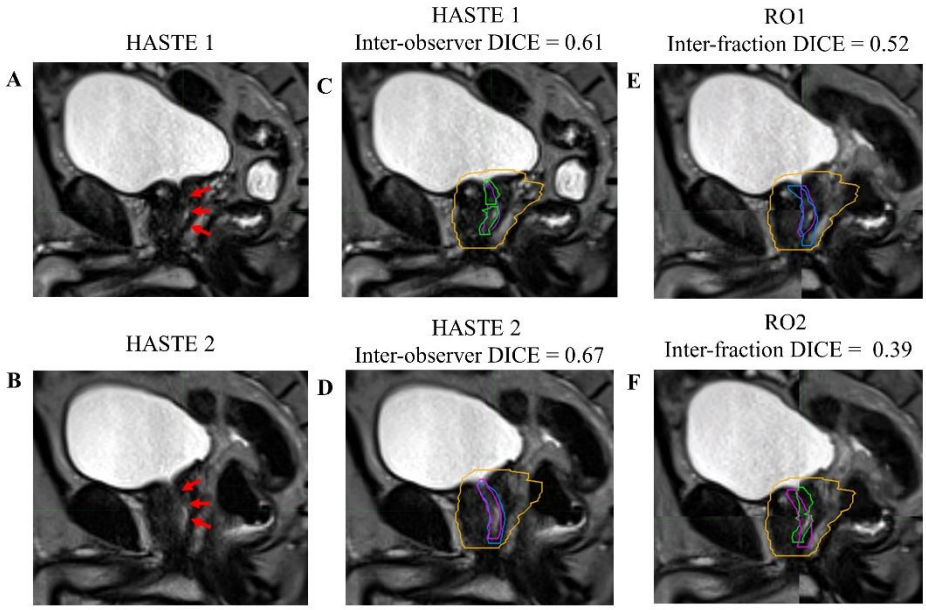

Figure 4-3. Patient C's (A) simulation (HASTE 1) and (B) final fraction (HASTE 2) urethra image (red arrows pointing to urethra). (C) Inter-observer urethra contour agreement between RO1 (purple) and RO2 (green) for HASTE 1. (D) Inter-observer urethra contour agreement between RO1 (blue) and RO2 (pink) for HASTE 2. Planning target volume (PTV) is contoured in orange. Inter-fraction urethra changes for (E) RO1 and (F) RO2 on fused (checkerboard layout) HASTE 1 and 2 images.

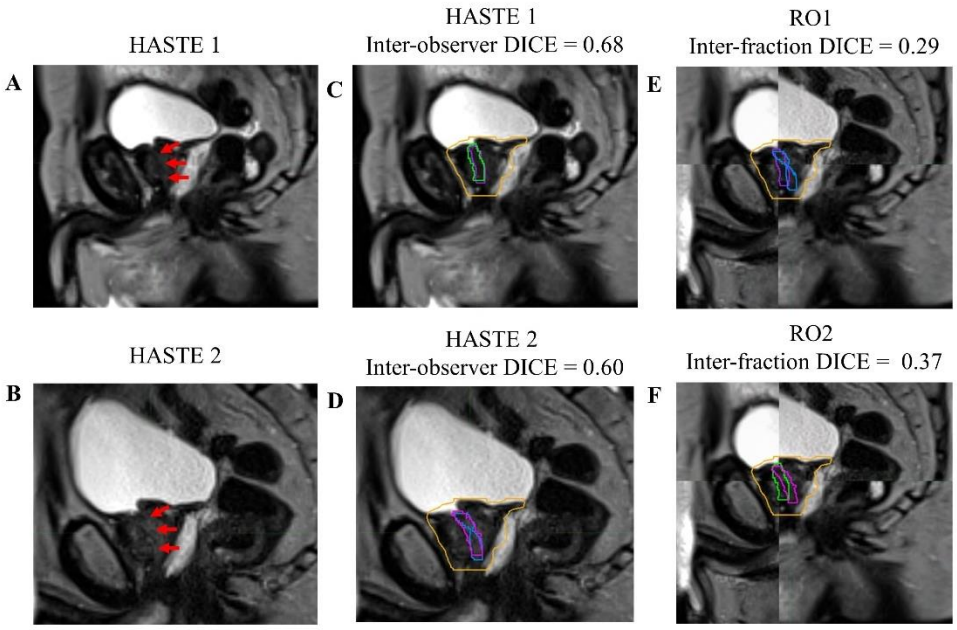

Figure 4-4. Patient D's (A) simulation (HASTE 1) and (B) final fraction (HASTE 2) urethra image (red arrows pointing to urethra). (C) Inter-observer urethra contour agreement between RO1 (purple) and RO2 (green) for HASTE 1. (D) Inter-observer urethra contour agreement between RO1 (blue) and RO2 (pink) for HASTE 2. Planning target volume (PTV) is contoured in orange. Inter-fraction urethra changes for (E) RO1 and (F) RO2 on fused (checkerboard layout) HASTE 1 and 2 images.

All patient simulation MRgRT plans met all clinical constraints, including urethra hotspot constraints. The combined RO-average simulation urethral mean dose, D0.03 cc, V42 Gy, and PTV mean dose were 40.69 ± 0.37 Gy, 41.83 ± 0.21 Gy, 0.02 ± 0.01 cc, and 41.29 ± 0.22 Gy. However, for RO1 and RO2, 23/26 (88%) and 21/26 (81%) patients' final fraction estimated urethral dose did not meet V42Gy ≤ 0.03cc. The combined RO-average final fraction urethral mean dose, D0.03 cc, V42 Gy, and PTV mean dose were 41.10 ± 0.68 Gy, 42.62 ± 0.72 Gy, 0.50 ± 0.58 cc, and 40.84 ± 0.65 Gy The final fraction urethral dose parameters were significantly greater than simulation ($p<0.05$), whereas the PTV dose parameters were significantly less ($p<0.05$). The combined RO-average urethral mean dose, D0.03 cc, V42Gy, and PTV mean dose

changes were 0.41 ± 0.60 Gy, 0.79 ± 0.74 Gy, 0.48 ± 0.58 cc, and -0.45 ± 0.71, respectively. Overall, dose parameters and urethral constraint change was consistent for both ROs.

Figures 4-5 and 4-6 shows both ROs' Patient A-D calculated (simulation) and estimated (final fraction) dose and urethra V42Gy. Patient A demonstrated minimal geometric urethral change and, as a result, little urethral dose change. Alternatively, Patient B showed minimal geometric urethral change, but significant urethral dose changes due to other anatomical changes such as differential bladder filling. Patient C exhibited significant geometric urethral change, resulting in the urethra moving into hot spot regions. Patient D showed significant geometric urethral change but little dose change, demonstrating the importance of hotspot location and robustness of each MRgRT IMRT plan.

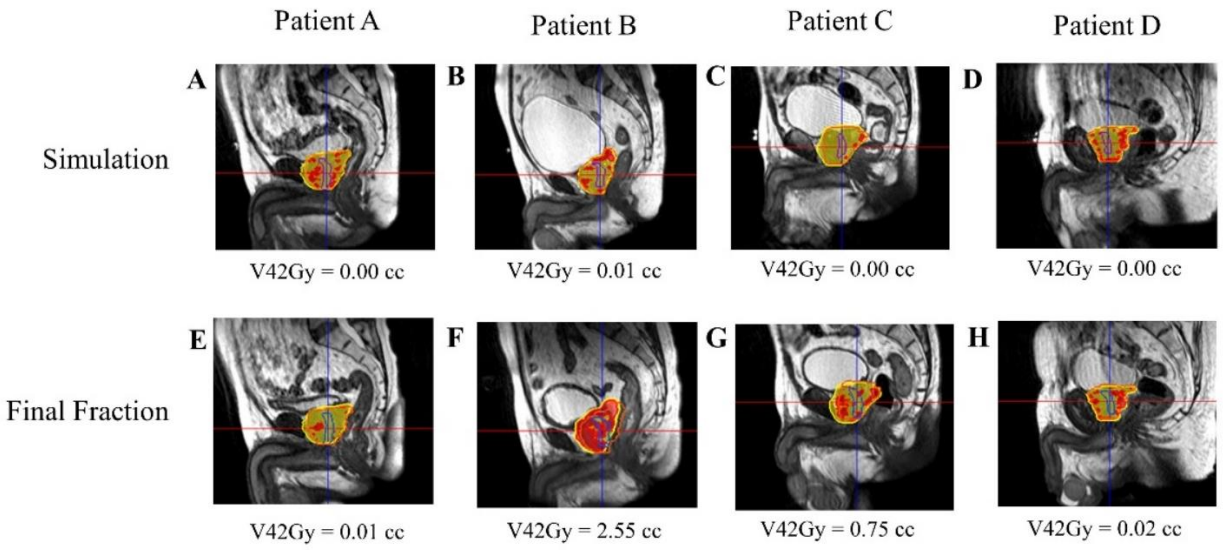

Figure 4-5. RO1's calculated and estimated dose and urethral V42Gy for Patient A-D's simulation and final fraction bSSFP. RO1 simulation/final HASTE urethra contour – purple/blue. Orange contour – PTV. Red – 105% (42 Gy) isodose region, Yellow – 95% (38 Gy) isodose region.

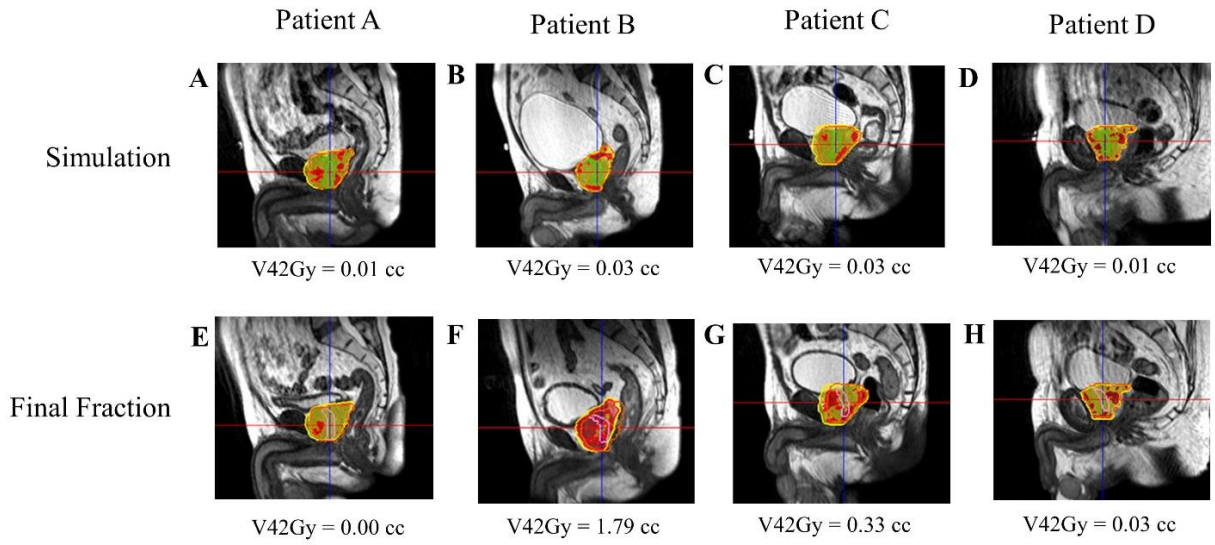

Figure 4-6. RO2's calculated and estimated dose and urethral V42Gy for Patient A-D's simulation and final fraction bSSFP. RO2 simulation/final HASTE urethra contour – green/pink. Orange contour – PTV. Red – 105% (42 Gy) isodose region, Yellow – 95% (38 Gy) isodose region.

4.4 Discussion

This study evaluated prostate cancer patients' inter-fractional urethral geometric and dosimetric change. Significant geometric and spatial urethral changes between simulation and the final fraction were noticed, indicating the potential need for daily urethral imaging to achieve better urethra protection by limiting urethral hotspots in MRgRT treatment planning and delivery. Our study reveals that the efficacy of urethral hotspot limiting constraints depends on inter-fractional urethral geometric and anatomic change as more than 80% of patients had a failing final fraction urethra V42Gy constraint. In other words, inter-fractional urethral geometric changes can result in a significant volume of the urethra moving into planned hot spot regions as shown in Figures 4-5F and 4-6F. Additionally, inter-fractional anatomical changes such as the bladder filling variation and prostate swelling can significantly alter the planned dose distribution and result in a higher urethral dose (92). Currently, there is no well-established dosimetric

constraint for the urethra. Prostate cancer patients were prescribed a 5 Fx x 8 Gy SBRT schedule to the PTV, which is a higher dose than the more common, lower dose 5 Fx x 7.25 Gy schedule. In principle, lower prescription dose may have a lower likelihood of GU toxicity, however, urethral hotspots remain a concern for the 5 Fx x 7.25 Gy schedule as the CTV, containing the urethra, is still prescribed to receive 40 Gy (7). MRgART workflow with on-board urethral imaging may be valuable to account for the daily urethral change as shown in this study, and if necessary, treatment re-optimization may be utilized to re-plan and reduce daily urethral hotspots and, as a result, GU toxicity.

This study had several limitations. First, there is a lack of urethra ground truth to reference, and as a result, inter-fractional urethral geometric and dosimetric changes are reported as relative changes. Currently, there is no gold-standard ground-truth for urethra localization at the time of treatment. Nonetheless, the much-improved soft tissue contrast with the urethral specific MRI makes us more confident in urethra localization. Second, urethra visibility with our current MRI sequence varied considerably between patients and between observers. Inter-patient urethral visibility variance may be due to varying amounts of residual urine in the prostatic urethra, surrounding fat and motion/ghosting artifacts, as well as nearby prostatic hyperplasia compressing the prostatic urethra (86). Inter-observer urethral visibility variance can also be due to different levels of observer experience. Further MRI sequence and imaging protocol optimization is necessary to achieve more robust urethral visualization. Third, the reported urethral MRI sequence took 7-8 minutes, which may be impractical for the already time-intensive MRgART workflow. The long urethral scan time can increase the chance of unwanted patient motion and anatomical changes. Therefore, future work will explore MR sequence acceleration strategies. Lastly, due to long urethral imaging times and clinical time constraints,

urethra images were only acquired at simulation and at the final fraction, which limits the accuracy of the reported urethral inter-fractional geometric and dosimetric changes variations. Despite this, a total of 26 prostate cancer patients were recruited, and the reported results of the entire cohort can be used to estimate urethral inter-fractional variations.

4.5 Conclusion

Inter-fractional urethral geometric or anatomical change can result in clinically significant urethral dose change for prostate cancer patients treated with urethral hotspot limiting MRgRT plans, potentially contributing to an increased urethral dose. MRgART workflow with on-board urethral imaging may be used to reduce daily urethral hotspots and, as a result, GU toxicity.

Chapter 5. Dosimetric Predictors for Acute Genitourinary Toxicity in MR-guided Stereotactic Body Radiation Therapy (SBRT): Expanded Substructure with Fraction-wise Analysis

5.1 Introduction

Stereotactic body radiation therapy (SBRT) has been leveraged to deliver large and highly conformal fractionated radiation (dose per fraction ≥ 5 Gy) for curative prostate cancer treatments (93). Overall, SBRT has been shown to have similarly high biochemical control rates when compared to conventional treatment fractionation while also benefitting from significantly reduced treatment times (94). Although SBRT improves treatment efficiency, genitourinary (GU) toxicity remains a significant challenge for patients. Based on published PACE-B and multi-center SBRT clinical trials, acute and late grade ≥ 2 GU toxicity rates after SBRT are estimated to be 29.1% and 12.0% (9,95,96) As a result, SBRT-specific dosimetric predictors should be identified to reduce the risk of treatment-related GU toxicity.

Most dosimetric parameters for minimizing GU toxicity focus on whole bladder dosimetry. However, the trigone and urethra receive high doses, similar to that of the planning target volume (PTV), due to their proximity to the target, whereas the superior portion of the bladder is largely spared (97,98). It also has been shown the bladder wall exposure may be more predictive of GU toxicity than whole bladder dosimetry (99). Therefore, dosimetric parameters for urinary substructures may better characterize exposure and be more predictive of GU toxicity than the entire bladder volume. While there is a strong rationale to track and limit dose to these sensitive substructures, critical substructure sparing is difficult on CT-guided treatment delivery systems due to limited soft-tissue contrast.

In a recently published phase III randomized clinical trial (MIRAGE), MRI-guided SBRT was shown to significantly reduce acute grade ≥ 2 GU toxicity compared to CT-guided SBRT (MRI arm: 24.4%; CT arm: 43.4%). This benefit was attributed to the fact that MRgRT enabled PTV margins to be reduced from 4 mm to 2 mm, allowing for improved critical structure sparing and treatment toxicity reduction. Because all patients on the trial had on-board 0.35T MRI images acquired prior to treatment and at simulation, the high soft-tissue contrast imaging data from the trial provide an unprecedented ability to track doses delivered to the trigone and bladder wall not only on the planning simulation, but also on daily anatomical changes.

Most existing dose-based toxicity predictors rely on a few pre-selected DVH points and statistics (e.g., mean, minimum, and maximum) from the planning dose distribution. Planning dose distributions may differ significantly from the delivered dose due to inter-fraction anatomic variations, and thus may be imprecise for dose-toxicity modeling (100). In this study, we sought to identify dosimetric predictors of acute GU toxicity following MRI-guided SBRT by utilizing on-board images to track planning and daily dose of bladder and substructures (trigone, bladder wall, and urethra). Furthermore, granular DVH points were analyzed as opposed to pre-selected coarse clinical dose endpoints, with the goal of providing more comprehensive information to predict treatment toxicity. A clinical toxicity regression model using only clinical parameters was also evaluated. Dosimetric toxicity regression models were compared to the clinical regression model and a hybrid model, combining the best performing dosimetric predictors with the clinical parameters.

5.2 Method and Materials

5.2.1 Patient Cohort

Sixty-nine prostate cancer patients, in the MIRAGE clinical trial (NCT04384770), treated with SBRT using a 0.35T MR-LINAC MRgRT system (ViewRay MRIdian, ViewRay Inc., Cleaveland, OH, USA) were included. Nine patients were excluded from the original 78 patients included in the MRI arm of the MIRAGE trial due to image acquisition and exporting issues from the treatment planning and delivery system, preventing substructure contouring. During patient simulation, a CT scan (electron density information), a 0.35T true fast imaging with steady state precession MRI (TrueFISP, planning MRI), and a 0.35T half-Fourier acquisition single-shot turbo spin echo MRI (HASTE, urethra imaging) were acquired. HASTE imaging provided improved urethral delineation and was used for urethral delineation as described in Pham *et al.* (101) The clinical target volume (CTV) was defined as the prostate and proximal seminal vesicle on the planning MRI. Afterwards, the PTV was formed by isotropically expanding the CTV by 2 mm. MRgRT SBRT plans were prescribed to deliver 40 Gy to 95% of the PTV (5 fractions [Fx]; 8 Gy/Fx) and optimized to meet clinical constraints (Table 5-1, complete clinical dose constraints and trial protocol can be found in Kishan *et al*. (102)).

Table 5-1. MRgRT SBRT clinical constraints for prostate cancer patients

Constraint		**Constraint**	
PTV V40 Gy	$\geq 95\%$	Rectum V20 Gy	$\leq 50\%$
PTV V42 Gy	$\leq 30\%$	Rectum V32 Gy	$\leq 20\%$
Urethra V42 Gy	≤ 0.03 cc	Rectum V36 Gy	≤ 10 %
Bladder V20 Gy	$\leq 40\%$	Rectum V38 Gy	< 2 cc
Bladder V39 Gy	< 2 cc	Rectum V40 Gy	$\leq 5\%$
Bladder V40 Gy	$\leq 5\%$	Rectum V42 Gy	< 0.03 cc
Bladder V42 Gy	< 0.03 cc		

Elective nodal radiotherapy (25 Gy in 5 fractions), a simultaneous integrated boost to the gross tumor volume (GTV) (42 Gy in 5 fractions), simultaneous integrated boost (35 Gy in 5 fractions) to the pelvic node, and androgen-deprivation therapy (ADT) usage was allowed per physician discretion. Prior to each treatment fraction delivery, a TrueFISP was acquired and the daily prostate was aligned to the planning MRI prostate for treatment. During treatment, cine MRIs were acquired at 4 frames per second in the sagittal plane and an automatic beam hold was initiated if >10% of the prostate cross-sectional area moved outside a 3 mm gating margin around the prostate.

Acute GU toxicity was evaluated using physician-scored Common Terminology Criteria for Adverse Events, version 4.03 (CTCAE v4.03) scale, from start of SBRT up to 90 days after SBRT (103). Grade 2 GU toxicity or greater was considered as significantly compromising to patient quality of life after treatment. Overall, 17/69 (24.6%) of patients reported acute grade 2 GU toxicity. No GU toxicity greater than grade 2 was reported.

5.2.2 Dosimetric Feature Selection

For retrospective dose analysis, daily TrueFISP scans were rigidly (only translation) registered to the planning MRI using the alignment from daily treatment setup. The trigone, bladder, bladder wall, rectum, and rectal wall were contoured on the simulation and five daily pre-treatment MRIs for each patient. Bladder and rectal walls were delineated by generating a 3 mm inner ring from the bladder and rectum contours, respectively. Daily dose to each structure was estimated by transferring the planning dose distributions to the daily MRI based on the daily setup alignment (Figure 5-1). Absolute and relative cumulative DVHs were granularly (0 to 51 Gy, 0.1 Gy increments) extracted for each structure from the simulation and daily treatment

scans to provide comprehensive dosimetric metrics for evaluation. Additionally, structure volume, mean dose, minimum dose, and maximum dose were recorded.

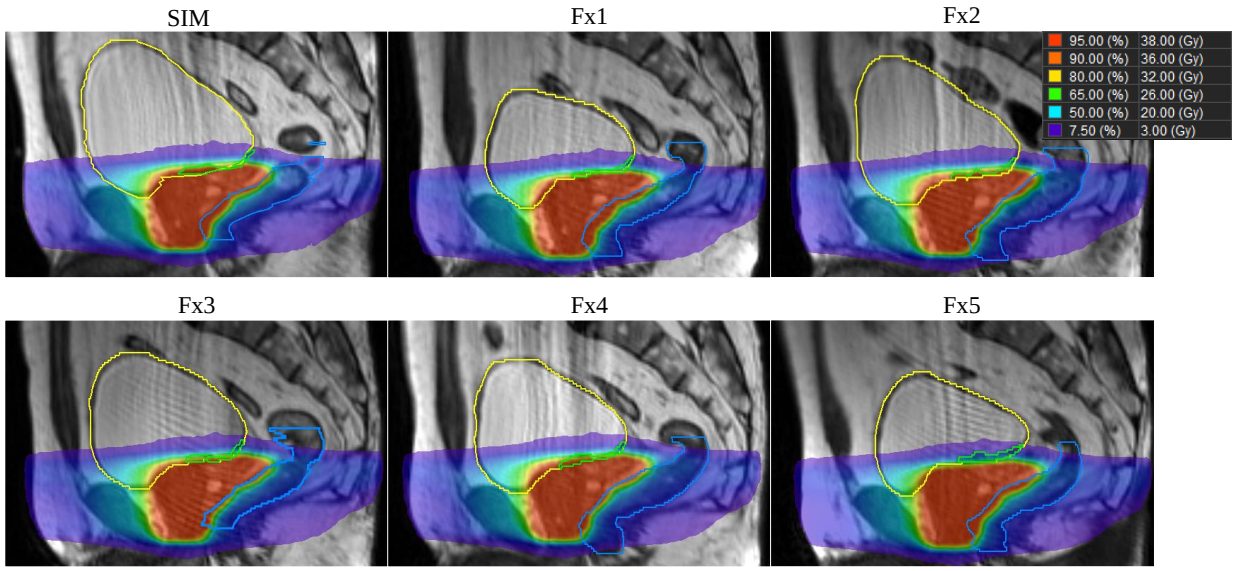

Figure 5-1. Simulation/Planning MRI (SIM) and pre-treatment (Fx 1-5) daily MRI for a prostate patient. Planning dose distribution/isodose is overplayed on each MRI. Simulation and daily trigones, bladder, and rectum are contoured in green, yellow, and blue, respectively.

Patients were randomly partitioned into a training (55 patients) and testing set (14) with similar grade 2 GU toxicity rates (14/55 = 25.5%; 3/14 = 21.4%) in each set. Simulation and daily structure parameters were incorporated as candidate features for dosimetric predictors to infer grade 2 GU toxicity. All features were normalized to have a mean of 0 and standard deviation of 1. Features with no variance among patients were removed. Additionally, features were pre-filtered using t-test ($p < 0.05$) followed by a maximum relevance minimum redundancy (mRMR) algorithm to reduce highly correlated and redundant features.

Logistic regression with three different feature selection schemes were investigated, specifically: a benchmark flat selection scheme with least absolute shrinkage and selection (LASSO), and two time group selection approaches, time-group LASSO and interactive grouped

greedy algorithm (IGA) (104–107). Ideally, a sparse logistic regression should follow the following optimization scheme for *m* patients:

$$\min_{x} \sum_{i=1}^{m} \log\left(1 + e^{-y_i(x^T a_i + c)}\right) \quad s.t.. \ \#\ of\ significant\ components\ or\ group\ (x) < K \quad (5\text{-}1)$$

where y_i represents the response ($y_i = 1$ for GU grade ≥ 2; $y_i = -1$ GU grade < 2), $\boldsymbol{a_i}$ represents the i-th feature of the feature matrix, $A \in \mathbb{R}^{m \times n}$, **x** is the feature weight vector, and c is the scalar intercept. However, direct regularization of counting nontrivial components or groups corresponds to L0 regularization which is highly nonconvex, where the solution can be computationally expensive and subject to local optimums. To this end, relaxed forms, such as L1 regularization was used as a surrogate for the ideal L0 regularization for feature selection. L1 (or LASSO) regularization adds a penalty term proportional to the absolute value of the feature weights, thus feature weights can be driven down to exactly zero, promoting sparsity and feature reduction. L1 regularization is a convex optimization problem, thus standard convex optimization methods (gradient descent) can be efficiently used to achieve feature selection.

5.2.3 Flat Single Layer Feature Selection

LASSO logistic regression selects features by optimizing the following objective function for *m* patients:

$$\min_{x} \sum_{i=1}^{m} \log\left(1 + e^{-y_i(x^T a_i + c)}\right) + \lambda \|\boldsymbol{x}\|_1 \quad (5\text{-}2)$$

where λ is ℓ_1-norm regularization parameter. The first term of the objective function is the cost function of the logistic regression, which is defined as the negative log-likelihood function. The second term is the L1 regularization. Larger λ values result in stronger regularization (higher

sparsity/feature reduction) and vice versa. λ was selected based on five-fold cross validation on the training cohort. A range of a 1000 log-spaced λ values between 0.0001 and 100 was selected.

During five-fold cross validation regularization tuning, the training cohort was divided into five equal-sized groups. In each group, at least one patient had a GU grade ≥ 2. For each fold, a group was selected as the validation set and the remaining four groups given a regularization value, were used to train the feature selection model. The model's deviance was evaluated on the validation set, and this was repeated four more times, selecting a new unique group to be the validation set each time. For each regularization value, the average and standard deviation of the deviance from cross-validation was calculated, and the regularization with minimum deviance and low variance selected as the optimal value for feature selection on the entire training set.

5.2.4 Time-grouped Feature Selection

For groups LASSO and IGA, features identified across the simulation/planning and five treatments (fractions 1-5) were grouped to encourage consistency and stability. Therefore, filtered features with incomplete groups, due to pre-filtering, had missing timepoint features recovered. Additionally, CTV, PTV, and urethra features had their features for fractions 1-5 padded with values from simulation, as these structures were only contoured for the simulation anatomy due to time constraints and the urethra imaging (HASTE) only being acquired during simulation. Time-group LASSO logistic regression selects group features by optimizing the following objective function for *m* patients:

$$\min_{x} \sum_{i=1}^{m} \log\left(1 + e^{-y_i(\boldsymbol{x}^T \boldsymbol{a}_i + c)}\right) + \alpha \sum_{i=1}^{k} \left\|\boldsymbol{x}_{G_i}\right\|_2 \quad (5\text{-}3).$$

Similar to LASSO, time-group LASSO also encouraged feature selection but regularized with L2,1 in contrast to flat L1 regularization so that the sparsity-encouraging L1 structure was imposed on the group level G and a smoothing-encouraging L2 structure was imposed within the group. L2 (or Ridge) regularization added a penalty term proportional to the square of the feature weights, which smoothed weights and prevented model overfitting. Here, α was the $\ell_{2,1}$-norm regularization parameter and promoted sparsity among grouped features, while allowing features within groups to be kept. The feature weight vector, **x**, was divided into k non-overlapping groups $\boldsymbol{x}_{G_1}, \boldsymbol{x}_{G_2}, \ldots, \boldsymbol{x}_{G_k}$. α was tuned using five-fold cross validation and a range of 1000 log-spaced values between 0.01 and 1 was selected.

IGA utilized a forward-backward greedy approach to achieve feature selection.

Candidate groups, G, were identified to drive down the criterion function:

$$Q = \log\left(1 + e^{-y_i(\boldsymbol{x}^T \boldsymbol{a}_i + c)}\right) + \frac{\rho}{2}\|\boldsymbol{x}_G\|_2^2 \quad (5\text{-}4).$$

IGA applied L2 regularization on the candidate group, where ρ was the ridge factor. Initially, the criterion function was evaluated with no groups. At each iteration, *k*, a forward group selection was performed followed by a backward group elimination step. During the forward step, the criterion function was evaluated for each group and the group that reduced the criterion function the most was selected. At the end of the forward step, the criterion function gain, $\delta(k)$ was calculated. Afterwards, the backward step was implemented to eliminate redundant groups. During the backward step, the difference between the criterion function of the current groups and the function with one group removed was evaluated. If the smallest difference was less than the threshold $\frac{\delta(k)}{2}$, the least significant group was removed. The elimination step was repeated until the smallest difference was no longer less than the threshold, leaving only significant groups.

The regularization parameter ρ and the number of iterations was tuned using five-fold cross-validation and a range of 1000 log-spaced values between 0.01 and 10 and a maximum iteration of 20.

For time-group LASSO and IGA, an additional feature post-filtering was applied to remove the remaining highly correlated groups amongst each organ/structure. For a selected organ/structure, unique combinations of group features were used to train a logistic regression model and the validation set was evaluated with the following cost function:

$$\sum_{i=1}^{m} \log\left(1 + e^{-y_i(x^T a_i + c)}\right) + \sigma \left\| x_{G_O} \right\|_0 \quad (5\text{-}5)$$

$\left\| x_{G_O} \right\|_0$ was the L0 norm and counted the number of groups for the selected organ, and σ represented the respective tuned regularization parameter for time-group LASSO (α) and IGA (ρ). The group combination with the lowest five-fold cross-validated average cost function value was selected for the respective organ. Post-filtering was applied for each organ, starting with the organ with the most amount of group features to the least.

5.2.5 Toxicity Regression Models

Grade 2 GU toxicity prediction was evaluated on the validation set (cross-validation on training set) and testing set. A dosimetric logistic regression model was trained on either the training folds (cross-validation evaluation) or the entire training set (testing set evaluation) using the selected features from either LASSO, time-group LASSO, or IGA. Performance was evaluated using receiver operating (ROC) area under the curve (AUC), accuracy, sensitivity, and specificity determined by the optimal operating point of the training. Dosimetric model validation performances were compared using a one-way ANOVA test ($p<0.05$). Additionally, a

clinical logistic regression model was trained and evaluated using only clinical parameters (age, baseline International Prostate Symptom (IPSS) score, prostate volume ADT usage, nodal treatment, GTV boost, and spaceoar hydrogel). A hybrid logistic regression model was then trained and evaluated, combining dosimetric predictors from the best testing performing dosimetric model and clinical parameters. The best performing dosimetric model, clinical model, and hybrid model were compared using a one-way ANOVA test ($p<0.05$). Finally, the feature importance of the best performing toxicity regression model was evaluated based on its logistic regression weight.

5.3 Results

Table 5-2 shows the dosimetric feature selection results by LASSO, time-group LASSO (without and with L0 post-filtering), and IGA (without and with L0 post-filtering). LASSO selected 12 features, time-group LASSO selected 8 groups, and IGA selected 15 groups. L0 post-filtering removed neighboring bladder and rectal wall DVH features, resulting in 7 and 12 groups being selecting for time-group LASSO and IGA, respectively. All features were selected from each structure, except the PTV.

Table 5-3 shows the validation and testing GU toxicity regression performance for LASSO, time-group LASSO (without and with L0 post-filtering), and IGA (without and with L0 post-filtering). Validation performances were not significantly different among LASSO, time-group LASSO (without and with L0 post-filtering), and IGA (without and with L0 post-filtering). L0 post-filtering improved the testing performance of IGA, resulting in the best testing performance with accuracy, sensitivity, and specificity of 0.79, 0.67, and 0.82, respectively.

Table 5-2. Dosimetric features selected by LASSO, group LASSO (without and with L0-post filtering), and IGA (without and with L0-post filtering). Group LASSO and IGA selected groups features. Each group contains 6 features for each timepoint. (simulation + Fx 1-5). Absolute (ml) and relative (%) DVH values were evaluated.

	LASSO	**Time-group LASSO**		**IGA**	
Post-Filtering	None	None	L0	None	L0
CTV	41.9 Gy CTV SIM (%)	41.9 Gy CTV (%)	41.9 Gy CTV (%)	41.9 Gy CTV (%)	41.9 Gy CTV (%)
	19.7 Gy Bladder Wall Fx1 (ml)	19.7 Gy Bladder Wall (ml)		19.7 Gy Bladder Wall (ml)	19.7 Gy Bladder Wall (ml)
Bladder Wall	19.8 Gy Bladder Wall Fx1 (%)	19.8 Gy Bladder Wall (%)	19.8 Gy Bladder Wall (%)	19.8 Gy Bladder Wall (%)	
				19.9 Gy Bladder Wall (%)	
	19.8 Gy Bladder Fx3 (ml)	19.8 Gy Bladder (ml)	19.8 Gy Bladder (ml)	19.8 Gy Bladder (ml)	19.8Gy Bladder (ml)
Bladder				20.5 Gy Bladder (ml)	20.5 Gy Bladder (ml)
		15.9 Gy Trigone (ml)	15.9 Gy Trigone (ml)	15.9 Gy Trigone (ml)	15.9 Gy Trigone (ml)
				18.2 Gy Trigone (ml)	18.2 Gy Trigone (ml)
	19.3 Gy Trigone Fx3 (ml)				
Trigone	41.2 Gy Trigone Fx1 (ml)				
	43.2 Gy Trigone Fx4 (ml)				
				43.3 Gy Trigone (ml)	43.3 Gy Trigone (ml)
	41.4 Gy Urethra SIM (%)	41.4 Gy Urethra (%)	41.4 Gy Urethra (%)	41.4 Gy Urethra (%)	41.4 Gy Urethra (%)
Urethra		41.7 Gy Urethra (%)	41.7 Gy Urethra (%)	41.7 Gy Urethra (%)	41.7 Gy Urethra (%)
	1.2 Gy Rectal Wall SIM (%)			1.2 Gy Rectal Wall (%)	1.2 Gy Rectal Wall (%)
Rectal Wall	1.2 Gy Rectal Wall Fx1 (%)				
	44 Gy Rectal Wall Fx2 (%)			44 Gy Rectal Wall (%)	
				44.1 Gy Rectal Wall (%)	44.1 Gy Rectal Wall (%)
Rectum		8.5 Gy Rectum (%)	8.5 Gy Rectum (%)	8.5 Gy Rectum (%)	8.5 Gy Rectum (%)
	8.9 Gy Rectum Fx4 (%)				

A hybrid model, combining IGA (with L0 post-filtering) dosimetric predictors and clinical parameters, was trained. Table 4 shows the validation and testing GU toxicity regression performance for IGA (with L0 post-filtering), clinical model with only clinical parameters, and

hybrid model. Post-hoc analysis of the one-way ANOVA indicated the clinical and hybrid had significantly different validation AUC, accuracy, and specificity, whereas IGA (with L0 post-filtering) did not have significantly different validation performance. Moreover, IGA (with L0 post-filtering) had the same testing performance as the hybrid model, which was higher than the clinical model.

Table 5-3. Validation and testing grade 2 GU toxicity regression performance using LASSO, time-group LASSO (without and with L0-post filtering), and IGA (without and with L0-post filtering (p-value determined by one-way ANOVA).

	LASSO	**Time-Group LASSO**		**IGA**		**p-value**
Post-Filtering	None	None	L0	None	L0	
Validation AUC (95% CI)	0.84 (0.63-1.05)	0.66 (0.51-0.80)	0.62 (0.43-0.81)	0.64 (0.45-0.83)	0.57 (0.52-0.61)	0.185
Validation Accuracy (95% CI)	0.87 (0.70-1.05)	0.71 (0.62-0.80)	0.67 (0.46-0.88)	0.60 (0.42-0.78)	0.69 (0.62-0.79)	0.210
Validation Sensitivity (95% CI)	0.80 (0.54-1.06)	0.53 (0.14-0.93)	0.63 (0.27-1.00)	0.60 (0.36-0.84)	0.37 (0.30-0.43)	0.367
Validation Specificity (95% CI)	0.90 (0.76-1.04)	0.79 (0.64-0.93)	0.68 (0.34-1.01)	0.61 (0.42-0.79)	0.80 (0.74-0.87)	0.299
Testing Accuracy	0.71	0.50	0.43	0.36	0.79	
Testing Sensitivity	0.33	0.00	0.00	0.33	0.67	
Testing Specificity	0.82	0.64	0.55	0.33	0.82	

Table 5-4. Validation and testing grade 2 GU toxicity regression performance for IGA (with L0 post-filtering), clinical model with only clinical parameters, and hybrid model (combing IGA and clinical parameters). (p-value determined by one-way ANOVA).

	IGA (with L0 post-filtering)	**Clinical**	**Hybrid**	**p-value**
Validation AUC (95% CI)	0.57 (0.52-0.61)	0.72 (0.63-0.82)	0.48 (0.36-0.62)	0.02
Validation Accuracy (95% CI)	0.69 (0.62-0.79)	0.82 (0.76-0.87)	0.54 (0.37-0.72)	0.02
Validation Sensitivity (95% CI)	0.37 (0.30-0.43)	0.53 (0.14-0.93)	0.36 (0.15-0.58)	0.61
Validation Specificity (95% CI)	0.80 (0.74-0.87)	0.90 (0.81-0.99)	0.61 (0.41-0.81)	0.03
Testing Accuracy	0.79	0.64	0.79	
Testing Sensitivity	0.67	0.33	0.67	
Testing Specificity	0.82	0.73	0.82	

Figure 5-2 shows the relative feature importance identified by IGA (with L0-post filtering). Bladder V19.8 Gy and V20.5 Gy was shown to be the most important dosimetric

predictor for grade 2 GU toxicity followed by trigone V15.9 Gy and 18.2 Gy. Simulation-only structures such as the urethra and CTV showed the lowest importance.

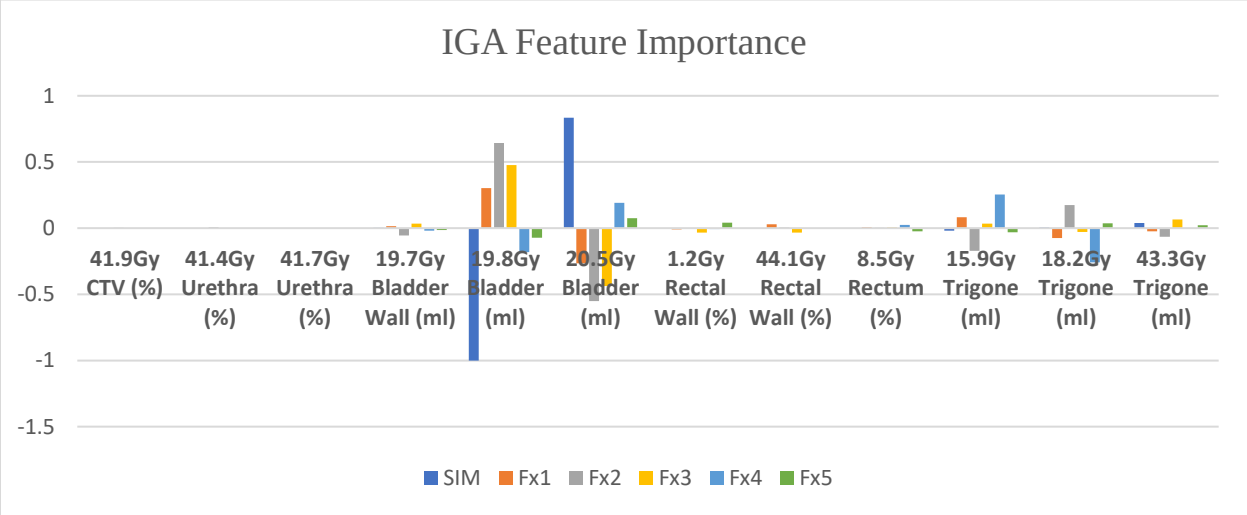

Figure 5-2. Relative feature importance (determined by logistic regression weight) identified by IGA with L0-post filtering.

5.4 Discussion

In this study, we sought to identify dosimetric predictors for predicting grade ≥ 2 GU toxicity in a cohort of prostate cancer patients treated with MRgRT SBRT. Dosimetric predictors were expanded beyond the bladder to include the CTV, PTV, trigone, bladder wall, urethra, rectum, and rectal wall. Additionally, in contrast to static planning-based predictions using pre-selected clinical dose endpoints, a per-fraction framework was used to account for granular DVH points at different timepoints throughout SBRT. Fractional and granular DVH generated a larger feature space to be analyzed (>20,000 initial features). Three feature selection approaches (LASSO, time-group LASSO, and IGA) were used to reduce features that were then evaluated with the aim of identifying new dosimetric constraints for mitigating GU toxicity in prostate cancer patients treated with MRgRT SBRT.

Single layer LASSO selected fewer features than time-group LASSO and IGA as it identified features at specific time points making it less susceptible to overfitting. Despite LASSO's high validation performance, the 95% confidence interval was large indicating the training cohort was limited and highly variable. Furthermore, the selected features were not consistent across multiple timepoints, resulting in low interpretability and casting doubt into consistency and generalizability. In contrast, with an effort to explicitly encourage feature consistency/stability and interpretability, time-group LASSO and IGA selected 8 and 15 groups, respectively. After L0 post-filtering, time-group LASSO and IGA selected 7 and 12 features, corresponding to 42 and 72 total features. Both group-based feature selection methods identified more features than LASSO, as they operate as take it or leave it on the group level. In principle, incorporating more features may risk overfitting, as illustrated by time-group LASSO's poor testing performance.

LASSO and time-group LASSO are shrinkage-based approaches and have inherently large estimation bias and relatively restrictive conditions on feature selection consistency, resulting in less relevant features being selected over more informative ones (108). Additionally, L1 regularization was used as a surrogate for L0 regularization to promote sparsity and achieve feature selection at a significantly lower computational cost. The performance of L1 regularization as a surrogate for L0 regularization may be suboptimal when restrictive isometry property (RIP) condition is not satisfied. This study evaluated granular DVH metrics, which included highly correlated DVH points from neighboring dose increments, potentially resulting in the feature space not adequately satisfying the RIP condition. Although, L1 regularization can promote sparsity, the model generated was not generalizable and resulted in unacceptable testing performance. L1 regularization does not penalize the selection of additional features, and as a

result, correlated and redundant features may be selected. This results the feature weight being divided among the correlated features as opposed to selecting and weighing a single feature from the correlated group. To mitigate this effect, a L0 post-filtering step was added after time-group LASSO to remove correlated features. Post-processing was preferred as it is less computationally expensive to evaluate the L0 regularization on the post-processed reduced feature space than if it were to be implemented on the larger feature space just after pre-filtering. However, L0 post-filtering did not significantly improve the performance of time-group LASSO as bulk feature reduction was already completed based on the L2,1 regularization. Future studies will explore implementing a cost for adding additional features in the shrinkage approaches as this is expected to improve feature identification and algorithm performance.

Alternatively, IGA is a greedy search-based approach, and utilizes forward steps to select features and backward elimination steps to remove redundant groups. IGA has been shown to be comparably computationally expensive as time-group LASSO (107). The IGA algorithm mimics L0 regularization by selecting and keeping features based on criterion function thresholds (Equation 4), whereas L0 regularization linearly weights each feature added as seen in Equation 5. The IGA criterion function, utilizes L2 regularization to fit selected features, and therefore IGA can be interpreted as applying an L2,0 regularization, so instead of a constant L0 penalty, it applies a dynamic penalty that is based on the gain of the criterion function. Initially, IGA's testing performance was poor, however, after L0 post-filtering, IGA achieved the best testing performance, suggesting the L0 post-filtering enhanced IGA's feature selection scheme.

Clinical parameters have been shown to be correlated with increased risk of treatment toxicity after SBRT (109,110). Therefore, a clinical model, including only clinical parameters such as patient-specific variables (age, baseline IPSS, prostate volume) and treatment variables

(ADT, nodal treatment, GTV boost, and spaceoar hydrogel usage), was compared to the dosimetric IGA regression model. IGA (with L0 post-filtering) was found to have higher testing performance than the clinical model. Moreover, combining clinical parameters with IGA dosimetric features into a hybrid model resulted in the same testing performance as IGA. Univariate analysis of clinical parameters in our training cohort showed there was no significant difference between GU grade 2 and grade < 2 toxicity groups, except for use of nodal treatment ($p < 0.03$). Thus, clinical parameters did not have significant predictive power and addition of clinical parameters did not improve the performance of the dosimetric IGA model.

IGA identified bladder V19.8 Gy and V20.5 Gy as the most important dosimetric predictors, which is consistent with the bladder V20Gy clinical dose constraint, followed by trigone V15.9 Gy and V18.2 Gy. Simulation/planning bladder dose had the greatest importance whereas fraction 4 trigone dose had the greatest importance among all its respective timepoints, suggesting daily trigone dose monitoring and potentially sparing (with treatment adaptation) may be beneficial in reducing GU toxicity. IGA also identified urethra V41.4 Gy and V41.7 Gy, which was consistent with the MIRAGE trial protocol and with GU toxicity literature as limiting urethral hotspot has been shown to reduce GU toxicity (111). However, IGA indicated low importance to urethral hotspot limitation. Low importance might stem from the urethra only being delineated during simulation, resulting in the urethral fractional dosimetric features being padded with simulation values, thus urethra daily dosimetric variations was not accurately evaluated for toxicity regression. Currently, the TrueFISP MRI sequence used for treatment planning and daily patient setup does not provide sufficient urethral contrast for delineation. Therefore, a HASTE sequence has been developed to provide urethral contrast for urethra-dose constraining treatment planning (101). However, the HASTE sequence has an acquisition time of

8 minutes which is longer than the 2-minute TrueFISP MRI, and thus prevents daily urethra image acquisition and dose monitoring without the disruption of clinical workflow. Future work will explore faster urethra image acquisition techniques in order to provide daily on-board urethra dosimetric evaluation.

A limitation of this study was the relatively small patient cohort, which limited the robustness of the feature selection approaches. As mentioned, the MIRAGE trial demonstrated MR-guided SBRT significantly reduced toxicity rates compared to CT-guided SBRT. Thus, new patients entering our institute are being offered and treated with a similar protocol as used in this study, allowing for a larger patient cohort to be accumulated, which can be used to develop more robust models for evaluation. A second limitation is this is a single-institution study, and all patients underwent similar treatment planning and were required to meet institutional constraints, thus there is minimal variation in DVH features amongst the cohort, making feature selection challenging. One possibility is to introduce large diversity by combining data from different institutions using variable constraints for a more heterogenous data set. Third, daily MRIs were registered to planning MRIs to estimate daily organ dose based on planned dose distributions, which may be different from the actual daily delivered dose, resulting in inaccurate features and weakened predictions. The rigidly transferred dose method used in this study was compared to daily delivered dose for a few patients and the dosimetric difference was found to be insignificant. Moreover, this study utilized granular DVH metrics, which are limited as they do not include spatial information. Therefore, DVH metrics are not able to detect small differences between patient treatment plans. Future work will be focused on implementing additional spatial features, such as MRI radiomics or dose distribution dosiomics, to better quantify differences between patient anatomy and dose distributions, and improve toxicity prediction (112,113).

Lastly, patient-reported toxicity measures may reflect other quality of life components to complement physician-scored CTCAE and may be incorporated into future studies for more comprehensive analysis endpoints (114).

5.5 Conclusion

Identification and analysis of fractional grouped dosimetric predictors with machine learning methods has been demonstrated and has the potential to predict GU toxicity. Awareness of sensitive bladder substructures such as the trigone, bladder wall, and urethra and the effect of radiation exposures to these substructures at multiple time points throughout SBRT may provide reliable dosimetric constraints to guide treatment planning. Overall, IGA-based logistic regression feature selection resulted in the best post-MRgRT SBRT GU toxicity prediction performance.

Chapter 6. Evidence-based Feasibility Study on Using Planning Dose as Surrogate for Actual Dose in Response Prediction

6.1 Introduction

Radiotherapy dose constraints have been studied extensively with the goal to optimize clinical outcome and treatment response (115). However, there is a long-standing logic gap in coping with this important family of variables in that while the clinical outcome truly depends on the actual received dose, dose constraint is typically imposed and assessed at the time of planning; before treatment. This limitation can be attributed to both lack of convenient mechanisms to record the actual delivered dose and the need to have planning guidelines. Efforts to bridge or minimize this planning dose surrogate map includes using perturbation analysis to account for possible inter- and intra- fraction anatomy variations with margins and uncertainty dose maps or adaptation schemes to introduce additional control (23–25). In this study, we take a different perspective and performed an evidence-based study to test the hypothesis that a planning-dose derived surrogate can be used as a proxy for the actual delivered dose for the purpose of response prediction. Specifically, we performed the analysis at two levels. First, we evaluated the plan versus delivered dose difference by comparing the daily dose delivered vs. the surrogate-derived dose calculated at planning, focusing on the major clinical planning dosimetric parameters. Second, we tested the actual impact on clinical response prediction using a regression map based on the surrogate derived daily dose.

6.2 Method and Materials

6.2.1 Data Description

Twenty prostate cancer patients from the MRI arm of the MIRAGE clinical trial (NCT0484770) who did not experience any treatment delivery interruptions were selected for this analysis. Patients were treated with stereotactic body radiation therapy (SBRT) using a 0.35T MR-LINAC (MRIdian, ViewRay Inc., Cleveland, OH, USA). During simulation, patients followed a bladder and rectum filling protocol and a 0.35T true fast imaging with steady state precession MRI (TrueFISP) was acquired for treatment planning. A CT scan was acquired and deformably registered to the planning MRI to provide electron density information. SBRT plans were prescribed to deliver 8 Gy per fraction for 5 fractions to the PTV. The complete clinical protocol can be found in Kishan *et* al (102).

Prior to each treatment fraction, a TrueFISP MRI was acquired. The bladder, bladder wall, rectum, rectal wall, and trigone were retrospectively contoured. The bladder and rectal walls were delineated by generating a 3 mm inner ring from the bladder and rectum contours. Daily dose distribution was estimated with two methods: 1) recalculation-based and 2) registration-based. With the recalculation approach, the daily electron density was derived from deformable registration of the simulation CT to the pre-treatment MRI, and planning monitor units and segments were applied to forward calculate the dose using a Monte Carlo algorithm with a statistical uncertainty of 1%. With the registration approach, the daily dose was estimated by transferring the planning dose distribution according to the estimated deformation between the daily and planning MRI. While the recalculation-based approach provided a more accurate representation of the daily dose distribution, it required proprietary knowledge of the machine parameters and beam models, adjudicated deformable registration of planning CT to daily MRI,

and a Monte Carlo dose calculation engine. The registration-based method only required MRI-MRI registration and we hypothesized that the registration-based method would provide a reasonable surrogate to the daily dose distribution and specifically tested out this hypothesis using the following two analyses.

6.2.2 Dose Volume Histogram Analysis

DVH constraints for the bladder, bladder wall, rectum, rectal wall, and trigone from the MIRAGE trial and literature were selected as dosimetric parameters (Table 6-1) (116–119). Additionally, organ mean and max doses were evaluated. Daily dose parameters from recalculation-based and registration-based methods were compared using a two-sided t-test ($p<0.05$).

Table 6-1. Prostate organ-at-risk (OAR) dose volume histogram (DVH) parameter based on MIRAGE trial and literature

Organ	**Dose Endpoint**
Bladder	V20 Gy (%), V40 Gy (%), D2 cc (Gy)
Bladder Wall	V20 Gy (%), V36 Gy (%)
Rectum	V20 Gy (%), V32 Gy (%), V36 Gy (%), V40 Gy (%), D2 cc (Gy)
Rectal Wall	V24 Gy (%), V39 Gy (%)
Trigone	V16 Gy (%), V43 Gy (%)

6.2.3 Regression Impact Analysis

Acute grade 2 or greater genitourinary (GU) toxicity based on physician-scored Common Terminology Criteria for Adverse Events, version 4.03 (CTCAE v4.03) scale, from the start of SBRT up to 90 days after SBRT was selected as the regression toxicity endpoint (103). Overall, 5/20 (25.0%) of patients reported acute grade 2 GU toxicity. We applied an existing fraction-wise logistic regression map, utilizing DVHs from both the simulation and daily urinary structures (bladder) and substructures (bladder wall, trigone) as the probing acute GU toxicity

model (120). Acute GU grade 2 toxicity prediction was compared between recalculation-based and registration-based methods using McNemar's test.

6.3 Results

Table 6-2 shows the daily dosimetric parameters difference between the recalculation-based and registration-based daily dose estimation methods. No statistically significant differences were observed except the trigone V16 Gy ($p=0.04$), with an absolute mean difference of 0.34%. Table 6-3 shows the contingency table for grade ≥ 2 GU toxicity prediction using fraction-wise logistic regression with recalculation-based and registration-based daily dose estimation methods. Both methods correctly predicted 15/20 (75%) of the responses in this 20-patient cohort with McNemar's test p-value of 1, indicating no statistically significance between toxicity predictions.

Table 6-2. Daily dose parameter difference between recalculation-based and registration-based daily dose estimation methods

Organ	Dosimetric Endpoint	Mean Difference	STD Difference	p-value (two-tail)
	V20 Gy (%)	-0.03	0.78	0.68
Bladder	V40 Gy (%)	0.00	0.27	0.99
	D2 cc (Gy)	-0.08	0.79	0.31
	Mean (Gy)	0.00	0.27	0.96
	Max (Gy)	0.05	0.51	0.32
	V20 Gy (%)	-0.06	0.67	0.40
Bladder Wall	V36 Gy (%)	-0.07	0.68	0.30
	Mean (Gy)	-0.01	0.25	0.65
	Max (Gy)	0.04	0.49	0.42
	V20 Gy (%)	0.08	1.30	0.54
	V32 Gy (%)	0.05	0.55	0.39
	V36 Gy (%)	0.03	0.39	0.42
Rectum	V40 Gy (%)	0.00	0.18	0.83
	D2 cc (Gy)	0.08	0.89	0.39
	Mean (Gy)	0.02	0.23	0.36
	Max (Gy)	-0.02	0.83	0.84
	V24 Gy (%)	0.08	1.11	0.47
Rectal Wall	V39 Gy (%)	0.03	0.41	0.50
	Mean (Gy)	0.02	0.24	0.32
	Max (Gy)	-0.02	0.83	0.84
	V16 Gy (%)	-0.34	1.62	0.04
Trigone	V43 Gy (%)	0.02	0.23	0.34
	Mean (Gy)	-0.14	0.84	0.09
	Max (Gy)	-0.08	0.60	0.22

Table 6-3. Contingency table for grade ≥ 2 GU toxicity prediction using fraction-wise logistic regression with recalculation-based and registration-based daily dose estimation methods

		Registration-based	
		Grade ≥ 2 GU Toxicity	Grade < 2 GU Toxicity
Re-calculation-based	Grade ≥ 2 GU Toxicity	12	3
	Grade < 2 GU Toxicity	2	3

6.4 Discussion

Current MRgRT planning deformably registers simulation CT to simulation planning MRI to provide electron density information for planning dose distribution estimation. The recalculation-based approach follows a similar procedure to obtain daily dose. While deforming simulation CT to daily MRI may yield some inconsistency in electron density, studies have shown that pseudo electron density generation and possible dose distribution variations due to transient gas bubbles minimally impact dose (120,121). Therefore, recalculation provides a reasonable clinical reference for daily dose. This study provides evidence for the feasibility of using planning dose distribution registration as a surrogate for the daily dose distribution. The use of a surrogate based on the planning dose distribution is desirable because informed clinical decisions need to be made before the actual treatment is started. It is also convenient to circumvent the complexity of generating and processing daily high-quality on-table electron-density maps to support dose recalculation.

In this patient cohort, none of the cases had online adaptation or treatment re-optimization. Registration-based daily dose estimation showed no statistically significant difference from recalculation-based daily dose estimation for all urinary structure dose

parameters, except for the trigone V16, which can stem from the trigone being a small urinary substructure and sensitive to dose perturbation and uncertainty from dose calculation. The absolute mean difference observed in trigone V16 was 0.34%, which is within the 1% dose calculation uncertainty used and arguably has no clinical significance. Furthermore, when tested against response of grade ≥ 2 GU toxicity, the regression showed no statistical difference, despite the difference in trigone DVH metrics. This alludes to the observation that while small structures located at high dose gradient regions may be subject to higher dose metric approximation errors, they also exhibit high variations across patients and treatment fractions, leading to reduced contribution in robust regression models. Therefore, when response regression is considered holistically, registration-based dose distribution can be used as a surrogate to the daily dose.

This pilot study selected 20 patients whose treatment delivery fractions were uninterrupted and unadapted to ensure the reliability of the response regression. It is desirable to increase the cohort size for further robustness analysis. Nevertheless, we demonstrated that probability of the two estimations being significantly different is small and likely clinically insignificant; the impact in response prediction is also minimal.

6.5 Conclusion

When planning dose is propagated via registration to daily treatment imaging and is used as a surrogate to recalculation-based daily dose distribution estimation, only small and clinically insignificant absolute dose difference is observed. Moreover, this surrogate works well for response prediction based on this pilot study. A larger cohort is desired to further validate this finding.

Bibliography

1. Siegel RL, Miller KD, Jemal A. Cancer statistics, 2020. *CA Cancer J Clin* (2020) **70**:7–30. doi: 10.3322/CAAC.21590

2. Hegemann N-S, Guckenberger M, Belka C, Ganswindt U, Manapov F, Li M. Hypofractionated radiotherapy for prostate cancer. (2014). doi: 10.1186/s13014-014-0275-6

3. Catton CN, Lukka H, Martin J. Prostate cancer radiotherapy: An evolving paradigm. *J Clin Oncol* (2018) **36**:2909–2913. doi: 10.1200/JCO.2018.79.3257

4. Catton CN, Lukka H, Gu CS, Martin JM, Supiot S, Chung PWM, Bauman GS, Bahary JP, Ahmed S, Cheung P, et al. Randomized Trial of a Hypofractionated Radiation Regimen for the Treatment of Localized Prostate Cancer. *J Clin Oncol* (2017) **35**:1884–1890. doi: 10.1200/JCO.2016.71.7397

5. Lee WR, Dignam JJ, Amin MB, Bruner DW, Low D, Swanson GP, Shah AB, D'Souza DP, Michalski JM, Dayes IS, et al. Randomized Phase III Noninferiority Study Comparing Two Radiotherapy Fractionation Schedules in Patients With Low-Risk Prostate Cancer. *J Clin Oncol* (2016) **34**:2325–2332. doi: 10.1200/JCO.2016.67.0448

6. Dearnaley D, Syndikus I, Mossop H, Khoo V, Birtle A, Bloomfield D, Graham J, Kirkbride P, Logue J, Malik Z, et al. Conventional versus hypofractionated high-dose intensity-modulated radiotherapy for prostate cancer: 5-year outcomes of the randomised, non-inferiority, phase 3 CHHiP trial. *Lancet Oncol* (2016) **17**:1047–1060. doi: 10.1016/S1470-2045(16)30102-4

7. Brand DH, Tree AC, Ostler P, van der Voet H, Loblaw A, Chu W, Ford D, Tolan S, Jain S, Martin A, et al. Intensity-modulated fractionated radiotherapy versus stereotactic body radiotherapy for prostate cancer (PACE-B): acute toxicity findings from an international, randomised, open-label, phase 3, non-inferiority trial. *Lancet Oncol* (2019) **20**:1531–1543. doi: 10.1016/S1470-2045(19)30569-8/ATTACHMENT/F9776432-045B-4658-9ED8-001722D244A2/MMC1.PDF

8. Kishan AU, Dang A, Katz AJ, Mantz CA, Collins SP, Aghdam N, Chu FI, Kaplan ID, Appelbaum L, Fuller DB, et al. Long-term Outcomes of Stereotactic Body Radiotherapy for Low-Risk and Intermediate-Risk Prostate Cancer. *JAMA Netw Open* (2019) **2**:e188006–e188006. doi: 10.1001/JAMANETWORKOPEN.2018.8006

9. Tree AC, Ostler P, van der Voet H, Chu W, Loblaw A, Ford D, Tolan S, Jain S, Martin A, Staffurth J, et al. Intensity-modulated radiotherapy versus stereotactic body radiotherapy for prostate cancer (PACE-B): 2-year toxicity results from an open-label, randomised, phase 3, non-inferiority trial. *Lancet Oncol* (2022) **23**:1308–1320. doi: 10.1016/S1470-2045(22)00517-4

10. Cheung MR, Tucker SL, Dong L, de Crevoisier R, Lee AK, Frank S, Kudchadker RJ, Thames H, Mohan R, Kuban D. Investigation of bladder dose and volume factors influencing late urinary toxicity after external beam radiotherapy for prostate cancer. *Int J*

Radiat Oncol Biol Phys (2007) **67**:1059–1065. doi: 10.1016/J.IJROBP.2006.10.042

11. D'Avino V, Palma G, Liuzzi R, Conson M, Doria F, Salvatore M, Pacelli R, Cella L. Prediction of gastrointestinal toxicity after external beam radiotherapy for localized prostate cancer. *Radiat Oncol* (2015) **10**:1–9. doi: 10.1186/S13014-015-0389-5/FIGURES/5

12. Hackman G, Taari K, Tammela TL, Matikainen M, Kouri M, Joensuu T, Luukkaala T, Salonen A, Isotalo T, Pétas A, et al. Randomised Trial of Adjuvant Radiotherapy Following Radical Prostatectomy Versus Radical Prostatectomy Alone in Prostate Cancer Patients with Positive Margins or Extracapsular Extension. *Eur Urol* (2019) **76**:586–595. doi: 10.1016/J.EURURO.2019.07.001

13. Thompson IM, Tangen CM, Paradelo J, Lucia MS, Miller G, Troyer D, Messing E, Forman J, Chin J, Swanson G, et al. Adjuvant Radiotherapy for Pathological T3N0M0 Prostate Cancer Significantly Reduces Risk of Metastases and Improves Survival: Long-Term Followup of a Randomized Clinical Trial. *J Urol* (2009) **181**:956–962. doi: 10.1016/J.JURO.2008.11.032

14. Wiegel T, Bartkowiak D, Bottke D, Bronner C, Steiner U, Siegmann A, Golz R, Störkel S, Willich N, Semjonow A, et al. Adjuvant Radiotherapy Versus Wait-and-See After Radical Prostatectomy: 10-year Follow-up of the ARO 96–02/AUO AP 09/95 Trial. *Eur Urol* (2014) **66**:243–250. doi: 10.1016/J.EURURO.2014.03.011

15. Bolla M, Van Poppel H, Tombal B, Vekemans K, Da Pozzo L, De Reijke TM, Verbaeys A, Bosset JF, Van Velthoven R, Colombel M, et al. Postoperative radiotherapy after radical prostatectomy for high-risk prostate cancer: long-term results of a randomised controlled trial (EORTC trial 22911). *Lancet (London, England)* (2012) **380**:2018–2027. doi: 10.1016/S0140-6736(12)61253-7

16. Amling CL, Blute ML, Bergstralh EJ, Seay TM, Slezak J, Zincke H. LONG-TERM HAZARD OF PROGRESSION AFTER RADICAL PROSTATECTOMY FOR CLINICALLY LOCALIZED PROSTATE CANCER: CONTINUED RISK OF BIOCHEMICAL FAILURE AFTER 5 YEARS. *J Urol* (2000) **164**:101–105. doi: 10.1016/S0022-5347(05)67457-5

17. Mullins JK, Feng Z, Trock BJ, Epstein JI, Walsh PC, Loeb S. The Impact of Anatomical Radical Retropubic Prostatectomy on Cancer Control: The 30-Year Anniversary. *J Urol* (2012) **188**:2219–2224. doi: 10.1016/J.JURO.2012.08.028

18. Bianco FJ, Scardino PT, Eastham JA. Radical prostatectomy: Long-term cancer control and recovery of sexual and urinary function ("trifecta"). *Urology* (2005) **66**:83–94. doi: 10.1016/J.UROLOGY.2005.06.116

19. Han M, Partin AW, Zahurak M, Piantadosi S, Epstein JI, Walsh PC. Biochemical (Prostate Specific Antigen) Recurrence Probability Following Radical Prostatectomy for Clinically Localized Prostate Cancer. *J Urol* (2003) **169**:517–523. doi: 10.1016/S0022-5347(05)63946-8

20. Hawken SR, Spratt DE, Qi J, Linsell SM, Cher ML, Ghani KR, Miller DC, Montie JE,

Morgan TM. Utilization of Salvage Radiation Therapy for Biochemical Recurrence After Radical Prostatectomy. *Int J Radiat Oncol* (2019) **104**:1030–1034. doi: 10.1016/J.IJROBP.2019.01.006

21. Kishan AU, Duchesne G, Wang PC, Rwigema JCM, Kishan AU, Saigal C, Rettig M, Steinberg ML, King CR. Discord among radiation oncologists and urologists in the postoperative management of high-risk prostate cancer. *Am J Clin Oncol Cancer Clin Trials* (2018) **41**:739–746. doi: 10.1097/COC.0000000000000381

22. Sineshaw HM, Gray PJ, Efstathiou JA, Jemal A. Declining Use of Radiotherapy for Adverse Features After Radical Prostatectomy: Results From the National Cancer Data Base. *Eur Urol* (2015) **68**:768–774. doi: 10.1016/J.EURURO.2015.04.003

23. Cao M, Gao Y, Yoon SM, Yang Y, Sheng K, Ballas LK, Basehart V, Sachdeva A, Felix C, Low DA, et al. Interfractional Geometric Variations and Dosimetric Benefits of Stereotactic MRI Guided Online Adaptive Radiotherapy (SMART) of Prostate Bed after Radical Prostatectomy: Post-Hoc Analysis of a Phase II Trial. *Cancers (Basel)* (2021) **13**: doi: 10.3390/CANCERS13112802

24. Yoon S, Cao M, Aghdam N, Shabsovich D, Kahlon S, Ballas L, Collins S, Steinberg ML, Kishan AU. Prostate bed and organ-at-risk deformation: Prospective volumetric and dosimetric data from a phase II trial of stereotactic body radiotherapy after radical prostatectomy. *Radiother Oncol* (2020) **148**:44–50. doi: 10.1016/J.RADONC.2020.04.007

25. Nikitas J, Smith LM, Gao Y, Martin Ma T, Sachdeva A, Yoon SM, Jiang T, Low DA, Ballas LK, Steinberg ML, et al. The role of adaptive planning in margin-reduced, MRI-guided stereotactic body radiotherapy to the prostate bed following radical prostatectomy: Post-hoc analysis of a phase II clinical trial. *Radiother Oncol* (2023) **183**:109631. doi: 10.1016/J.RADONC.2023.109631

26. Ma TM, Ballas LK, Wilhalme H, Sachdeva A, Chong N, Sharma S, Yang T, Basehart V, Reiter RE, Saigal C, et al. Quality-of-Life Outcomes and Toxicity Profile Among Patients With Localized Prostate Cancer After Radical Prostatectomy Treated With Stereotactic Body Radiation: The SCIMITAR Multicenter Phase 2 Trial. *Int J Radiat Oncol Biol Phys* (2023) **115**:142–152. doi: 10.1016/J.IJROBP.2022.08.041

27. Pathmanathan AU, Schmidt MA, Brand DH, Kousi E, van As NJ, Tree AC. Improving fiducial and prostate capsule visualization for radiotherapy planning using MRI. *J Appl Clin Med Phys* (2019) **20**:27–36. doi: 10.1002/ACM2.12529

28. Commandeur F, Simon A, Mathieu R, Nassef M, Arango JDO, Rolland Y, Haigron P, De Crevoisier R, Acosta O. MRI to CT Prostate Registration for Improved Targeting in Cancer External Beam Radiotherapy. *IEEE J Biomed Heal Informatics* (2017) **21**:1015–1026. doi: 10.1109/JBHI.2016.2581881

29. Lim-Reinders S, Keller BM, Al-Ward S, Sahgal A, Kim A. Online Adaptive Radiation Therapy. *Int J Radiat Oncol* (2017) **99**:994–1003. doi: 10.1016/J.IJROBP.2017.04.023

30. Nicosia L, Sicignano G, Rigo M, Figlia V, Cuccia F, De Simone A, Giaj-Levra N, Mazzola R, Naccarato S, Ricchetti F, et al. Daily dosimetric variation between image-

guided volumetric modulated arc radiotherapy and MR-guided daily adaptive radiotherapy for prostate cancer stereotactic body radiotherapy. *https://doi.org/101080/0284186X20201821090* (2020) **60**:215–221. doi: 10.1080/0284186X.2020.1821090

31. Fischer-Valuck BW, Henke L, Green O, Kashani R, Acharya S, Bradley JD, Robinson CG, Thomas M, Zoberi I, Thorstad W, et al. Two-and-a-half-year clinical experience with the world's first magnetic resonance image guided radiation therapy system. *Adv Radiat Oncol* (2017) **2**:485–493. doi: 10.1016/J.ADRO.2017.05.006

32. Tocco BR, Kishan AU, Ma TM, Kerkmeijer LGW, Tree AC. MR-Guided Radiotherapy for Prostate Cancer. *Front Oncol* (2020) **10**:2763. doi: 10.3389/FONC.2020.616291/BIBTEX

33. Bruynzeel AME, Tetar SU, Oei SS, Senan S, Haasbeek CJA, Spoelstra FOB, Piet AHM, Meijnen P, Bakker van der Jagt MAB, Fraikin T, et al. A Prospective Single-Arm Phase 2 Study of Stereotactic Magnetic Resonance Guided Adaptive Radiation Therapy for Prostate Cancer: Early Toxicity Results. *Int J Radiat Oncol Biol Phys* (2019) **105**:1086–1094. doi: 10.1016/J.IJROBP.2019.08.007

34. Michalet M, Riou O, Valdenaire S, Debuire P, Ailleres N, Draghici R, Charissoux M, Moscardo CL, Farcy-Jacquet MP, Fenoglietto P, et al. Magnetic Resonance-Guided Reirradiation for Local Recurrence Within the Prostate or in the Prostate Bed: Preliminary Results of a Prospective Registry Study. *Adv Radiat Oncol* (2021) **6**: doi: 10.1016/J.ADRO.2021.100748

35. Okamoto H, Nishioka S, Iijima K, Nakamura S, Sakasai T, Miura Y, Takemori M, Nakayama H, Morishita Y, Shimizu M, et al. Monte Carlo modeling of a 60Co MRI-guided radiotherapy system on Geant4 and experimental verification of dose calculation under a magnetic field of 0.35 T. *J Radiat Res* (2019) **60**:116–123. doi: 10.1093/JRR/RRY087

36. Park JM, Shin KH, Kim J in, Park SY, Jeon SH, Choi N, Kim JH, Wu HG. Air–electron stream interactions during magnetic resonance IGRT: Skin irradiation outside the treatment field during accelerated partial breast irradiation. *Strahlentherapie und Onkol* (2018) **194**:50–59. doi: 10.1007/s00066-017-1212-z

37. Cusumano D, Teodoli S, Greco F, Fidanzio A, Boldrini L, Massaccesi M, Cellini F, Valentini V, Azario L, De Spirito M. Experimental evaluation of the impact of low tesla transverse magnetic field on dose distribution in presence of tissue interfaces. *Phys Medica* (2018) **53**:80–85. doi: 10.1016/J.EJMP.2018.08.007

38. Steinmann A, O'Brien D, Stafford R, Sawakuchi G, Wen Z, Court L, Fuller C, Followill D. Investigation of TLD and EBT3 performance under the presence of 1.5T, 0.35T, and 0T magnetic field strengths in MR/CT visible materials. *Med Phys* (2019) **46**:3217–3226. doi: 10.1002/mp.13527

39. Steinmann A, Alvarez P, Lee H, Court L, Stafford R, Sawakuchi G, Wen Z, Fuller C, Followill D. MRIgRT dynamic lung motion thorax anthropomorphic QA phantom: Design, development, reproducibility, and feasibility study. *Med Phys* (2019) **46**:5124–

5133. doi: 10.1002/mp.13757

40. Steinmann A, Alvarez P, Lee H, Court L, Stafford R, Sawakuchi G, Wen Z, Fuller CD, Followill D. MRIgRT head and neck anthropomorphic QA phantom: Design, development, reproducibility, and feasibility study. *Med Phys* (2020) **47**:604–613. doi: 10.1002/mp.13951

41. Pappas E, Kalaitzakis G, Boursianis T, Zoros E, Zourari K, Pappas EP, Makris D, Seimenis I, Efstathopoulos E, Maris TG. Dosimetric performance of the Elekta Unity MR-linac system: 2D and 3D dosimetry in anthropomorphic inhomogeneous geometry. *Phys Med Biol* (2019) **64**: doi: 10.1088/1361-6560/ab52ce

42. Okamoto H, Nishioka S, Iijima K, Nakamura S, Sakasai T, Miura Y, Takemori M, Nakayama H, Morishita Y, Shimizu M, et al. Monte Carlo modeling of a 60 Co MRI-guided radiotherapy system on Geant4 and experimental verification of dose calculation under a magnetic field of 0.35 T. *J Radiat Res* (2019) **60**:116–123. doi: 10.1093/jrr/rry087

43. Cusumano D, Teodoli S, Greco F, Fidanzio A, Boldrini L, Massaccesi M, Cellini F, Valentini V, Azario L, De Spirito M. Experimental evaluation of the impact of low tesla transverse magnetic field on dose distribution in presence of tissue interfaces. *Phys Medica* (2018) **53**:80–85. doi: 10.1016/j.ejmp.2018.08.007

44. Shortall J, Vasquez Osorio E, Aitkenhead A, Berresford J, Agnew J, Budgell G, Chuter R, McWilliam A, Kirkby K, Mackay R, et al. Experimental verification the electron return effect around spherical air cavities for the MR-Linac using Monte Carlo calculation. *Med Phys* (2020) **47**:2506–2515. doi: 10.1002/mp.14123

45. Bol GH, Lagendijk JJW, Raaymakers BW. Compensating for the impact of non-stationary spherical air cavities on IMRT dose delivery in transverse magnetic fields. *Phys Med Biol* (2015) **60**:755–768. doi: 10.1088/0031-9155/60/2/755

46. Shortall J, Vasquez Osorio E, Chuter R, McWilliam A, Choudhury A, Kirkby K, Mackay R, van Herk M. Assessing localized dosimetric effects due to unplanned gas cavities during pelvic MR-guided radiotherapy using Monte Carlo simulations. *Med Phys* (2019) **46**:5807–5815. doi: 10.1002/mp.13857

47. Shortall J, Vasquez Osorio E, Cree A, Song Y, Dubec M, Chuter R, Price G, McWilliam A, Kirkby K, Mackay R, et al. Inter- and intra-fractional stability of rectal gas in pelvic cancer patients during MRIgRT. *Med Phys* (2021) **48**:414–426. doi: 10.1002/mp.14586

48. Uilkema S, Van Der Heide U, Sonke JJ, Moreau M, Van Triest B, Nijkamp J. A 1.5 T transverse magnetic field in radiotherapy of rectal cancer: Impact on the dose distribution. *Med Phys* (2015) **42**: doi: 10.1118/1.4936097

49. Godoy Scripes P, Subashi E, Burleson S, Liang J, Romesser P, Crane C, Mechalakos J, Hunt M, Tyagi N. Impact of varying air cavity on planning dosimetry for rectum patients treated on a 1.5 T hybrid MR-linac system. *J Appl Clin Med Phys* (2020) **21**:144–152. doi: 10.1002/acm2.12903

50. Winkel D, Bol GH, Kroon PS, van Asselen B, Hackett SS, Werensteijn-Honingh AM,

Intven MPW, Eppinga WSC, Tijssen RHN, Kerkmeijer LGW, et al. Adaptive radiotherapy: The Elekta Unity MR-linac concept. *Clin Transl Radiat Oncol* (2019) **18**:54–59. doi: 10.1016/J.CTRO.2019.04.001

51. Hsu SH, Zawisza I, O'Grady K, Peng Q, Tomé WA. Towards abdominal MRI-based treatment planning using population-based Hounsfield units for bulk density assignment. *Phys Med Biol* (2018) **63**: doi: 10.1088/1361-6560/aacfb1

52. Hoogcarspel SJ, Van Der Velden JM, Lagendijk JJW, Van Vulpen M, Raaymakers BW. The feasibility of utilizing pseudo CT-data for online MRI based treatment plan adaptation for a stereotactic radiotherapy treatment of spinal bone metastases. *Phys Med Biol* (2014) **59**:7383–7391. doi: 10.1088/0031-9155/59/23/7383

53. Nicosia L, Sicignano G, Rigo M, Figlia V, Cuccia F, De Simone A, Giaj-Levra N, Mazzola R, Naccarato S, Ricchetti F, et al. Daily dosimetric variation between image-guided volumetric modulated arc radiotherapy and MR-guided daily adaptive radiotherapy for prostate cancer stereotactic body radiotherapy. *Acta Oncol* (2021) **60**:215–221. doi: 10.1080/0284186X.2020.1821090

54. Guo Y, Wu X, Wang Z, Pei X, Xu XG. End-to-end unsupervised cycle-consistent fully convolutional network for 3D pelvic CT-MR deformable registration. *J Appl Clin Med Phys* (2020) **21**:193–200. doi: 10.1002/ACM2.12968

55. Khan AU, Simiele EA, Lotey R, DeWerd LA, Yadav P. Development and evaluation of a GEANT4-based Monte Carlo Model of a 0.35 T MR-guided radiation therapy (MRgRT) linear accelerator. *Med Phys* (2021) **48**:1967–1982. doi: 10.1002/MP.14761

56. Brand DH, Tree AC, Ostler P, van der Voet H, Loblaw A, Chu W, Ford D, Tolan S, Jain S, Martin A, et al. Intensity-modulated fractionated radiotherapy versus stereotactic body radiotherapy for prostate cancer (PACE-B): acute toxicity findings from an international, randomised, open-label, phase 3, non-inferiority trial. *Lancet Oncol* (2019) **20**:1531–1543. doi: 10.1016/S1470-2045(19)30569-8

57. Kishan AU, Dang A, Katz AJ, Mantz CA, Collins SP, Aghdam N, Chu FI, Kaplan ID, Appelbaum L, Fuller DB, et al. Long-term Outcomes of Stereotactic Body Radiotherapy for Low-Risk and Intermediate-Risk Prostate Cancer. *JAMA Netw Open* (2019) **2**:e188006–e188006. doi: 10.1001/JAMANETWORKOPEN.2018.8006

58. Widmark A, Gunnlaugsson A, Beckman L, Thellenberg-Karlsson C, Hoyer M, Lagerlund M, Kindblom J, Ginman C, Johansson B, Björnlinger K, et al. Ultra-hypofractionated versus conventionally fractionated radiotherapy for prostate cancer: 5-year outcomes of the HYPO-RT-PC randomised, non-inferiority, phase 3 trial. *Lancet* (2019) **394**:385–395. doi: 10.1016/S0140-6736(19)31131-6

59. Kataria T, Gupta D, Goyal S, Bisht SS, Chaudhary R, Narang K, Banerjee S, Basu T, Abhishek A, Sambasivam S, et al. Simple diagrammatic method to delineate male urethra in prostate cancer radiotherapy: An MRI based approach. *Br J Radiol* (2016) **89**: doi: 10.1259/bjr.20160348

60. Waterman FM, Dicker AP. Determination of the urethral dose in prostate brachytherapy

when the urethra cannot be visualized in the postimplant CT scan. *Med Phys* (2000) **27**:448–451. doi: 10.1118/1.598912

61. Kawashima A, Sandler CM, Wasserman NF, Leroy AJ, King BF, Goldman SM. Imaging of urethral disease: A pictorial review. *Radiographics* (2004) **24**: doi: 10.1148/rg.24si045504

62. Ko YH, Kim TH, Song PH, Kim BH, Kim BS, Kim KH, Cho J. Structural Variations of the Prostatic Urethra Within the Prostate Predict the Severities of Obstructive Symptoms: A Prospective Multicenter Observational Study. *Urology* (2017) **104**:160–165. doi: 10.1016/j.urology.2017.03.014

63. Litzenberg DW, Muenz DG, Archer PG, Jackson WC, Hamstra DA, Hearn JW, Schipper MJ, Spratt DE. Changes in prostate orientation due to removal of a Foley catheter. *Med Phys* (2018) **45**:1369–1378. doi: 10.1002/mp.12830

64. Lee HK, D'Souza WD, Yamal JMJ, Pollack A, Lee AK, Palmer MB, Kuban DA. Dosimetric consequences of using a surrogate urethra to estimate urethral dose after brachytherapy for prostate cancer. *Int J Radiat Oncol Biol Phys* (2003) **57**:355–361. doi: 10.1016/S0360-3016(03)00583-2

65. Dekura Y, Nishioka K, Hashimoto T, Miyamoto N, Suzuki R, Yoshimura T, Matsumoto R, Osawa T, Abe T, Ito YM, et al. The urethral position may shift due to urethral catheter placement in the treatment planning for prostate radiation therapy. doi: 10.1186/s13014-019-1424-8

66. Ulin K, Urie MM, Cherlow JM. Results of a multi-institutional benchmark test for cranial CT/MR image registration. *Int J Radiat Oncol Biol Phys* (2010) **77**:1584–1589. doi: 10.1016/j.ijrobp.2009.10.017

67. Kotecha R, Djemil T, Tendulkar RD, Reddy CA, Thousand RA, Vassil A, Stovsky M, Berglund RK, Klein EA, Stephans KL. Dose-Escalated Stereotactic Body Radiation Therapy for Patients With Intermediate- and High-Risk Prostate Cancer: Initial Dosimetry Analysis and Patient Outcomes. *Int J Radiat Oncol Biol Phys* (2016) **95**:960–964. doi: 10.1016/j.ijrobp.2016.02.009

68. Tetar SU, Bruynzeel AME, Lagerwaard FJ, Slotman BJ, Bohoudi O, Palacios MA. Clinical implementation of magnetic resonance imaging guided adaptive radiotherapy for localized prostate cancer. *Phys Imaging Radiat Oncol* (2019) **9**:69–76. doi: 10.1016/j.phro.2019.02.002

69. Tetar SU, Bruynzeel AME, Oei SS, Senan S, Fraikin T, Slotman BJ, Moorselaar RJA van, Lagerwaard FJ. Magnetic Resonance-guided Stereotactic Radiotherapy for Localized Prostate Cancer: Final Results on Patient-reported Outcomes of a Prospective Phase 2 Study. *Eur Urol Oncol* (2020) doi: 10.1016/j.euo.2020.05.007

70. Takeda T, Tin AL, Corradi RB, Mamoor M, Benfante NE, Sjoberg DD, Scardino PT, Eastham JA, Fine SW, Touijer KA. Topography of Prostate Cancer Recurrence After Radiation Therapy: A Detailed Mapping Study of Salvage Radical Prostatectomy Specimens. *Eur Urol* (2018) **73**:488–490. doi: 10.1016/j.eururo.2017.08.005

71. Frank H. Netter. *Atlas of human anatomy*. 7th ed. Elsevier (2017). 656 p.

72. Zakian KL, Wibmer A, Vargas HA, Alberts E, Kadbi M, Mychalczak B, Kollmeier M, Gorovets D, McBride S, Hunt M, et al. Comparison of Motion-Insensitive T2-Weighted MRI Pulse Sequences for Visualization of the Prostatic Urethra During MR Simulation. *Pract Radiat Oncol* (2019) **9**:e534–e540. doi: 10.1016/j.prro.2019.06.009

73. Stoddard N, Leslie SW. *Histology, Male Urethra*. StatPearls Publishing (2020). http://www.ncbi.nlm.nih.gov/pubmed/31194395 [Accessed July 29, 2020]

74. Mohler JL, Antonarakis ES, Armstrong AJ, D'Amico A V., Davis BJ, Dorff T, Eastham JA, Enke CA, Farrington TA, Higano CS, et al. Prostate Cancer, Version 2.2019, NCCN Clinical Practice Guidelines in Oncology. *J Natl Compr Canc Netw* (2019) **17**:479–505. doi: 10.6004/JNCCN.2019.0023

75. Widmark A, Gunnlaugsson A, Beckman L, Thellenberg-Karlsson C, Hoyer M, Lagerlund M, Kindblom J, Ginman C, Johansson B, Björnlinger K, et al. Ultra-hypofractionated versus conventionally fractionated radiotherapy for prostate cancer: 5-year outcomes of the HYPO-RT-PC randomised, non-inferiority, phase 3 trial. *Lancet* (2019) **394**:385–395. doi: 10.1016/S0140-6736(19)31131-6/ATTACHMENT/BE42A27F-79B9-4D7D-93AE-F4FF9FDFE327/MMC1.PDF

76. Ma TM, Lamb JM, Casado M, Wang X, Basehart TV, Yang Y, Low D, Sheng K, Agazaryan N, Nickols NG, et al. Magnetic resonance imaging-guided stereotactic body radiotherapy for prostate cancer (mirage): a phase iii randomized trial. *BMC Cancer* (2021) **21**: doi: 10.1186/S12885-021-08281-X

77. Cheung MR, Tucker SL, Dong L, de Crevoisier R, Lee AK, Frank S, Kudchadker RJ, Thames H, Mohan R, Kuban D. Investigation of bladder dose and volume factors influencing late urinary toxicity after external beam radiotherapy for prostate cancer. *Int J Radiat Oncol Biol Phys* (2007) **67**:1059–1065. doi: 10.1016/J.IJROBP.2006.10.042

78. Wang K, Mavroidis P, Royce TJ, Falchook AD, Collins SP, Sapareto S, Sheets NC, Fuller DB, El Naqa I, Yorke E, et al. Prostate Stereotactic Body Radiation Therapy: An Overview of Toxicity and Dose Response. *Int J Radiat Oncol Biol Phys* (2021) **110**:237–248. doi: 10.1016/J.IJROBP.2020.09.054/ATTACHMENT/3115C618-1565-42D0-9072-4BE340E8138D/MMC1.DOCX

79. Leeman JE, Chen YH, Catalano P, Bredfeldt J, King M, Mouw KW, D'Amico A V., Orio P, Nguyen PL, Martin N. Radiation Dose to the Intraprostatic Urethra Correlates Strongly With Urinary Toxicity After Prostate Stereotactic Body Radiation Therapy: A Combined Analysis of 23 Prospective Clinical Trials. *Int J Radiat Oncol Biol Phys* (2022) **112**:75–82. doi: 10.1016/J.IJROBP.2021.06.037

80. Zilli T, Jorcano S, Bral S, Rubio C, Bruynzeel AME, Oliveira A, Abacioglu U, Minn H, Symon Z, Miralbell R. Once-a-week or every-other-day urethra-sparing prostate cancer stereotactic body radiotherapy, a randomized phase II trial: 18 months follow-up results. *Cancer Med* (2020) **9**:3097–3106. doi: 10.1002/CAM4.2966

81. Hannan R, Tumati V, Xie X-J, Cho LC, Kavanagh BD, Brindle J, Raben D, Nanda A,

Cooley S, Kim DWN, et al. Stereotactic body radiation therapy for low and intermediate risk prostate cancerdResults from a multi-institutional clinical trial *. *Eur J Cancer* (2016) **59**:142–151. doi: 10.1016/j.ejca.2016.02.014

82. Takeda T, Tin AL, Corradi RB, Mamoor M, Benfante NE, Sjoberg DD, Scardino PT, Eastham JA, Fine SW, Touijer KA. Topography of Prostate Cancer Recurrence After Radiation Therapy: A Detailed Mapping Study of Salvage Radical Prostatectomy Specimens. *Eur Urol* (2018) **73**:488–490. doi: 10.1016/J.EURURO.2017.08.005

83. Waterman FM, Dicker AP. Determination of the urethral dose in prostate brachytherapy when the urethra cannot be visualized in the postimplant CT scan. *Med Phys* (2000) **27**:448–451. doi: 10.1118/1.598912

84. Litzenberg DW, Muenz DG, Archer PG, Jackson WC, Hamstra DA, Hearn JW, Schipper MJ, Spratt DE. Changes in prostate orientation due to removal of a Foley catheter. (2018) doi: 10.1002/mp.12830

85. Kataria T, Gupta D, Goyal S, Bisht SS, Chaudhary R, Narang K, Banerjee S, Basu T, Abhishek A, Sambasivam S, et al. Simple diagrammatic method to delineate male urethra in prostate cancer radiotherapy: an MRI based approach. *Br J Radiol* (2016) **89**: doi: 10.1259/BJR.20160348

86. Zakian KL, Wibmer A, Vargas HA, Alberts E, Kadbi M, Mychalczak B, Kollmeier M, Gorovets D, McBride S, Hunt M, et al. Comparison of Motion-Insensitive T2-Weighted MRI Pulse Sequences for Visualization of the Prostatic Urethra During MR Simulation. *Pract Radiat Oncol* (2019) **9**:e534–e540. doi: 10.1016/J.PRRO.2019.06.009

87. Richardson M, Skehan K, Wilton L, Sams J, Samuels J, Goodwin J, Greer P, Sridharan S, Martin J. Visualising the urethra for prostate radiotherapy planning. *J Med Radiat Sci* (2021) **68**:282–288. doi: 10.1002/JMRS.485

88. Commandeur F, Simon A, Mathieu R, Nassef M, Arango JDO, Rolland Y, Haigron P, De Crevoisier R, Acosta O. MRI to CT Prostate Registration for Improved Targeting in Cancer External Beam Radiotherapy. *IEEE J Biomed Heal Informatics* (2017) **21**:1015–1026. doi: 10.1109/JBHI.2016.2581881

89. Pathmanathan AU, Schmidt MA, Brand DH, Kousi E, van As NJ, Tree AC. Improving fiducial and prostate capsule visualization for radiotherapy planning using MRI. *J Appl Clin Med Phys* (2019) **20**:27–36. doi: 10.1002/ACM2.12529

90. Nicosia L, Sicignano G, Rigo M, Figlia V, Cuccia F, De Simone A, Giaj-Levra N, Mazzola R, Naccarato S, Ricchetti F, et al. Daily dosimetric variation between image-guided volumetric modulated arc radiotherapy and MR-guided daily adaptive radiotherapy for prostate cancer stereotactic body radiotherapy. *Acta Oncol* (2021) **60**:215–221. doi: 10.1080/0284186X.2020.1821090

91. Pham J, Savjani RR, Gao Y, Cao M, Hu P, Sheng K, Low DA, Steinberg M, Kishan AU, Yang Y. Evaluation of t2-weighted mri for visualization and sparing of urethra with mr-guided radiation therapy (Mrgrt) on-board mri. *Cancers (Basel)* (2021) **13**: doi: 10.3390/CANCERS13143564

92. Ma TM, Neylon J, Casado M, Sharma S, Sheng K, Low D, Yang Y, Steinberg ML, Lamb J, Cao M, et al. Dosimetric impact of interfraction prostate and seminal vesicle volume changes and rotation: A post-hoc analysis of a phase III randomized trial of MRI-guided versus CT-guided stereotactic body radiotherapy. *Radiother Oncol* (2022) **167**:203–210. doi: 10.1016/J.RADONC.2021.12.037

93. Mohler JL, Antonarakis ES, Armstrong AJ, D'Amico A V., Davis BJ, Dorff T, Eastham JA, Enke CA, Farrington TA, Higano CS, et al. Prostate Cancer, Version 2.2019, NCCN Clinical Practice Guidelines in Oncology. *J Natl Compr Canc Netw* (2019) **17**:479–505. doi: 10.6004/JNCCN.2019.0023

94. Jackson WC, Silva J, Hartman HE, Dess RT, Kishan AU, Beeler WH, Gharzai LA, Jaworski EM, Mehra R, Hearn JWD, et al. Stereotactic Body Radiation Therapy for Localized Prostate Cancer: A Systematic Review and Meta-Analysis of Over 6,000 Patients Treated On Prospective Studies. *Int J Radiat Oncol Biol Phys* (2019) **104**:778–789. doi: 10.1016/J.IJROBP.2019.03.051

95. Brand DH, Tree AC, Ostler P, van der Voet H, Loblaw A, Chu W, Ford D, Tolan S, Jain S, Martin A, et al. Intensity-modulated fractionated radiotherapy versus stereotactic body radiotherapy for prostate cancer (PACE-B): acute toxicity findings from an international, randomised, open-label, phase 3, non-inferiority trial. *Lancet Oncol* (2019) **20**:1531–1543. doi: 10.1016/S1470-2045(19)30569-8

96. Kishan AU, Dang A, Katz AJ, Mantz CA, Collins SP, Aghdam N, Chu FI, Kaplan ID, Appelbaum L, Fuller DB, et al. Long-term Outcomes of Stereotactic Body Radiotherapy for Low-Risk and Intermediate-Risk Prostate Cancer. *JAMA Netw open* (2019) **2**: doi: 10.1001/JAMANETWORKOPEN.2018.8006

97. Viswanathan AN, Yorke ED, Marks LB, Eifel PJ, Shipley WU. Radiation Dose–Volume Effects Of The Urinary Bladder. *Int J Radiat Oncol Biol Phys* (2010) **76**:S116. doi: 10.1016/J.IJROBP.2009.02.090

98. Ghadjar P, Zelefsky MJ, Spratt DE, Munck Af Rosenschöld P, Oh JH, Hunt M, Kollmeier M, Happersett L, Yorke E, Deasy JO, et al. Impact of dose to the bladder trigone on long-term urinary function after high-dose intensity modulated radiation therapy for localized prostate cancer. *Int J Radiat Oncol Biol Phys* (2014) **88**:339–344. doi: 10.1016/J.IJROBP.2013.10.042

99. Willigenburg T, Van Der Velden JM, Zachiu C, Teunissen FR, Lagendijk JJW, Raaymakers BW, De Boer JCJ, Van Der Voort Van Zyp JRN. Accumulated bladder wall dose is correlated with patient-reported acute urinary toxicity in prostate cancer patients treated with stereotactic, daily adaptive MR-guided radiotherapy. (2022) doi: 10.1016/j.radonc.2022.04.022

100. Bohoudi O, Bruynzeel AME, Tetar S, Slotman BJ, Palacios MA, Lagerwaard FJ. Dose accumulation for personalized stereotactic MR-guided adaptive radiation therapy in prostate cancer. *Radiother Oncol* (2021) **157**:197–202. doi: 10.1016/J.RADONC.2021.01.022

101. Pham J, Savjani RR, Gao Y, Cao M, Hu P, Sheng K, Low DA, Steinberg M, Kishan AU,

Yang Y. Evaluation of T2-Weighted MRI for Visualization and Sparing of Urethra with MR-Guided Radiation Therapy (MRgRT) On-Board MRI. *Cancers (Basel)* (2021) **13**: doi: 10.3390/CANCERS13143564

102. Kishan AU, Ma TM, Lamb JM, Casado M, Wilhalme H, Low DA, Sheng K, Sharma S, Nickols NG, Pham J, et al. Magnetic Resonance Imaging–Guided vs Computed Tomography–Guided Stereotactic Body Radiotherapy for Prostate Cancer. *JAMA Oncol* (2023) **9**:365–373. doi: 10.1001/jamaoncol.2022.6558

103. Cancer Institute N. Common Terminology Criteria for Adverse Events (CTCAE) Version 4.0. (2009) http://www.meddramsso.com [Accessed March 27, 2023]

104. Tibshirani R. Regression shrinkage and selection via the lasso: a retrospective. *J R Stat Soc Ser B (Statistical Methodol* (2011) **73**:273–282. doi: 10.1111/J.1467-9868.2011.00771.X

105. Yuan M, Lin Y. Model selection and estimation in regression with grouped variables. *J R Stat Soc Ser B (Statistical Methodol* (2006) **68**:49–67. doi: 10.1111/J.1467-9868.2005.00532.X

106. Liu J, Ji S, Ye J. SLEP: Sparse Learning with Efficient Projections. (2011) http://www.public.asu.edu/˜jye02/Software/SLEP [Accessed April 3, 2023]

107. Qian W, Li W, Sogawa Y, Fujimaki R, Yang X, Liu J. An Interactive Greedy Approach to Group Sparsity in High Dimensions. *Technometrics* (2017) **61**:409–421. doi: 10.1080/00401706.2018.1537897

108. Fan J, Li R. Variable Selection via Nonconcave Penalized Likelihood and its Oracle Properties. *https://doi.org/101198/016214501753382273* (2011) **96**:1348–1360. doi: 10.1198/016214501753382273

109. Hong DS, Heinzerling JH, Lotan Y, Cho LC, Brindle J, Xie X, Pistenmaa D, Cooley S, Boike T, Timmerman RD. Predictors of Acute Toxicity after Stereotactic Body Radiation Therapy for Low and Intermediate-risk Prostate Cancer: Secondary Analysis of a Phase I Trial. *Int J Radiat Oncol* (2011) **81**:S210. doi: 10.1016/j.ijrobp.2011.06.384

110. Seymour ZA, Chang AJ, Zhang L, Kirby N, Descovich M, Roach M, Hsu IC, Gottschalk AR. Dose-volume analysis and the temporal nature of toxicity with stereotactic body radiation therapy for prostate cancer. *Pract Radiat Oncol* (2015) **5**:e465–e472. doi: 10.1016/J.PRRO.2015.02.001

111. Leeman JE, Chen YH, Catalano P, Bredfeldt J, King M, Mouw KW, D'Amico A V., Orio P, Nguyen PL, Martin N. Radiation Dose to the Intraprostatic Urethra Correlates Strongly With Urinary Toxicity After Prostate Stereotactic Body Radiation Therapy: A Combined Analysis of 23 Prospective Clinical Trials. *Int J Radiat Oncol Biol Phys* (2022) **112**:75–82. doi: 10.1016/J.IJROBP.2021.06.037

112. Rossi L, Bijman R, Schillemans W, Aluwini S, Cavedon C, Witte M, Incrocci L, Heijmen B. Texture analysis of 3D dose distributions for predictive modelling of toxicity rates in radiotherapy. *Radiother Oncol* (2018) **129**:548–553. doi:

10.1016/J.RADONC.2018.07.027

113. Murakami Y, Soyano T, Kozuka T, Ushijima M, Koizumi Y, Miyauchi H, Kaneko M, Nakano M, Kamima T, Hashimoto T, et al. Dose-Based Radiomic Analysis (Dosiomics) for Intensity Modulated Radiation Therapy in Patients With Prostate Cancer: Correlation Between Planned Dose Distribution and Biochemical Failure. *Int J Radiat Oncol Biol Phys* (2022) **112**:247–259. doi: 10.1016/J.IJROBP.2021.07.1714

114. Rammant E, Ost P, Swimberghe M, Vanderstraeten B, Lumen N, Decaestecker K, Bultijnck R, De Meerleer G, Sarrazyn C, Colman R, et al. Patient- versus physician-reported outcomes in prostate cancer patients receiving hypofractionated radiotherapy within a randomized controlled trial. *Strahlenther Onkol* (2019) **195**:393–401. doi: 10.1007/S00066-018-1395-Y

115. Zuppone S, Bresolin A, Spinelli AE, Fallara G, Lucianò R, Scarfò F, Benigni F, Di Muzio N, Fiorino C, Briganti A, et al. Pre-clinical Research on Bladder Toxicity After Radiotherapy for Pelvic Cancers: State-of-the Art and Challenges. *Front Oncol* (2020) **10**:2000. doi: 10.3389/FONC.2020.527121/BIBTEX

116. Prado A, Flores I, Montero Á, Casa MÁ de la, Alonso L, Martí J, Fernández-Letón P, Rubio C, Prado A, Flores I, et al. Constraint Analysis and Bladder Wall Low-Dose-Constraint Reduction in Five-Fraction Urethra-Sparing Prostate SBRT. *Int J Med Physics, Clin Eng Radiat Oncol* (2021) **10**:132–148. doi: 10.4236/IJMPCERO.2021.103012

117. Byun DJ, Gorovets DJ, Jacobs LM, Happersett L, Zhang P, Pei X, Burleson S, Zhang Z, Hunt M, McBride S, et al. Strict bladder filling and rectal emptying during prostate SBRT: Does it make a dosimetric or clinical difference? *Radiat Oncol* (2020) **15**:1–9. doi: 10.1186/S13014-020-01681-6/TABLES/3

118. Henderson DR, Murray JR, Gulliford SL, Tree AC, Harrington KJ, Van As NJ. An Investigation of Dosimetric Correlates of Acute Toxicity in Prostate Stereotactic Body Radiotherapy: Dose to Urinary Trigone is Associated with Acute Urinary Toxicity. *Clin Oncol (R Coll Radiol)* (2018) **30**:539–547. doi: 10.1016/J.CLON.2018.05.001

119. Kim DWN, Cho LC, Straka C, Christie A, Lotan Y, Pistenmaa D, Kavanagh BD, Nanda A, Kueplian P, Brindle J, et al. Predictors of rectal tolerance observed in a dose-escalated phase 1-2 trial of stereotactic body radiation therapy for prostate cancer. *Int J Radiat Oncol Biol Phys* (2014) **89**:509–517. doi: 10.1016/J.IJROBP.2014.03.012

120. Pham J, Neilsen BK, Liu H, Cao M, Yang Y, Sheng K, Ma TM, Kishan AU, Ruan D. Dosimetric Predictors for Genitourinary Toxicity in MR-guided Stereotactic Body Radiation Therapy (SBRT):Substructure with Fraction-wise Analysis. *Med Phys* (2023) **Under Review**:

121. O'Connor LM, Choi JH, Dowling JA, Warren-Forward H, Martin J, Greer PB. Comparison of Synthetic Computed Tomography Generation Methods, Incorporating Male and Female Anatomical Differences, for Magnetic Resonance Imaging-Only Definitive Pelvic Radiotherapy. *Front Oncol* (2022) **12**:160. doi: 10.3389/FONC.2022.822687/BIBTEX